

**Novel Angular and Frequency Manipulation of Light  
in Nano-scaled Dielectric Photonic Systems**

by

Yichen Shen

Submitted to the Department of Physics  
in partial fulfillment of the requirements for the degree of

Doctor of Philosophy in Physics

at the

MASSACHUSETTS INSTITUTE OF TECHNOLOGY

June 2016

© Massachusetts Institute of Technology 2016. All rights reserved.

Signature redacted

Author .....

Department of Physics

May 23, 2016

Signature redacted

Certified by .....

Marin Soljačić

Professor

Thesis Supervisor

Signature redacted

Accepted by .....

Professor Nergis Mavalvala

Associate Department Head for Education





# Novel Angular and Frequency Manipulation of Light in Nano-scaled Dielectric Photonic Systems

by

Yichen Shen

Submitted to the Department of Physics  
on May 23, 2016, in partial fulfillment of the  
requirements for the degree of  
Doctor of Philosophy in Physics

## Abstract

Humankind has long endeavored to control light. In modern society, with the rapid development of nanotechnology, the control of light is moving toward devices at micrometer and even nanometer scales. At such scales, traditional devices based on geometrical optics reach their fundamental diffraction limits and cease to work. Nano-photonics, on the other hand, has attracted wide attention from researchers, especially in the last decade, due to its ability to manipulate light at the nanoscale. In this thesis, we explore novel control of light created by nanophotonic structures, with a common theme on light interference in nanoscaled dielectric photonic systems.

The first part of the thesis focuses on broadband angular selective nanophotonic systems. We survey the literatures and the current state of the art focused on enabling optical broadband angular selectivity. We also present a novel way of achieving broadband angular selectivity using Brewster mode in nanophotonic systems. We propose two categories of potential applications for broadband angularly selective systems. The first category aims at enhancing the efficiency of solar energy harvesting, through photovoltaic process or solar thermal process. The second category aims at enhancing light extracting efficiency and detection sensitivity. Finally, we discuss the most prominent challenges in broadband angular selectivity and some prospects on how to solve these challenges.

The second part of the thesis focuses on spectrum control of light using all-dielectric surface resonator. We propose a new structural color generation mechanism that produces colors by the Fano resonance effect on thin photonic crystal slab. We experimentally realize the proposed idea by fabricating the samples that show resonance-induced colors with weak dependence on the viewing angle. We also show that the colors can be dynamically tuned by stretching the photonic crystal slab fabricated on an elastic substrate. In a follow up work, we address how to overcome the challenge of mode leaking on dielectric substrate. We present a class of low-index zigzag surface structure that supports resonance modes even without index contrast with the substrate.

In the third part, we investigate neuromorphic computation using the interference

of light in on-chip dielectric photonic waveguide network. We first mathematically prove that conventional neural networks architecture can be equivalently represented by nanoscaled optical systems. We then experimentally demonstrate that our optical neural networks are able to give equivalent accuracy on a standard training datasets. In the last part, we show that in principle optical neural nets are at least 3 orders of magnitude faster and power efficient in forward propagation than conventional neural nets.

Thesis Supervisor: Marin Soljačić

Title: Professor

## Acknowledgments

First of all, I would like to thank my Ph.D. advisor Professor Marin Soljacic. Marin gives us the freedom to do what we love in lab and decide on the directions to take, yet he is always ready to provide insights and advice on the bigger pictures of the experiment. His expertise in optics and anything light-related never stops to amaze me, and I have learned an enormous amount from him as a scientist, an inventor, and a teacher. He has literally become a role model (on many aspect) for me. Thank you Marin, for your advice on my career choice, inspiration on my research projects, and encouragement during my difficult times.

I would like to thank Professor John Joannopoulos for been a virtual co-supervisor of my thesis. John is a co-author on almost all papers I published during my PhD. I'm thrilled every time when John called me or asked me to go to his office to go through my manuscripts. As well-established and as busy as John, his patience and care for his students is simply amazing, and this culture of caring has influenced every following generations of JDJ family.

I would also like to acknowledge Professor Steven Johnson, Professor Dirk Englund and Professor Rajeev Ram for teaching three of the best courses I have taken at MIT. And Professor Martin Zwierlein for serving as one of the most encouraging committee member.

My acknowledgements also go to all collaborators I had during my PhD, special thanks to Bikram Bhatia from Prof. Evelyne Wang's group, Farnaz Niroui from Prof. Vladimir Bulovic's group, Nicholas Harris from Prof. Dirk Englund's group, Dexin Ye and Zhiyu Wang from Prof. Lixin Ran's group (ZJU), Xiao Lin and Bin Zheng from Prof. Hongsheng Chen's group (ZJU).

The majority of my time over the last five years was spend with the members of the Soljacic's group. I have had a great deal of fun working with all of them, day and night, rain or shine. Chia-Wei (Wade) Hsu, as my 3-year office mate and ALSO roommate, is the person I spend most time with during my PhD. I really enjoyed the conversation we had on all kinds of things and the ski trip we had every year.

I'm greatly impressed by his hardworking, his talent and his passion on research. Furthermore, his sincereness and kind personality has made him one of the nicest person to spend time with. Josue Lopez, my office mate after Wade left, has been a great buddy to talk with, and we shared a lot of common value and interests on research. Scott Skirlo has been the one I spend a lot of time talking with recently on optical neuronetwork and on artificial intelligence. Ognjen Ilic, I still remember the time we spend together at Thousand Island Lake and in Hangzhou. I would also like to thank the senior members of the group, especially Ido Kaminer, Bo Zhen, Veronika Rinnerbauer and Ling Lu, for the help and advice to me in the past years. Finally, I would like to thank the UROP and RA students I have supervised, especially Emma Regan, Imbert Wong and Duncan Wheeler, their motivation, energy and eager to learn has been a significant driving force for me, and made me enjoy my PhD even more.

Life at MIT is enjoyable and exhilarating, but there can always be moments of confusion, disappointment, or simply bad days. I would like to thank all my dearest roommates, abbreviated as the gang of WORK (Wade, Oliver, Ray and Ken), for all fun time we spend together on board games, hot pot dinners, weekend-brunch and late night conversations :-).

I have met numerous wonderful people during my time here which I will not be able to enumerate, and I feel extremely lucky to have them around. I thank my fellow Physics graduate students, especially Edbert Sie, Shu-heng Shao and Tony Zhu for spending countless nights with me on Psets and preparing for qualify exams together. I thank the HFLSers in Boston, especially Weishun Xu, Yijia Wang, Shuai Li, Yue Fu, Taiyi Sun, Lei Dai and Ruichao Ma for all the fun, the memories and events we had together. I thank all the members of the the division-2 basketball community, for the 3 hours of ruthless and exhausted basketball games every weekend.

Finally, I thank my girlfriend, Li Zhu, for finding me in Ashdown gaming room the night before the exam :-), and your consistent support and encouragement everyday. My parents, Qingwen Yu and Youxing Shen, without whom I simply will not be here.





# Contents

<b>1</b>	<b>Introduction</b>	<b>15</b>
1.1	An Era for Nanophotonics . . . . .	15
1.2	Optical Broadband Angular Selectivity . . . . .	16
1.3	All-dielectric Surface Resonator . . . . .	17
1.4	Substrate-Independent Light Confinement in Bioinspired All-Dielectric Surface Resonators . . . . .	17
1.5	On-Chip Optical Computing . . . . .	18
<b>2</b>	<b>Broadband Angular Selectivity of Light at the Nanoscale</b>	<b>19</b>
2.1	Introduction . . . . .	19
2.2	Progress . . . . .	21
2.2.1	Microscale Geometrical Optics . . . . .	21
2.2.2	Birefringent-Polarizer Systems . . . . .	23
2.2.3	Plasmonic Brewster Angle in Metallic Gratings . . . . .	26
2.2.4	Optical Brewster Modes in One-Dimensional Photonic Crystals	29
2.2.5	Brewster Modes in Metamaterials . . . . .	36
2.3	Applications . . . . .	41
2.3.1	Solar Energy Harvesting . . . . .	41
2.3.2	Transmitters and Detectors . . . . .	48
<b>3</b>	<b>All-dielectric Frequency Selective Surface Resonator</b>	<b>53</b>
3.1	Introduction to Structural Colors . . . . .	53
3.2	Optical Fano-Resonances . . . . .	54

3.3	Experimental Demonstration of Structural Colors with Fano-Resonances	57
3.4	Dynamical Tuning of Structural Colors . . . . .	60
3.5	Conclusion . . . . .	63
<b>4</b>	<b>Substrate-Independent Light Confinement in Bioinspired All-Dielectric Surface Resonators</b>	<b>65</b>
4.1	Light Confinement on Dielectric Photonic Slab Resonator . . . . .	65
4.2	Bio-inspired Surface Resonator . . . . .	68
4.3	Experiment . . . . .	70
4.4	Applications . . . . .	72
4.4.1	Structural Colors . . . . .	72
4.4.2	Photonic Integrated Circuits . . . . .	73
4.5	Conclusion . . . . .	74
<b>5</b>	<b>On-Chip Optical Neuromorphic Computing</b>	<b>77</b>
5.1	Introduction . . . . .	77
5.2	Optical Neural Network Device Architecture . . . . .	78
5.2.1	Optical Interference Unit . . . . .	79
5.2.2	Optical Nonlinearity . . . . .	82
5.3	Simulation . . . . .	84
5.4	Time efficiency . . . . .	84
5.5	Conclusion . . . . .	86
5.6	Supplementary . . . . .	86
<b>6</b>	<b>Concluding remarks and future directions</b>	<b>87</b>
6.1	Optical Broadband Angular Selectivity . . . . .	87
6.2	All-dielectric metasurfaces . . . . .	89
6.3	On-Chip Optical Neuromorphic Computing . . . . .	90

# List of Figures

2-1	Conventional light selective devices. . . . .	20
2-2	Angular Selectivity based on Microscale Geometrical Optics . . . . .	22
2-3	Birefringent Broadband Angularly Selective Film . . . . .	25
2-4	Angular filter based on plasmonic Brewster angle in metallic gratings	27
2-5	Design of angular filter based on Brewster modes in 1D photonic crystals	30
2-6	Experimental realization of the 1D-PhC angular filter . . . . .	33
2-7	Comparison between the $p$ -polarized transmission spectrum of the Rigorous Coupled Wave Analysis (RCWA) simulation [1] and the corresponding experimental measurements. . . . .	34
2-8	Illustration of optical angularly selective filter in air using prisms . . .	35
2-9	Angular selectivity based on Brewster angle in metamaterials . . . . .	38
2-10	Experimental verification . . . . .	40
2-11	Application of Angular Selectivity in Energy Harvesting . . . . .	44
2-12	(A) Experimental setup for polarization-independent angularly selective filter system. (B) Emittance and absorptance measurement. The red and blue curves are calculated through Eqn. 2.15 and Eqn. 2.16 with measured data of the sample used in our previous work [2]. . . . .	47
2-13	(A) Illustration of enhancing signal/noise ratio by using angularly selective filter in front of an electromagnetic wave detector. (B) Illustration of enhancing directionality of light emitter using an angularly selective filter. . . . .	49
3-1	Light reflectance assisted with Fano-resonance . . . . .	56

3-2	Fabrication process of surface Fano resonator . . . . .	58
3-3	Si rods on amorphous silica wafer . . . . .	59
3-4	Si rods on PDMS . . . . .	62
4-1	Illustration of resonance mode in grating and bioinspired zigzag structure	67
4-2	Numerical simulation of the zigzag structure . . . . .	69
4-3	Experimental design and measurement . . . . .	71
S1	Numerical Simulation of T-bar Structure . . . . .	74
S2	Numerical Simulation of Suspended Grating . . . . .	75
S3	Microspectrometer Setup for Reflectance Measurement . . . . .	76
S1	General Architecture of Optical Neural Network . . . . .	79
S2	Illustration of Optical Interference Unit . . . . .	80
S3	The optical response of a nonlinear optical system (saturable absorption) that perform nonlinear calculation. Inset: Schematic illustration of the saturable absorption system. . . . .	83
S4	Optical bistable system that perform nonlinear calculation . . . . .	86

# List of Tables



# Chapter 1

## Introduction

### 1.1 An Era for Nanophotonics

Following the invention of lasers in the 1960s, photonics has seen enormous advances in its impact on almost every discipline from everyday life to the most advanced science. The development of photonics technology has greatly enhanced our abilities in generation, emission, transmission and modulation of light. Traditional optical devices based on geometrical optics such as lenses, mirrors and fibers have done an excellent job of manipulating light in the past decades. However, just as electronics has seen a dramatic miniaturization over the last 40 years, which enabled data density to be doubled every 18 months (the so-called Moore's law), the feature sizes of photonic devices have rapidly decreased too. Unfortunately, such a trend has unavoidably slowed down because we are already at the boundary where geometrical optics breaks down (feature size  $\approx 10\mu m$ ). In order to catch up with the density of electronic devices (feature size  $\approx 100nm$ ), the need to manipulate light at the micro-scale or even nano-scale is increasingly desirable for the optical community.

Interesting properties emerge when the structure that light interacts with has features at the length scale comparable to or smaller than light's wavelength – the nanometer to micrometer scale. The juicy science and their explosive application potential has made the study of such phenomena, namely called “nanophotonics”, one of the fastest growing fields in the recent decades. In this thesis, I will show a few

different routes on pushing the light manipulation beyond the scale limit of geometrical optics using nano-scaled dielectric systems. We have found amazing new optical phenomena such as optical broadband angular selectivity (Chapter 2) and geometrically “protected” surface states (Chapter 4), together with interesting applications of our systems in energy (Chapter 2), display (Chapter 3) and computing (Chapter 5).

The first theme of this thesis is on nanophotonic systems that has angular selective properties (Chapter 2). The second theme of this thesis is on all-dielectric surface resonators (Chapter 3 and Chapter 4). The last theme of this thesis is on On-chip Optical Computing (Chapter 5). Below is a brief break down summary of each chapter.

## 1.2 Optical Broadband Angular Selectivity

Humankind has long endeavored to control the propagation direction of light. Since time immemorial, shades, lenses, and mirrors have been used to control the flow of light. In modern society, with the rapid development of nanotechnology, the control of light is moving toward devices at micrometer and even nanometer scales. At such scales, traditional devices based on geometrical optics reach their fundamental diffraction limits and cease to work. Nano-photonics, on the other hand, has attracted wide attention from researchers, especially in the last decade, due to its ability to manipulate light at the nanoscale. This Chapter focuses on the nano-photonics systems that aim to select light based on its propagation direction. In the first half of the chapter, we survey the literature and the current state of the art focused on enabling optical broadband angular selectivity. The mechanisms we review can be classified into three main categories: (i) microscale geometrical optics, (ii) multilayer birefringent materials, and (iii) Brewster modes in plasmonic systems, photonic crystals, and metamaterials. In the second half, we present two categories of potential applications for broad-band angularly selective systems. The first category aims at enhancing the efficiency of solar energy harvesting, through photovoltaic process or solar thermal process. The second category aims at enhancing light extracting efficiency and de-

tection sensitivity. Finally, we discuss the most prominent challenges in broadband angular selectivity and some prospects on how to solve these challenges.

### **1.3 All-dielectric Surface Resonator**

Structural coloration is an interference phenomenon where colors emerge when visible light interacts with nanoscopically structured material and has recently become a most interesting scientific and engineering topic. However, current structural color generation mechanisms either require thick (compared to the wavelength) structures or lack dynamic tunability. This report proposes a new structural color generation mechanism that produces colors by the Fano resonance effect on thin photonic crystal slab. We experimentally realize the proposed idea by fabricating the samples that show resonance-induced colors with weak dependence on the viewing angle. Finally, we show that the resonance-induced colors can be dynamically tuned by stretching the photonic crystal slab fabricated on an elastic substrate.

### **1.4 Substrate-Independent Light Confinement in Bioinspired All-Dielectric Surface Resonators**

This chapter is a follow up study of Chapter 3, however, it also contains new optical phenomena that by itself is very interesting. Traditionally, photonic crystal slabs can support resonances that are strongly confined to the slab but also couple to external radiation. However, when a photonic crystal slab is placed on a substrate, the resonance modes become less confined, and as the index contrast between slab and substrate decreases, they eventually disappear. Using the scale structure of the *Dione juno* butterfly wing as an inspiration, we present a low-index zigzag surface structure that supports resonance modes even without index contrast with the substrate. The zigzag structure supports resonances that are contained away from the substrate, which reduces the interaction between the resonance and the substrate. We experimentally verify the existence of substrate independent resonances in the visible

wavelength regime. Potential applications include substrate-independent structural color and light guiding.

## 1.5 On-Chip Optical Computing

Artificial Neural Network (or deep learning) is an algorithm that gets much attention in recent years. In this chapter, we carried out a study to do neuromorphic computing with on-chip all-dielectric nanophotonic system. We first mathematically prove that conventional neural networks architecture can be equivalently represented by nanoscaled optical systems. We then experimentally demonstrate that our optical neural networks are able to give equivalent accuracy on a standard training datasets. In the last part, we show that in principle optical neural nets are at least 3 orders of magnitude faster and power efficient in forward propagation than conventional neural nets.

# Chapter 2

## Broadband Angular Selectivity of Light at the Nanoscale

### 2.1 Introduction

A monochromatic electromagnetic plane wave is characterized by three fundamental properties: frequency, polarization and propagation direction. The ability to select light according to each of these separate properties would be an essential step in achieving control over light. Over the past several decades, tremendous progress has been made towards achieving frequency selectivity and polarization selectivity on a scale far smaller than what geometrical optics permits (Fig. 2-1). For example, frequency selectivity can be obtained by using dyes, surface resonances [3–6], or taking advantage of photonic bandgaps in photonic crystals [7–11]. The ability to filter light by its colors has resulted in modern flat panel display technology. On the other hand, polarization selectivity is accomplished by means of “wire grid” polarizers [12] or by exploiting birefringent materials [13, 14]. The ability to filter light by its polarization has to a large extent enabled the 3D movie industry.

Light selection based on the direction of propagation, on the other hand, has seen relatively slower progress. Since ancient times, people have used a long tube in front of the eyes to effectively “block out” light from unwanted directions, or used louvers as a type of curtain to block out sunlight. Until now, most of the angularly



Figure 2-1: **Conventional light selective devices.** Frequency selectivity can be achieved by bandpass filters [15] or dielectric mirrors [16] (top panel); Polarization Selectivity can be achieved by wire grid polarizer, polaroid (polyvinyl alcohol polymer impregnated with iodine), or multilayer materials (3M Inc.) [17]; Traditional angularly selective devices are mainly based on geometric optics, such as telescopes [18] and radars [19].

selective systems have been based on geometrical optics approaches, such as the lens array systems in telescopes and the parabolic mirror disc in radar (Fig. 2-1). These systems are usually bulky and expensive.

In recent years, the development of nanophotonics has led to many new devices at the wavelength or even sub-wavelength scale. Methods based on diffraction and plasmonic resonances have been explored for the purpose of angularly selection [20, 21]; however, these effects are generally narrowband due to the inherent resonant properties of these mechanisms. Truly nanoscale *broadband* angular selectivity has long been a scientific and engineering challenge [2, 21–28].

In this chapter, we mainly focus on the topic of nanoscale broadband angular selectivity. We start by presenting the key theoretical concepts, experiments and proposals in this field, namely using micro-scale geometrical optics, birefringent materials, metallic gratings, photonic crystals and metamaterials. Among these approaches we have spearhead on the last two approaches. We then extend our discussion to potential applications and impact that broadband angularly selective material could bring us. Finally, we discuss outlook for further theoretical and technological advances.

## 2.2 Progress

### 2.2.1 Microscale Geometrical Optics

As has been discussed in the introduction, traditional broadband angularly selective systems are mainly based on geometrical optics. Recently, in order to reduce the system size, efforts have been made to push to the smallest scale limit of geometrical optics. In these efforts, shades, lenses and mirrors are made at the micrometer scale. At such length scales they are too small to be seen by human eyes while still big enough to function in the regime where laws of geometrical optics hold.

In mid 2000, motivated by the need to significantly narrow the usable viewing angle to provide viewing privacy, the broadband angularly selective effect was demonstrated using the micro-louvre approach by 3M Inc. [29–31]. As shown in Fig. 2-2A,B,

their angularly selective system comprises of (i) a transparent polymeric material as the base sheet; and (ii) light directing elements comprising absorptive material, wherein each element served as light shade with width  $w$ , height  $h$ , and distance  $a$  away from each other. In this micro-louvre design,  $w$ ,  $h$  and  $a$  are all in the range from  $5\mu m$  to  $50\mu m$ , so human eyes cannot see the micro-louvre components, but they are still much bigger than the wavelength of the visible light, so laws of geometrical optics still hold.

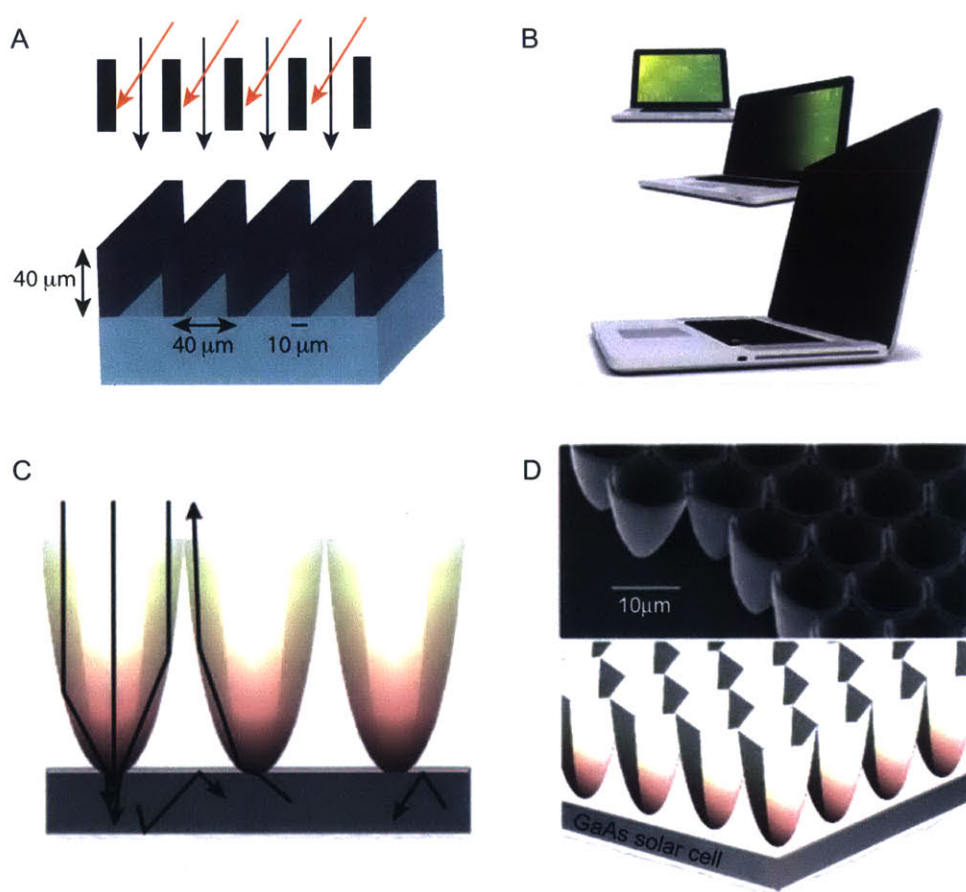


Figure 2-2: **Angular Selectivity based on Microscale Geometrical Optics** (A) A schematic design of a micro-louvre angularly selective system [29–31]. (B) The effect of the micro-louvre broadband angularly selective system as privacy protection. (C) Representative rays illustrate the function of the metallic coupler. (D) Schematic of metal array coupler on a solar cell with a randomizing back reflector and a scanning electron microscopy (SEM) of a structure fabricated in metal-coated resist via two-photon lithography. [32, 33]

Recently, a reflective broadband angularly selective filter based on microscale geometrical optics was proposed and fabricated by Atwater and co-workers [32, 33] (Fig. 2-2C,D). Their simulation showed that the parabolic directors they designed with  $22\mu\text{m}$  height and  $10\mu\text{m}$  diameter exhibit a strong angular selectivity. Light with incident angle less than  $5.6^\circ$  is able to funnel through the system, while light incident at larger angles is strongly reflected. In their work, the parabolic light director is fabricated using two-photon lithography, thin-film processing, and aperture formation by focused ion beam lithography [33]. The proposed system was later shown by the same group to have a potential (in theory) to increase the efficiency of solar cells [32]. However, a successful experimental demonstration of this proposed angularly selective absorber has yet to be reported due to the difficulties in high-resolution large scale fabrication.

In general, broadband angularly selective systems based on micro-geometrical optics designs have enabled new opportunities in managing light's direction on small scales. However, the performance of systems based on such a mechanism will ultimately be limited by diffraction and scattering effects when the scales of interest approach the geometrical optics limit.

### 2.2.2 Birefringent-Polarizer Systems

Another method that has been proposed to achieve broadband angular selectivity is to use a combination of polarizers and birefringent films [34–36]. This new approach is not based on geometrical optics. However, in reality, the birefringent material still needs to be many wavelengths thick in order to have enough phase retardation.

In a uniaxially birefringent film, if the extraordinary index (or the optical axis) lies in the plane of the film, it is said to be a half-wave plate if its thickness  $d_1$  and birefringence  $n_e - n_o$ , are chosen such that:

$$(n_e - n_o)d = \lambda/2$$

where  $\lambda$  is the wavelength of incident light. Half-waveplates have the property that

when plane polarized light is incident in the direction such that the polarization vector makes an angle  $\theta$  with the extraordinary axis of the film, then the plane of polarization will be rotated by  $2\theta$  as the light passes through the plate. The half wave plate can be made broadband by stacking several different birefringent layers together to compensate for the frequency dispersion.

Fig. 2-3 illustrates the simplest design that operates with this principle. The design comprises a half wave plate sandwiched between two polarizers. The polarizing axes of the two polarizers are crossed at  $90^\circ$ . Upon passing the first polarizer and the birefringent film, the polarization axis of the light is rotated appreciably. The rotation of the polarization axis is proportional to the distance that the light travels when passing through the birefringent film. For orthogonal light, the distance traversed in passing through the birefringent film is minimal and equal to the thickness  $d$  of the film. For oblique light, the distance is greater than  $d$  and depends upon the incident angle of the light. The degree of birefringence and the thickness of the birefringent film are chosen appropriately in relation to the optical and polarizing axes of the angularly selective film such that all orthogonal light has its polarizing axis rotated by  $90^\circ$  after passing through the birefringent film and is thus transmitted through the second polarizer, while non-orthogonal light has its polarizing axis rotated by a different angle, and is hence substantially blocked by the second polarizer.

Fig. 2-3B presents the experimental result of one such design [35]; It is composed of two linear polarizing laminated films (LP). The birefringent material was 27 mil Cellulose Diacetate film (CDA). The CDA and LP were separated by a  $1/16''$  spacer with an open window aperture of  $4.5'' \times 3''$ . The optical axis of the CDA was oriented horizontally (along the x axis with z being orthogonal to the  $xy$  plane of the film and x being the horizontal direction) with respect to the film axis and the LP was aligned with the polarizing axis oriented  $\pm 45^\circ$  to the optical axis of the CDA. As one can see, the combined material system has relatively high transparency for light at normal incidence, with an angularly selective window of around  $30^\circ$ .

Because the birefringence-polarizer angularly selective system is simple to fabricate and can be easily scaled up to a large area, it has found its most common ap-

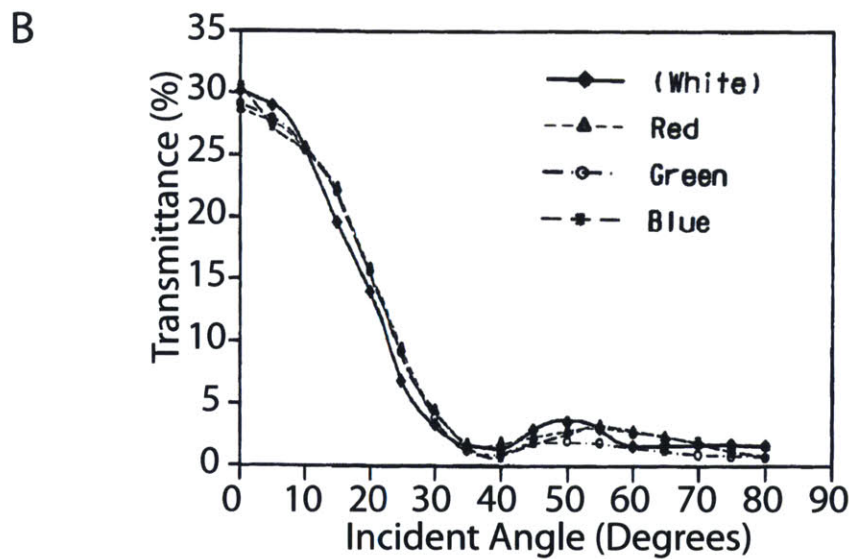
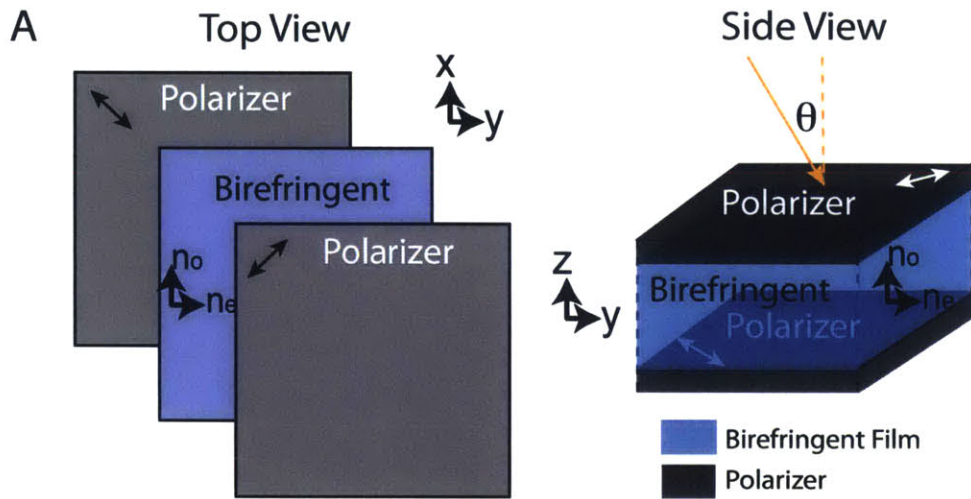


Figure 2-3: **Birefringent Broadband Angularly Selective Film** (A) Schematic layout of a birefringent angularly selective filter. (B) Experimental measurement result of the transmission spectrum (random polarization) of the sample at different incident angles [35].

plication in privacy protection films. However, as this mechanism relies solely on the rotation of the light polarization direction through the birefringent film, the angular window of transparency is typically quite broad ( $> 20^\circ$ ). Furthermore, the incident light has to pass through two polarizers, and as a result, the peak transmissivity is heavily attenuated.

### 2.2.3 Plasmonic Brewster Angle in Metallic Gratings

Extraordinary optical transmission (EOT) [22, 37, 38] is the phenomenon of greatly enhanced transmission of light incident at certain directions through a subwavelength aperture in an otherwise opaque metallic film which has been patterned with a regularly repeating periodic structure. Therefore, it is a natural candidate for providing angular selectivity. However, the traditional EOT is based on plasmonic resonances, so it inherently has a limited bandwidth of operation.

Instead of relying on plasmonic resonances inside the metallic film, Alù *et al* [24, 26–28] used a nonresonant Brewster-like effect based on impedance matching to achieve enhanced transmission through metallic gratings (Fig. 4-2). This mechanism provides enhanced transmission at a particular angle for transverse-magnetic (TM) polarization and is weakly dependent on the frequency.

To understand this plasmonic Brewster angle mechanism, consider the geometry of Fig. 4-2A: A metallic screen of thickness  $l$ , corrugated by slits of width  $W$  and period  $d$ , is illuminated by a TM wave. The scattering from such a periodic structure can be modeled by using a transmission-line (TL) approach [39]. The circuit analog is depicted at the bottom of Fig. 4-2A: the free space region is modeled as a semi-infinite transmission line; for a given angle of incidence  $\theta$  with respect to the  $z$  axis, the effective vacuum wavenumber is  $\beta_0 = k_0 \cos \theta$ , the characteristic impedance per unit length of vacuum can be calculated by

$$Z_0 = \frac{V_0}{I_0} = \frac{\int_0^d E_x dx}{H_y} = \frac{|E|d \cos \theta}{|E|/\eta_0} = \eta_0 d \cos \theta. \quad (2.1)$$

Where  $\eta_0 = \sqrt{\mu_0/\epsilon_0}$  is the vacuum impedance. Inside each slit, modal propagation

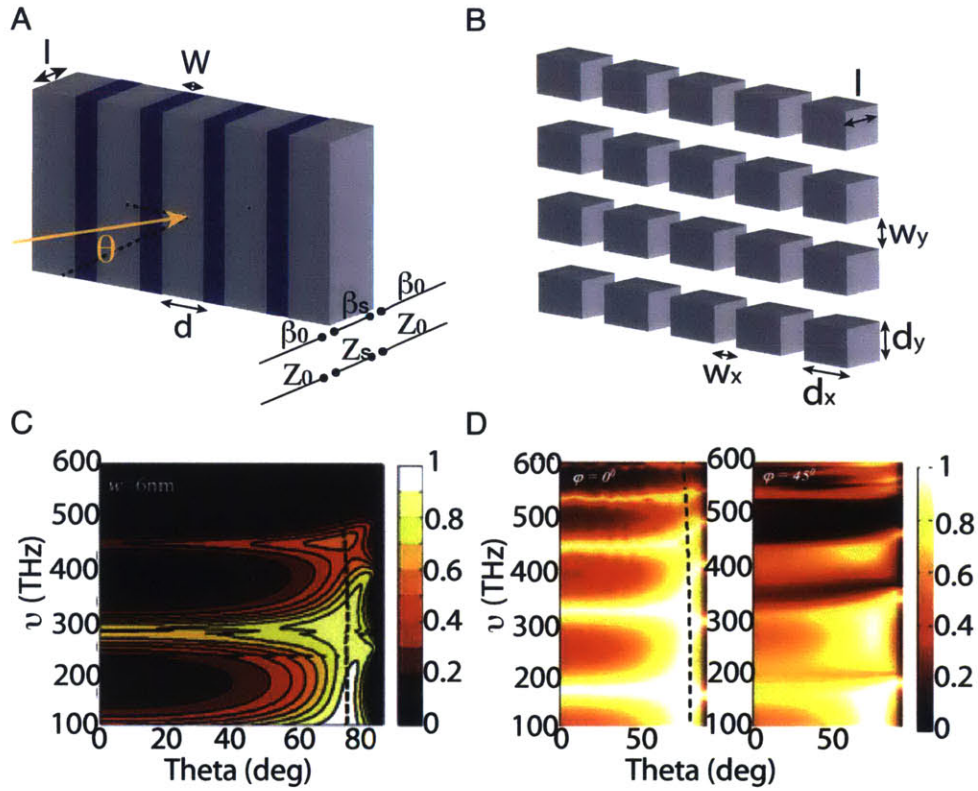


Figure 2-4: **Angular filter based on plasmonic Brewster angle in metallic gratings.** (A) The geometry of the 1-dimensional grating (B) The geometry of the 2-dimensional grating. (C) Angular transmission spectra for a 1-dimensional grating with thickness  $l = 200\text{nm}$ , period  $d = 96\text{nm}$ , and slit width  $w = 6\text{nm}$ . The dashed line indicates the plasmonic Brewster angle condition [24]. (D) Angular transmission spectra for a 2-dimensional grating thickness  $l = 400\text{nm}$ , period  $d_x = d_y = 100\text{nm}$ , and slit width  $w_x = 6\text{nm}$  and  $w_y = 12\text{nm}$ . The dashed line indicates the plasmonic Brewster angle condition [23].

does not depend on the incidence angle. When the slit is significantly narrower than the periodicity and the wavelength, that is, only the dominant TM mode propagates inside the slit and only the fundamental diffraction order radiates in free space, i.e.,  $W \ll d < \lambda_0 = 2\pi/k_0$ , and the characteristic impedance per unit length  $Z_s$  satisfies the equation [40]

$$Z_s = W\beta_s/(\omega\epsilon_0), \quad (2.2)$$

where the wavenumber  $\beta_s$  satisfies the equation

$$\tanh \left[ \sqrt{\beta_s^2 - k_0^2} W/2 \right] \sqrt{\beta_s^2 - k_0^2} = -\sqrt{\beta_s^2 - k_0^2} \epsilon_m / \epsilon_m.$$

From Eqn 2.1 and Eqn. 2.2, we observe that the characteristic impedances of air and slit are not equal in general, but as we change the incident angle  $\theta$ , there can exist an angle  $\theta_B$ , or the so-called plasmonic Brewster angle, such that the two impedances are equal  $Z_0(\theta_B) = Z_s$ . The condition for such impedance matching is:

$$\cos \theta_B = (\beta_s W)/(k_0 d). \quad (2.3)$$

This impedance matching is independent of the grating thickness  $l$  and only depends weakly on the frequency  $\omega$ , as shown in Fig. 4-2C. In fact, the angularly selective working frequency range extends from zero frequency (DC) to the breakdown of this model  $d \approx \lambda_0$ .

The mechanism described above using 1D metallic gratings only works for light incident in the plane perpendicular to the slit direction. In a later paper [23], the same group led by Alù demonstrated that such a phenomenon, representing the equivalent of Brewster transmission for plasmonic screens, can also occur in 2D metallic gratings of various structural forms and shapes, and that it may be made less sensitive to the azimuthal angle  $\phi$  (Fig. 4-2B,D).

Although the experimental realization has been demonstrated in the microwave regime, it is challenging to realize such plasmonic Brewster mode in the visible wavelength regime, mainly due to the metallic loss in the visible regime, and the challeng-

ing fabrication requirement (needed resolution  $< 5\text{nm}$ ). However, the Brewster mode idea proposed here has inspired subsequent research that brings broadband angular selectivity to new levels of performance.

## 2.2.4 Optical Brewster Modes in One-Dimensional Photonic Crystals

Photonic crystals (PhCs) are periodic structures [9] in which the index of refraction varies between high-index and low-index, with a periodicity comparable to the wavelength. Such an environment presents to photons what the periodic atomic potential of a semiconductor presents to electrons. In particular, just as a periodic atomic potential will open up a band gap inside the crystal where no electron is allowed to propagate, under the right conditions, a PhC can exhibit a complete photonic band gap: a range of frequencies in which light is forbidden to propagate inside the material.

This unique property of blocking light using photonic band gaps leads to the following intriguing possibility: imagine if one could secure a direction in a one dimensional (1-D) PhC such that incident light always passes through (regardless of frequencies and the thickness of each layer), and could design the thickness of each layer of the 1-D PhC such that light propagating in other directions is all blocked by the photonic band gaps; then the resulting material system would potentially have broadband angularly selective behavior.

Such an idea was proposed and realized in a recent work by us [2]. The design principle rests on three different features of a 1-D PhC: (i)  $p$ -polarized light transmits without any reflection at the Brewster angle of each interface, (ii) the existence of band gaps that prevent light propagation for given frequency ranges, and (iii) the band-gap-broadening effect of heterostructures (Fig. 2-5D,F).

Consider the light reflection at the interface between two dielectric materials with permittivities  $\epsilon_1$ ,  $\epsilon_2$  and permeabilities  $\mu_1$ ,  $\mu_2$  respectively. The off-axis reflectivity

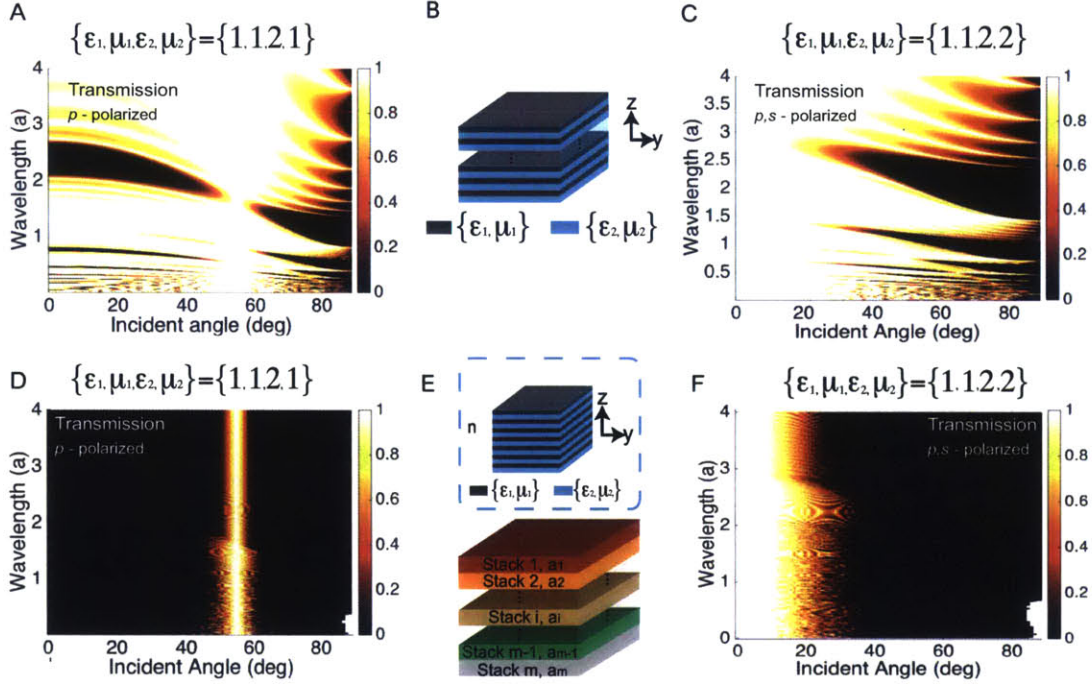


Figure 2-5: **Design of angular filter based on Brewster modes in 1D photonic crystals.** (A)  $p$ -polarized transmission spectrum of a quarter-wave stack with 20 alternative layers of two materials having  $\epsilon_1 = 1$  and  $\epsilon_2 = 2$  respectively. (B) Schematic layout of a simple quarter-wave stack. (C) The same plot as in part (A), but with  $\epsilon_1 = \mu_1 = 1$ ,  $\epsilon_2 = \mu_2 = 2$ , and for both polarizations. (D)  $p$ -polarized transmission spectrum of 50 stacks of quarter-wave stacks at various periodicities. Each quarter-wave stack consists of 10 bi-layers of  $\{\epsilon_1 = 1, \epsilon_2 = 2\}$  materials. The periodicities of these quarter-wave stacks form a geometric series  $a_i = a_0 r^{i-1}$  with  $r = 1.0212$ , where  $a_i$  is the periodicity of  $i^{\text{th}}$  stack. (E) Schematic layout of the heterostructure stacking mechanism (F)  $p, s$ -polarized transmission spectrum for a structure that has the same number of stacks and layers per stack as in part (D), but with different material properties:  $\epsilon_1 = \mu_1 = 1$ ,  $\epsilon_2 = \mu_2 = 2$ .

can be calculated directly from the generalized Fresnel equations [14]:

$$\left(\frac{E_r}{E_i}\right)_{\perp} = \frac{\frac{1}{Z_i} \cos \theta_i - \frac{1}{Z_t} \cos \theta_t}{\frac{1}{Z_i} \cos \theta_i + \frac{1}{Z_t} \cos \theta_t} \quad (2.4)$$

and

$$\left(\frac{E_r}{E_i}\right)_{\parallel} = \frac{\frac{1}{Z_t} \cos \theta_i - \frac{1}{Z_i} \cos \theta_t}{\frac{1}{Z_i} \cos \theta_i + \frac{1}{Z_t} \cos \theta_t}, \quad (2.5)$$

where the impedance  $Z$  is defined as  $Z = \sqrt{\frac{\mu}{\epsilon}}$ , the subscripts  $i$  and  $r$  denote incident light and reflected light, respectively, and the subscripts  $\perp$  and  $\parallel$  indicate the direction of the electric field  $\vec{E}$  with respect to the plane of incidence. At certain incident angle  $\theta_B$  (so-called Brewster angle) when the numerators in Eqn. 2.4 and Eqn. 2.5 become zero, there is no reflection at the interface. Notice for the 1D PhC, the light propagating at the Brewster angle from  $Z_1$  material to  $Z_2$  material automatically satisfies the Brewster condition from  $Z_2$  material to  $Z_1$ .

Next, consider a simple quarter-wave stack consisting of these two materials (Fig. 2-5B). In such a system, monochromatic plane waves with frequency  $\omega$  cannot propagate in certain directions due to destructive interference, or so-called photonic band-gaps (dark region in Fig. 2-5A,C). However, when the light is propagating at the Brewster angle ( $55^\circ$  in Fig. 2-5A and  $0^\circ$  in Fig. 2-5C), since it has no reflections at any interface, destructive interference does not happen, and the light always goes through. The transmission spectrum of such a quarter-wave stack is shown in Figs. 2-5A,C. Furthermore, from Figs. 2-5A and C, we can see that a single quarter-wave stack is not sufficient to provide broadband angular selectivity. What one needs is a bigger photonic band gap to cover the entire spectrum at off-Brewster angles. The enlargement of photonic band gap is achieved by stacking together quarter-wave stacks with various periodicities [41–43] (Figs. 2-5D,F).

To show the feasibility of the method described above, we present an experimental realization for the  $\epsilon_1 \neq \epsilon_2$ ,  $\mu_1 = \mu_2 = 1$  case. The sample was fabricated with Bias Target Deposition (BTD) technique [44] at 4Wave AFCS tool (4Wave Inc.), using  $\text{SiO}_2$  ( $\epsilon_1 \approx 2.18$ ,  $\mu_1 = 1$ ) and  $\text{Ta}_2\text{O}_5$  ( $\epsilon_2 \approx 4.33$ ,  $\mu_2 = 1$ ) on a 2 cm  $\times$  4 cm fused silica

wafer (University Wafer Inc.). The sample consists of 84 layers in total (Fig. 2E). There are six bi-layer stacks ( $m = 6$ ), each bi-layer stack consisting of seven bi-layers ( $n = 7$ ), with the thicknesses of each layer equal in a given stack. The periodicities of the 6 bi-layer stacks form a geometric series with  $a_i = a_0 r^{i-1}$ , for the  $i^{\text{th}}$  stack, where  $a_0 = 140$  nm and  $r = 1.165$ . For index matching purposes, the whole sample was immersed into a colorless liquid with dielectric constant  $\epsilon_{\text{Liquid}} = \epsilon_1 = 2.18$  (Cargille Labs) (Fig. 2-6A). The sample could work in the air by adding a coupling prism or by using a porous material for  $\epsilon_1$  which has a lower refractive index, such as aerogel [45].

The sample is transparent (up to 98%) to  $p$ -polarized incident light at the Brewster angle  $\theta_B = 55^\circ$  (Fig. 2-6D), as shown in Fig. 2-6D; the angular window of transparency is about 8 degrees. It behaves like a mirror at all other incident angles over the entire visible spectrum (Fig. 2-6B,C,E). For  $s$ -polarized incident light, the sample behaves like a mirror at all angles [46]. The  $p$ -polarization transmittance of the sample in the visible spectrum was measured using an Ultraviolet-Visible spectrophotometer (Cary500i)—a  $p$ -polarizer was used to filter the source beam. The experimentally measured result agrees with the Rigorous Coupled Wave Analysis (RCWA) [1] simulation prediction (Fig. 2-7), which includes the measured dispersion of materials (index variation  $< 1.3\%$  for  $\text{SiO}_2$  and  $< 6.2\%$  for  $\text{Ta}_2\text{O}_5$  over the wavelength range from 400 nm to 700 nm). In the experimental measurements, the peak transmittance at the Brewster angle gets lower at shorter wavelengths (Fig. 2-7B) because the wavelength is getting closer to the dimensional tolerance of fabrication.

In the original experiment, the sample had to be immersed in an index-matched liquid. In-air operation requires ultra-low index materials (such as aerogel [47]) as one of the composition layers, which makes it hard to fabricate. Furthermore, the Brewster angle at the interface of two dielectric media (in the lower index isotropic material) is always larger than  $45^\circ$ . An implementation introduced later by the same group used macroscopic prisms to improve the previous design, such that the device can be directly used in air without using ultra-low index materials. In addition, the angle of high transparency can be adjusted easily over a broad range, including normal incidence [48] (Fig. 2-8). Notice for normal angular-window design shown in

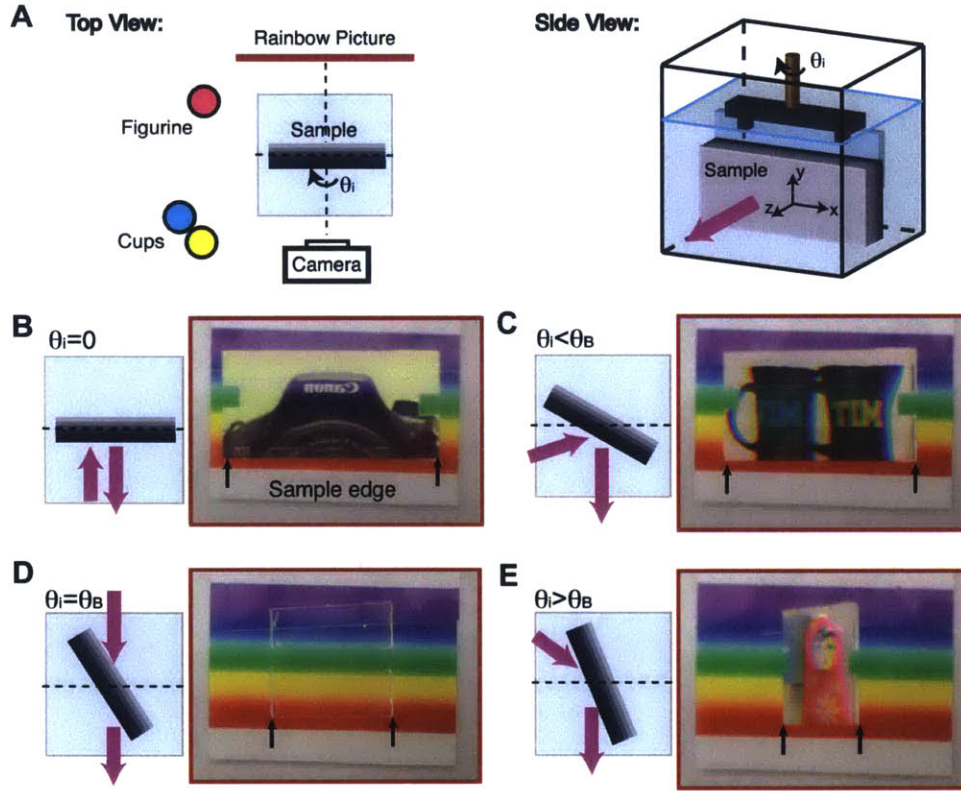


Figure 2-6: **Experimental realization of the 1D-PhC angular filter.** (A) Schematic layout of the experimental setup. The system is immersed in a liquid that is index matched to  $\epsilon_1 = \epsilon_{SiO_2} = 2.18$ . (B) Normal incident angle setup. The sample behaves like a mirror and reflects the image of the camera. (C)  $\theta_i = 30^\circ$  setup. The sample behaves like a mirror and reflects the image of MIT cups in the lab. (D)  $\theta_i = \theta_B = 55^\circ$  setup. The sample becomes transparent for the entire visible regime for  $p$ -polarized light. (E)  $\theta_i = 70^\circ$  setup. The sample behaves as a mirror and reflects the figurine placed at the corner of the table. In B-E a polarizer is installed on the camera so it detects only  $p$ -polarized light [2]

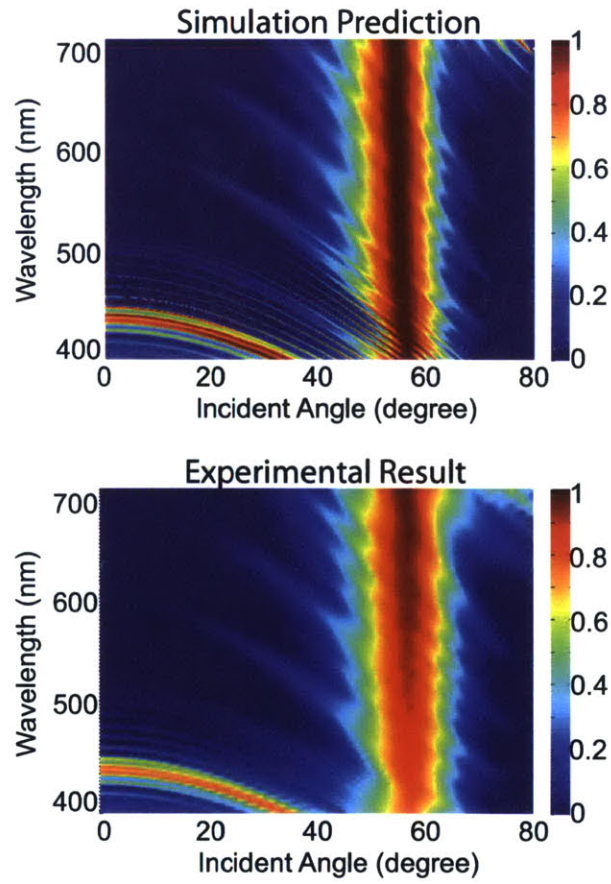


Figure 2-7: Comparison between the  $p$ -polarized transmission spectrum of the Rigorous Coupled Wave Analysis (RCWA) simulation [1] and the corresponding experimental measurements.

Fig. 2-8B, the image is not preserved. However, the image can be preserved if one adds another layer of angular filter, as described in Ref. [48].

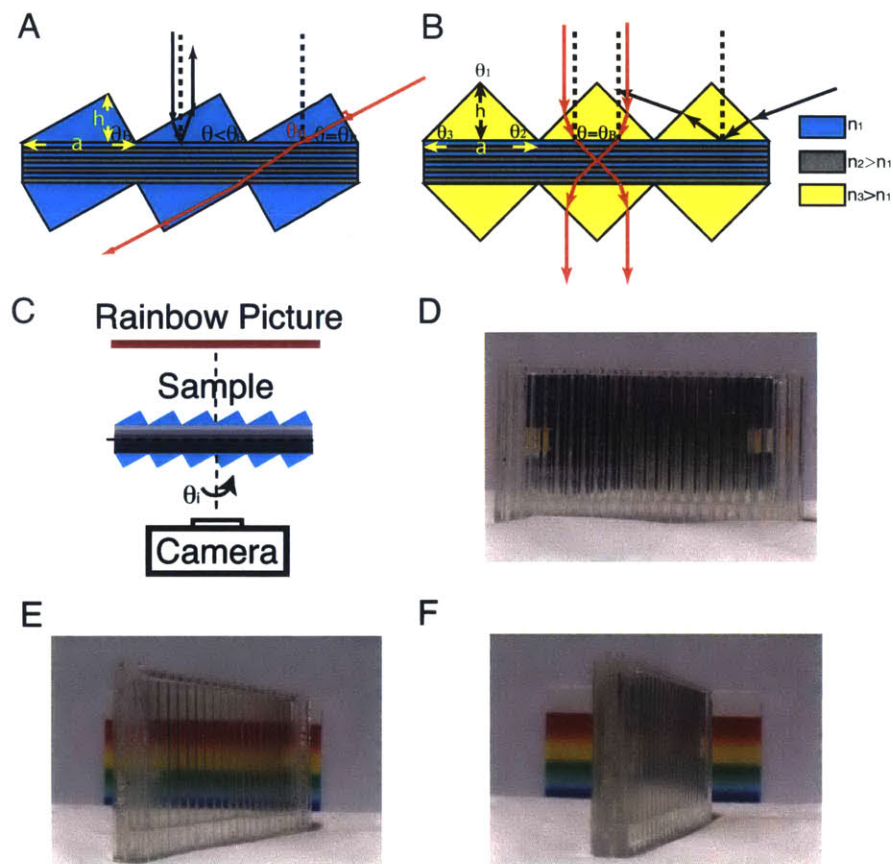


Figure 2-8: **Illustration of optical angularly selective filter in air using prisms** (A) Oblique incidence prism design (B) Normal incidence prism design. The red beams represent the light rays coming in at the right direction so the prisms can couple the light into the Brewster mode inside the PhC slab. The black beams represent the light coming in from other directions so they cannot be coupled into the Brewster mode inside the PhC slab; hence, they are reflected back into the prisms. (C) Schematic view of the system setup. (D) Normal incidence angle setup: the sample is reflective. (E)  $\theta = 55^\circ$  setup: the sample becomes transparent. (F)  $\theta = 75^\circ$  setup: the sample become reflective again.

From Eqn. 2.5, it is apparent that the brewster angle and the polarization dependence solely depend on the material properties ( $Z$ ). It worth pointing out that for common isotropic materials, their magnetic susceptibility is typically 1 ( $\mu = 1$ ), making the impedance  $Z_i$  and  $Z_t$  almost never equal to each other. In such case,

for  $p$ -polarized light, there will exist an oblique Brewster angle (as we demonstrated above), and for  $s$ -polarized light, as there is no Brewster angle, this construction behaves as a dielectric mirror that reflects over a wide frequency range and over all incident angles.

The mechanism above provides both angular selectivity and polarization selectivity, which is useful in many applications. For example, in most optically pumped lasers, the pumping light comes in with a specific polarization and at one specific angle. A cavity built with both angular- and polarization- selective mirrors will allow the pumping light to get through, while at the same time trapping all the light with other propagation directions and polarizations inside the cavity.

The restriction on the polarization can be lifted by releasing the conventional requirement that  $\mu_1 = \mu_2 = 1$ . For the past decade, it has been demonstrated that metamaterials have the potential to achieve  $\epsilon = \mu \neq 1$  in broadband [49–51]. Consider two media with  $\epsilon_1 = \mu_1 \neq \epsilon_2 = \mu_2$ ; under those circumstances there is no reflection at the interface at normal incidence because the two media are impedance matched, where the impedance  $Z$  is defined as  $Z = \sqrt{\frac{\mu}{\epsilon}}$ . When  $Z_i = Z_t$ , the reflectivities for  $s$ - and  $p$ - polarized light become identical. In particular, the Brewster angle is the same for both polarizations ( $\theta_B = \theta_i = \theta_r = 0^\circ$ ). Another way to bypass the oblique Brewster angle restriction is using birefringent materials, which we will explain in the next section.

### 2.2.5 Brewster Modes in Metamaterials

Metamaterials are artificially created materials engineered to have properties that may not be found in nature. They are assemblies of building blocks, each consisting of several different conventional material types such as metals or plastics. The building blocks are usually arranged in periodic patterns with a deep-subwavelength periodicity. Metamaterials gain their properties not from their fundamental composition (crystal structure, electron distribution, etc.), but from their artificially-designed microscopic building blocks. Their precise shape, geometry, size, orientation and arrangement can affect the waves of light or sound in an unconventional manner,

creating material properties that cannot be achieved with conventional materials.

In 2011, Hamam *et al* [52] pointed out that an angular photonic band gap can exist within anisotropic material systems (Fig. 2-9A). Inspired by this and building upon their earlier work of using Optical Brewster Modes in 1-D PhC [2], we proposed a new design that replaces one of the isotropic materials in conventional 1-D PhC by effective-anisotropic-metamaterials. In this way one can in principle achieve a broadband angularly selective behavior at *arbitrary* incident angles [25].

To understand this effect, one can follow the same line of argument as in the previous section, but this time consider the light reflection at the interface between an isotropic medium with dielectric constant  $\epsilon_{iso}$  and an anisotropic medium with dielectric constant  $\{\epsilon_x, \epsilon_y, \epsilon_z\}$ . The reflectivity of *p*-polarized light with a propagating angle  $\theta_i$  (defined in the isotropic material) at an isotropic-anisotropic interface is [53]

$$R_p = \left| \frac{n_x n_z \cos \theta_i - n_{iso} (n_z^2 - n_{iso}^2 \sin^2 \theta_i)^{\frac{1}{2}}}{n_x n_z \cos \theta_i + n_{iso} (n_z^2 - n_{iso}^2 \sin^2 \theta_i)^{\frac{1}{2}}} \right|^2 \quad (2.6)$$

where  $n_x = n_y$  and  $n_z$  are the refractive indices of the anisotropic material at the ordinary and extraordinary axes, respectively, and  $n_{iso}$  is the refractive index of the isotropic material.

Therefore, the Brewster angle,  $\theta_i = \theta_B$ , can be calculated by setting  $R_p = 0$ , giving:

$$\tan \theta_B = \sqrt{\left( \frac{\epsilon_z}{\epsilon_{iso}} \right) \left[ \frac{\frac{\epsilon_x}{\epsilon_{iso}} - 1}{\frac{\epsilon_z}{\epsilon_{iso}} - 1} \right]} \quad (2.7)$$

Birefringent crystal can be grown through molecular beam epitaxy [54], however, growing multilayer birefringent structure is challenging. Nevertheless, recent progress by 3M Inc. has shown that fabricating such isotropic-anisotropic multilayer PhC using birefringent polymers might be possible [17], even for visible light.

Furthermore, following this idea, we [25] introduced tunability of the dielectric constant of the anisotropic layer by using metamaterial to replace the anisotropic layers in Fig. 2-9A. As shown in Fig. 2-9B, each metamaterial layer consists of several high-index ( $\epsilon_1 = 10$ ) and low-index ( $\epsilon_2 = \epsilon_{air} = 1$ ) isotropic material layers. When

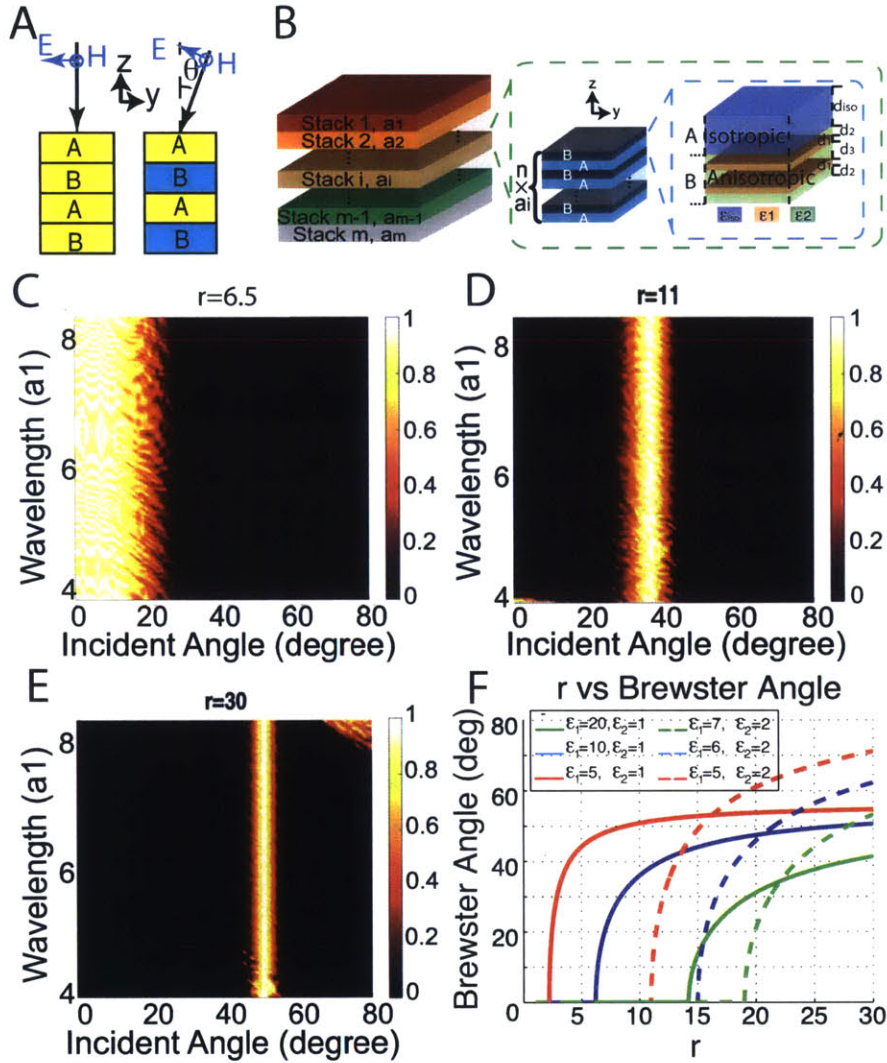


Figure 2-9: **Angular selectivity based on Brewster angle in metamaterials.** (A) Schematic illustration of a stack of isotropic-anisotropic photonic crystals. Layer A is an isotropic medium; layer B is an effective anisotropic medium consisting of two different isotropic media with dielectric constants  $\epsilon_1$  and  $\epsilon_2$ . The thickness ratio between these two materials is set to be  $r$ . (B) Effective index for  $p$ -polarized light in an isotropic A - anisotropic B multilayer system. Left panel: all the layers have the same index. Right panel: the change in incident angle leads to a change in the observed index of the anisotropic material layers B. (C-E) Transmission spectrum for the metamaterial photonic crystal design. The materials and structures are illustrated in subfigure A, with  $n = m = 30$ ,  $\epsilon_1 = 10$ ,  $\epsilon_2 = 1$ , and  $\epsilon_{iso} = 2.25$ , but different  $r$ . (C)  $r = 6.5$  and  $\theta_B = 0^\circ$  (D)  $r = 9$  and  $\theta_B = 24^\circ$ . (E)  $r = 11$  and  $\theta_B = 38^\circ$ . (F)  $r = 30$  and  $\theta_B = 50^\circ$ . (F) Dependence of the Brewster angle (coupled in from air) on  $r$  for various values of  $\epsilon_1$  and  $\epsilon_2$ . Solid and dashed lines, correspond, respectively, to  $\epsilon_1$  for air and  $\epsilon_2$  for PDMS [25].

the combined high-index-low-index two-layer unit is sufficiently thin compared to the wavelength (optically thin), the whole system can be treated as a single anisotropic medium with the *effective* dielectric permittivity tensor  $\{\epsilon_x, \epsilon_y, \epsilon_z\}$  [55]:

$$\epsilon_x = \epsilon_y = \frac{\epsilon_1 + r\epsilon_2}{1 + r} \quad (2.8)$$

$$\frac{1}{\epsilon_z} = \frac{1}{1 + r} \left( \frac{1}{\epsilon_1} + \frac{r}{\epsilon_2} \right) \quad (2.9)$$

where  $r$  is the ratio of the thickness of the two materials  $\epsilon_1$  and  $\epsilon_2$ :  $r = d_2/d_1$ . Substituting Eqn. 2.8 and Eqn. 2.9 into Eqn. 2.7 gives the dependence of Brewster angle  $\theta_B$  on  $r$ :

$$\theta_B(r) = \arctan \left[ \sqrt{\frac{\epsilon'_1 \epsilon'_2 (\epsilon'_1 + r\epsilon'_2 - 1 - r)}{(1 + r)\epsilon'_1 \epsilon'_2 - \epsilon'_2 - \epsilon'_1 r}} \right] \quad (2.10)$$

where  $\epsilon'_1 = \epsilon_1/\epsilon_{\text{iso}}$ , and  $\epsilon'_2 = \epsilon_2/\epsilon_{\text{iso}}$ .

Eqn. 2.10 shows that it is possible to adjust the Brewster angle by changing the ratio  $r = d_1/d_2$ , which is confirmed by transfer matrix calculation of the transmission spectrum of an isotropic-anisotropic PhC with  $n = m = 30$  but different  $r$  (Fig. 2-9C-E). The dependence of the Brewster angle on  $r$  is presented in Fig. 2-9F. At small  $r$ , there is either no Brewster angle or the light cannot be coupled into the Brewster angle from air. As  $r$  gets larger, a rapid increase in the Brewster angle is observed, which eventually plateaus, approaching the isotropic-isotropic limit,  $\theta_B = \arctan \sqrt{\epsilon_2/\epsilon_{\text{iso}}}$  [14]. Note that if  $\epsilon_2$  is some soft elastic material (such as PDMS or air), one can simply vary  $r$  by changing the distance  $d_2$  in real time, and hence varying the Brewster angle accordingly. Such *tunability* of the Brewster angle does not exist in conventional (non-metamaterial) isotropic-isotropic or isotropic-anisotropic photonic crystals, where the Brewster angle depends solely on the materials' dielectric properties.

To show the feasibility of the above-mentioned method, we present an experimental realization in the microwave regime. Since our goal here is only to demonstrate the concept, we kept the experimental setup simple. We implemented the geometry design in Fig. 2-9B, using Rogers R3010 material ( $\epsilon_1 = 10$ ), air ( $\epsilon_2 = 1$ ), and polypropylene ( $\epsilon_{\text{iso}} = 2.25$ , Interstate Plastics). The thickness of each layer is chosen

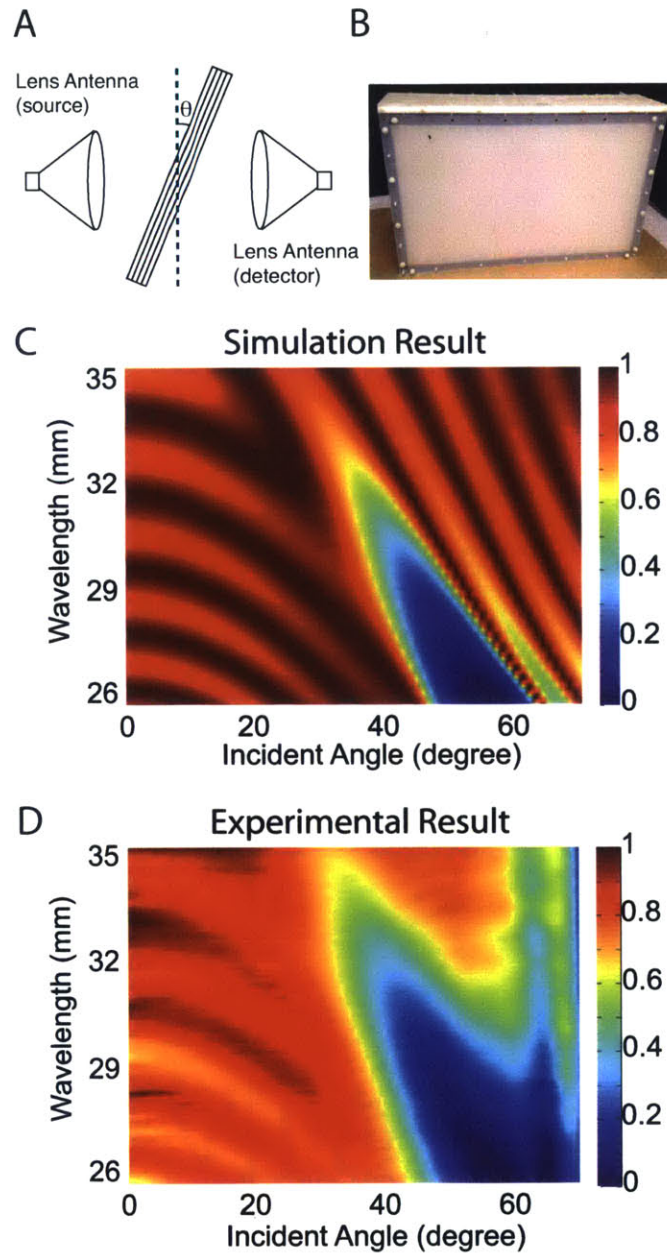


Figure 2-10: **Experimental verification** a, A schematic illustration of the experimental setup. b, Photo of the fabricated sample. c, d, Comparison between  $p$ -polarized transmission spectrum of Transfer Matrix Method, and the experimental measurements.

to be  $\{d_{iso}, d_1, d_2, d_3\} = \{3.9, 0.5, 1.6, 3.9\}mm$ . A simple 12-period structure ( $m = 12$ ,  $n = 1$  case in Fig. 2-9B) was made (Fig. 2-10B). With the experimental setup shown in Fig. 2-10A, the transmission spectrum for  $p$ -polarized light was measured in the wavelength range from  $26mm$  to  $35mm$ . For incident angles less than 60 degrees, the experimental result (Fig. 2-10D) agrees well with the simulation (analytical) result calculated from Transfer Matrix Method [14] (Fig. 2-10C). For larger incident angles, the finite-sized microwave beam spot picks up the edge of the sample, which causes the transmission to deviate from the theoretical simulation; by using bigger samples, one should be able to resolve this issue.

## 2.3 Applications

### 2.3.1 Solar Energy Harvesting

One major application for the reflective angularly selective material system is in solar energy harvesting, such as in solar cells and solar thermal systems.

Current solar energy harvesting technologies for electricity production can be categorized into two main conversion processes: direct conversion and indirect conversion. Direct conversion is also known as photovoltaic conversion (solar cells). In an ideal photovoltaic conversion, each photon absorbed by a solar-active material (typically silicon) causes an electron to jump from the valence band to the conduction band and create a hole in the valence band, leading to an electric current pulse [56]. On the other hand, indirect conversion, or solar thermal conversion, corresponds to conversion of solar energy into heat by collection in a solar absorber and subsequent conversion of this heat into work by means of a thermal engine [57], a thermal photovoltaic device [58–60], or a thermal electrical device [61, 62].

The total efficiency of a solar cell (SC) or solar thermal (ST) system can be calculated by:

$$\mu_{total} = \mu_I \cdot \mu_{SC/ST} \quad (2.11)$$

where  $\mu_I$  represents the efficiency of light trapping, which is the percentage of solar

energy that is trapped in the semiconductor layer (for solar cells) or absorber (for solar thermal systems), while  $\mu_{SC/ST}$  represents the efficiency of the actual photo-electric conversion in solar cells, or thermal-electric conversion in solar thermal systems. Since  $\mu_{SC/ST}$  is mainly limited by the inherent material properties such as the Shockley-Queisser limit [63] (for solar cells) and Carnot efficiency (for solar thermal systems), here we focus on applying angularly selective surface to trap light and optimize  $\mu_I$ .

The efficiency of light trapping  $\mu_I$  is highly sensitive to the absorber's emittance and can be calculated by:

$$\mu_I = \frac{P_{\text{absorbed}}}{P_{\text{inc}}} = \frac{J_s - J_e - J_r - J_o}{J_s} = 1 - \frac{J_e}{J_s} - \frac{J_r}{J_s} - \frac{J_o}{J_s}, \quad (2.12)$$

where  $P_{\text{absorbed}}$  is the total power trapped in the solar cell or solar thermal system, and  $P_{\text{inc}}$  is the total power incident on the device. The quantity  $J_s$  is the incoming energy flux from sunlight,  $J_e$  is the outgoing energy flux from photon emission,  $J_r$  is the energy flux of sunlight reflected from the system, and  $J_o$  are other thermal losses due to conduction, convection and non-radiative electron recombination.  $J_s$  and  $J_e$  are given by:

$$J_s = \Omega_c(N_s) \int_0^\infty d\omega \epsilon_a(\omega) I_s(\omega) \quad (2.13)$$

$$J_e = \pi \int_0^\infty d\omega \epsilon_e(\omega) I_{\text{emit}}(\omega) \quad (2.14)$$

where the effective absorptance  $\epsilon_a(\omega)$  and emittance  $\epsilon_e(\omega)$  are defined as:

$$\epsilon_a(\omega) = \epsilon_t(\omega, \theta = \theta_t), \quad (2.15)$$

$$\epsilon_e(\omega) = \frac{1}{\pi} \int_{\phi=0}^{2\pi} \int_{\theta=0}^{\pi/2} \sin \theta \cos \theta \epsilon_t(\omega, \theta, \phi) d\phi d\theta. \quad (2.16)$$

Here  $\Omega_c(N_s) \approx N_s \cdot 7 \cdot 10^{-5}$  rad is the solid angle spanned by the solar disk (at solar concentration of  $N_s$  suns),  $\epsilon_t$  is the transmission of angularly selective filter at different incident angles  $(\theta, \phi)$  and frequency  $f$  ( $\epsilon_t = 1$  if no angularly selective filter is applied).  $\theta_t$  is the angle of incidence,  $I_s$  is the solar spectrum, and  $I_{\text{emit}}$  is the emission

spectrum of solar cell or solar thermal system. Therefore, in order to maximize the solar trapping efficiency  $\mu_I$ , we need to minimize  $J_e/J_s$  and  $J_r/J_s$  (Eqn. 2.12).

When conventional solar cells or solar thermal absorbers are placed under direct sunlight, they receive light only from the solid angles spanned by the solar disk ( $\Omega_{inc} = \theta_c(1) \approx 6.8 \cdot 10^{-5}$  rad). On the other hand, they emit and reflect light isotropically ( $\Omega_{emit} \approx 2\pi$  rad). The large ratio between absorption and emission solid angles ( $\Omega_{inc}/\Omega_{emit} \approx 1.1 \cdot 10^{-5}$ ) results in an increase in photon entropy [64], hence decreasing the efficiency of solar cells and solar thermal systems. There are two ways to increase  $\Omega_{inc}/\Omega_{emit}$  [65]: The first way is to increase  $\Omega_{inc}$  by applying a concentrator to the system [66–68]. The second way is to decrease the angle of emission by applying angularly selective filters. The effect of such a filter is similar to using a concentrator, but can be made much thinner and can be easily incorporated into traditional solar cell modules. The angularly selective approach has been theoretically proposed several times [69–75]. Up to now there have been only a few experimental realizations using narrow band angularly selective filters [76]. Methods of using broadband angularly selective filters in solar energy harvesting have been proposed theoretically [32], but remain challenging to fabricate. Using the implementation of the PhC angularly selective filter described in the previous section, we present here a new method to achieve broadband angular confinement (depicted in Fig. 2-11), and discuss its potential to improve the efficiency of current solar cells and solar thermal systems.

## Solar Cells

In solar cells, the emission loss is mainly due to radiative recombination [77], and incomplete absorption (especially in thin film solar cells). A broadband angularly selective system can help mitigate losses from both of these causes, through the effects of photon-recycling (for radiative recombination) and light trapping (for reflected sunlight).

For solar cells with high radiative efficiency, such as GaAs or other direct-bandgap material solar cells, radiative recombination and emission is a major loss mechanism.

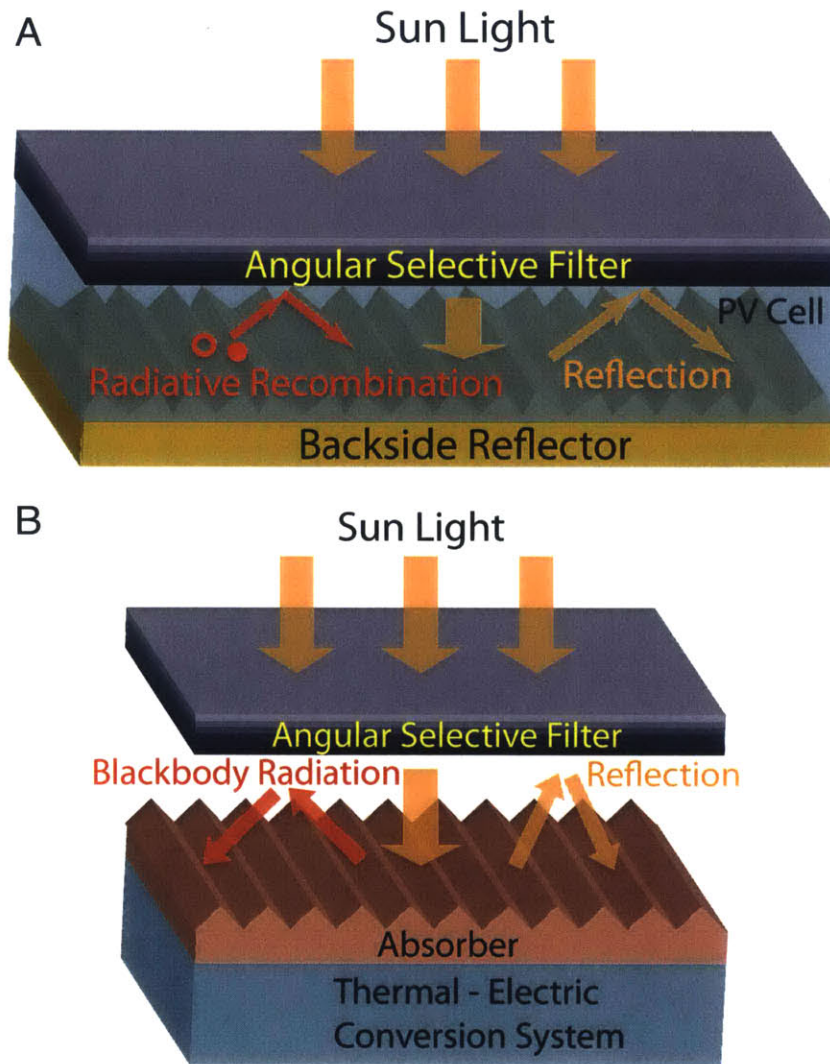


Figure 2-11: **Application of Angular Selectivity in Energy Harvesting** (A) Solar Cell Application (B) Solar Thermal Application.

In this case, photon recycling that reflects the radiated photons back into the solar cell using angularly selective filters can lead to enhancement in voltage and efficiency [32, 71, 76, 78]. In particular, a recent theoretical work from Atwater's group [71] has predicted that by limiting the light emission angle, it is possible to achieve an enhancement of absolute efficiency by 8% (without Auger recombination) and 5% (with Auger recombination) for GaAs solar cells with ideal back reflector. In addition, it is also shown that the efficiency enhancement will increase significantly for thinner cells. Another recent work by Hohn *et al.* [79] has compared the effects of the following three different angularly selective mechanisms in GaAs solar cells: 1) narrowband angularly selective filter with an optically flat mirror back reflector, 2) narrowband angularly selective filter with a diffusive back reflector, and 3) broadband angularly selective filter with a diffusive back reflector. The work shows theoretically that using a broadband angularly selective filter one can achieve a solar cell with the highest efficiency (41.3%), compared with the Shockley-Queisser limit of 33.5% [80]; and the lowest cell thickness (less than 100nm). However, such a broadband angularly selective filter was only hypothesized in both works mentioned above.

On the other hand, for solar cells with low radiative efficiency, such as silicon solar cells, non-radiative processes like Auger recombination limit the voltage; hence photon recycling will have little effect on the efficiency [81,82], and the light trapping effect is more significant. For solar cells with diffusive back reflector (Fig. 2-11A) [83], it has been theoretically shown that limiting the emission angle in the *solar spectrum* can reduce the optical escape cone and enhance the light trapping [32,73, 84, 85]. Enhanced light trapping effect allows for better absorption of sunlight in a very thin cell (reducing material usage), and an increase in current, voltage and efficiency of the solar cell as well. A recent theoretical calculation from H. Atwater's group [71, 85] has shown that amorphous silicon hetero-junction with intrinsic thin layer (HIT) cells perform significantly better under angle restriction, with efficiency gains of approximately 1% absolute achievable, with moderate angle restriction in parallel with a 50% reduction in cell thickness.

Here we propose a new setup (Fig. 2-12) that achieves the broadband angular

confinement using the angularly selective filter we *et al.* reported (Fig. 2-8) [2, 48]. As illustrated in the inset of Fig. 2-12, although the PhC filter lets *p*-polarized light pass through only at the Brewster angle, one can use achromatic quarter-wave plate and a mirror to convert the randomly polarized sunlight into *p*-polarized light. Furthermore, the polarization restriction of the filter might also be lifted with the recent development of high efficiency polarizer [86, 87]. We point out that since the PhC angularly selective window gets narrower as one increases the number of layers [2], in principle the transparent angular window can be decreased further with more layers in the PhC filter. With a 1000-layer filter, the angular confinement (Fig. 2G in Ref. [2]) can be made less than  $2^\circ$ .

In conclusion, with the implementation of the broadband angularly selective filter, the enabled enhanced photon recycling and light trapping could allow for thinner solar cells with higher efficiency.

### Solar Thermal Systems

Fig. 2-11B presents the schematic design of using the broadband angularly selective filter in solar thermal systems. Such broadband angularly selective filters can help increase the light trapping efficiency of current solar thermal systems through the following two ways:

Firstly, it can help eliminate the reflection loss from the absorber, or reduce  $J_r/J_s$  in Eqn. 2.12. In order to effectively absorb sunlight, the solar thermal absorber is typically made up of metal with high thermal stability, such as tantalum or steel, so the surface reflection from the absorber is significant. For example, one of the most recently optimized solar thermal absorbers still exhibits a 13% loss due to light reflection from the air-metal interface [88, 89]. With the implementation of the broadband angularly selective filter, as illustrated in Fig. 2-11B and Fig. 2-12A, the reflected sunlight can be effectively trapped so that all the reflected light is recycled back to the absorber.

Secondly, it can help mitigate the photon emission loss from the absorber, or reduce  $J_e/J_s$  in Eqn. 2.12. In traditional low temperature solar thermal systems,

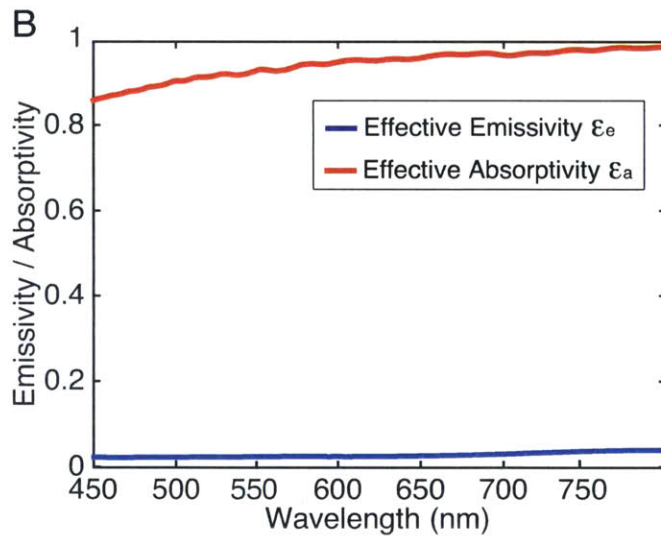
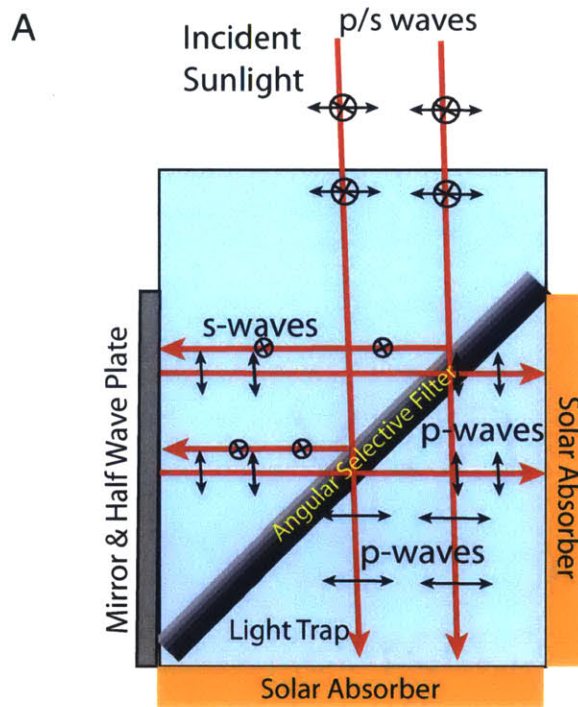


Figure 2-12: (A) Experimental setup for polarization-independent angularly selective filter system. (B) Emittance and absorptance measurement. The red and blue curves are calculated through Eqn. 2.15 and Eqn. 2.16 with measured data of the sample used in our previous work [2].

frequency selective absorbers are used to effectively separate the incident light and the emitted light [59, 90, 91]. However, there is a strong incentive to increase the absorber temperature since higher absorber temperature helps to achieve higher thermal-electric conversion (Eqn. 2.12). In the case of high temperature solar thermal systems, the overlap of  $I_s$  and  $I_{emit}$  in frequency is no longer negligible. A more detailed theoretical analysis by Blanco *et al* [92] suggests that in such a case one needs to rely on angular selection, although in this paper such broadband angularly selective materials are hypothetical.

The same setup we proposed in the solar cell section (Fig. 2-12) can also work for an angularly selective high-temperature solar thermal system. The transmittance of the angular confinement system at different incident angles is measured, and the calculated effective emittance  $\epsilon_e$  and absorptance  $\epsilon_a$  are plotted over the entire visible spectrum (Fig. 2-12). On average a factor of 47 enhancement is obtained for  $\epsilon_a/\epsilon_e$  over the entire visible spectrum compared to the case without angularly selective filter ( $\epsilon_a/\epsilon_e = 1$ ). Such ratio can be enhanced even more by increasing the number of layers in the PhC slab, as explained in the previous work [2]. Furthermore, since the angularly selective filter does not need to be in a direct contact with the absorber, materials with high thermal stability are not required.

### 2.3.2 Transmitters and Detectors

Among many detectors ranging from microscopes, cameras, radars, to telescopes, an important indicator used to describe their detection quality is the signal-to-noise ratio (SNR). In many cases, detectors are used to detect an object that usually spans only a small solid angle, while unwanted (noise) signals coming in from other directions can decrease the SNR. A similar argument can be applied to emitters: in many signal transmission applications, such as display screens, WiFi and radio stations, we only want the signal to propagate in certain directions. Signals propagating in other directions are either not wanted or present a waste of energy.

In the past, various geometrical optic setups have been used to achieve angular selectivity and increase the SNR of the detectors or increase directionality of emitters.

Such a setup can take up a lot of space and is sometimes the most expensive part of the whole system. Replacing the bulky and expensive traditional angularly selective system by the nanoscale, material-based angularly selective system (Fig. 2-13) has the potential to bring revolutionary changes to many important applications. In the following part of this section, we list a few major applications that are most suitable for the implementation of nanoscale broadband angularly selective system.

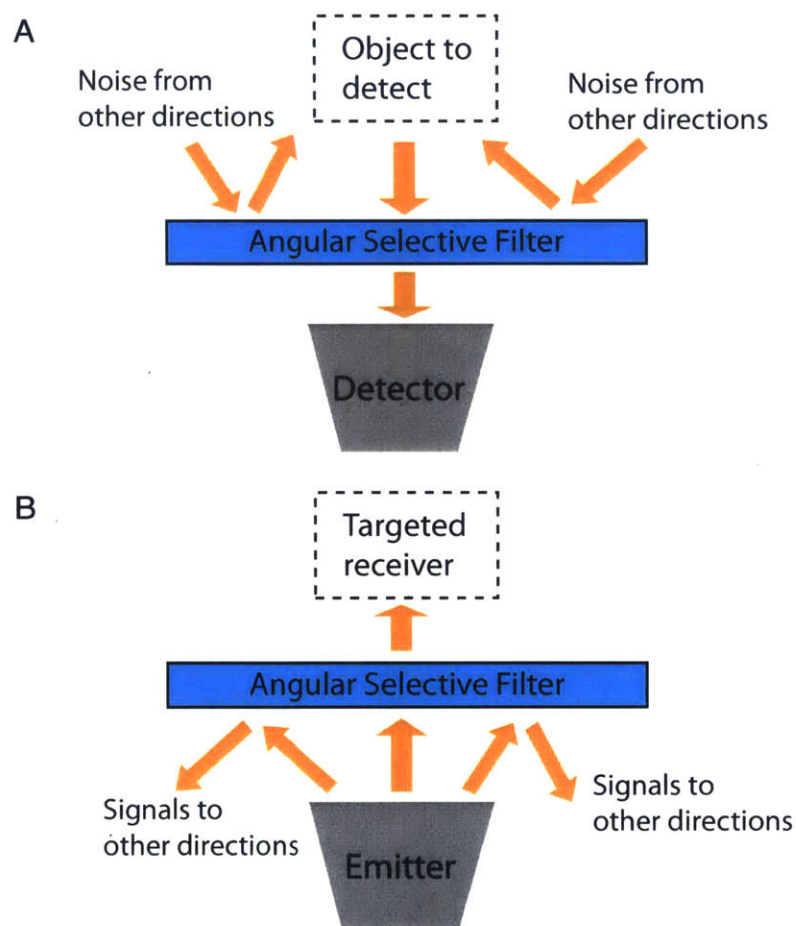


Figure 2-13: (A) Illustration of enhancing signal/noise ratio by using angularly selective filter in front of an electromagnetic wave detector. (B) Illustration of enhancing directionality of light emitter using an angularly selective filter.

- **Transmitter Application: Privacy Screens**

As we discussed in section II, privacy screens are one of the earliest applications that motivated the study of angularly selective material systems. Today, privacy

screens are widely used. In the United States, many healthcare workers are required by the Health Insurance Portability and Accountability Act of 1996 (HIPAA) to use privacy screens in the workplaces. Bankers and consultants in major firms are also required to use privacy screens when traveling or in public settings.

The most widely used privacy screens today employ the traditional micro-louvre design described in Fig. 2-2A. Since the absorptive micro-louvre also blocks part of the light even from normal incidence, such a filter typically reduces the brightness of the screen by 40%-50%. Furthermore, the periodic grating structure of the privacy film can interfere with the thin-film-transistor (TFT) layer inside the LCD screen and form Moire patterns on the screen.

New broadband angularly selective filter based on nano photonics could lead to higher transmission at normal incidence, better angular selectivity and no Moire patterns.

- **Detector Application: Radars, Telescopes**

Common detectors such as radars and telescopes are usually used to observe distant objects. Unfortunately unwanted signals coming from other directions can cause a reduction in SNR. In order to increase the SNR, typical radar systems use a steerable parabolic disk so that only light coming in at certain angle can be reflected to the receiving antenna (Fig. 1). Similarly, telescopes use lens/mirrors systems [93, 94] or long detecting tube [95] to selectively filter out signals coming from unwanted directions. One common feature of this geometrical optics approach is that the angularly selective system needs to have the depth (size along the propagation direction of incident light) proportional to the detection aperture. Therefore, for those radars and telescopes that have large apertures, the angularly selective system would be very bulky, and sometimes even occupy the majority of the volume of the entire detecting system.

Here we propose a new design concept based on an angularly selective material system. As shown in Fig. 2-13, an angularly selective filter is added in front

of the detector. Such implementation has been developed for narrow band detectors [96], but not for broadband detectors yet. The angular sensitivity and bandwidth of this new kind of detection system can be made as good as the traditional detection systems (if not better); however, such an angularly selective filter can be made much thinner and independent of the aperture size, which has a potential to significantly reduce the system volume and might be valuable for many defense and commercial applications.



## Chapter 3

# All-dielectric Frequency Selective Surface Resonator

### 3.1 Introduction to Structural Colors

People have long been inspired by nature's ability to create a dazzling range of colors. Dyes, pigments and metals that absorb light of only certain colors and reflect the rest of the spectrum are the most common color generation mechanisms. Recently, great attention has been paid to a different type of color generation mechanism: structural coloration, which produces color without the use of dyes and pigments [97]. Structural coloration is, in principle, an interference phenomenon where colors emerge when visible light interacts with nanoscopically structured material. Compared with pigmentary colors, structural colors 1) usually appear brighter under sunlight; 2) are immune to photobleaching, and 3) can be tuned dynamically [98]. Due to those advantages, they have found applications in painting, textiles and passive displays [99, 100].

Structural colors are typically produced by light interference within bulk materials, for example, structural colors from scattering [101–103], multilayer interference [104–106] and photonic crystals [9, 100, 107, 108]. In these bulk effects, the color gets brighter and sharper as one increases the bulk thickness, i.e., number of particles (for scattering), the number of layers (for multilayer interference), or the number of

periods (for photonic crystals). As a result, designs based on these mechanisms require the structured materials to be much thicker than the wavelength. However, in certain applications, such as optical coating [109, 110], structures with low thickness are preferred [111]. Conventional optical coatings use thin film interference, which typically requires metallic substrates in order to achieve enough reflection. Therefore, the structural colors generated through thin film interference are material limited, angular sensitive and cannot be tuned dynamically. Recently, structural colors from plasmonic effect was investigated extensively. [3–5, 112–116] It has demonstrated promising features including low thickness (single layer structure), full color display, and friendly for nano-fabrication. However, since metals are inherently lossy in visible spectrum, the reflection peak from plasmonic effect is typically broadband and less intensive. Furthermore, plasmonic colors are also angular sensitive.

In this report, we propose a new mechanism to generate structural color — different from any of the current mechanisms mentioned above — that produces color by interference between the directly reflected light and the guided resonances mode on an *all-dielectric surface structure*. The new mechanism exhibits strong peak reflection (100% in simulation), is flexible in material choice, suitable for large area fabrication, and has weak angular dependence. Moreover, it supports dynamic tuning of the reflectance spectrum, as we will demonstrate in this study.

## 3.2 Optical Fano-Resonances

The resonance-induced reflectance used in this study to generate static and dynamic color is related to a more general resonance category, known as Fano resonance [117]. This optical resonance was first investigated and analyzed by Fan *et al* [118] in photonic crystal slabs. The optical Fano resonance can be understood as an interference effect: light incident on a periodic surface structure (Fig. 3-1a) excites a one-dimensionally confined mode supported by the surface structure. The localized mode leaks into the surrounding environment (Fig. 3-1d), interfering with the directly reflected light from the surface. When the reflected and the radiated light have the same

phase, constructive interference produces a sharp reflectance peak (Fig. 3-1b,c). The reflectance line shape near resonance peak can be calculated by temporal coupled mode theory and fitted by the Lorentzian line shape [119]:

$$r = r_d + f \frac{\gamma}{i(\omega - \omega_0) + \gamma}, \quad (3.1)$$

where the factor  $f$  is the complex amplitude of the resonant mode,  $r_d$  is the direct reflection coefficients,  $\omega_0$  and  $\gamma$  are the center frequencies and widths of the resonance, which are directly related to the quality factor  $Q$  of the resonance mode:

$$Q \approx \frac{\omega_0}{\gamma}. \quad (3.2)$$

To date, most Fano resonance features discussed have a rather high  $Q$  ( $> 50$ ) to be used for lasing or filtering purposes. In these cases, the reflectance peak is relatively narrow band. However, in order to achieve color control using Fano resonance, the reflectance peak needs to be reasonably broadband to reflect enough light. As a proof of principle, we study a square lattice of rods as shown in Fig. 3-1a. This structure is also chosen for its suitability for dynamic tuning, which will be discussed later in this paper. The dielectric constant of the rods is chosen to be  $\epsilon_2 = 4$  (e.g.,  $\text{Ta}_2\text{O}_5$ ) and the surrounding environment has  $\epsilon_1 = 1$  i.e., vacuum. The reflectance spectra for structures with different rod radii  $r$  are computed with the rigorous coupled wave analysis (RCWA) method [1] and plotted in Fig. 3-1b. The bandwidth of the resonant peaks increases with increasing radius  $r$  of the rods. The resonant modes at different  $r$  and the corresponding field distribution are calculated using a Finite Difference Time Domain (FDTD) method [120] (Fig. 3-1d) and their locations are highlighted in Fig. 3-1b. The spectral position of the resonant modes exactly follows the reflectance maxima, suggesting that the reflectance peaks are indeed caused by Fano resonance. The quality factor  $Q$  for each resonant mode is evaluated using a low-storage "filter diagonalization method" (FDM) [121] and plotted in Fig. 3-1e, which shows that  $Q$  decreases as  $r$  increases.

One interesting feature of Fano-resonance induced reflection spectrum is its angu-

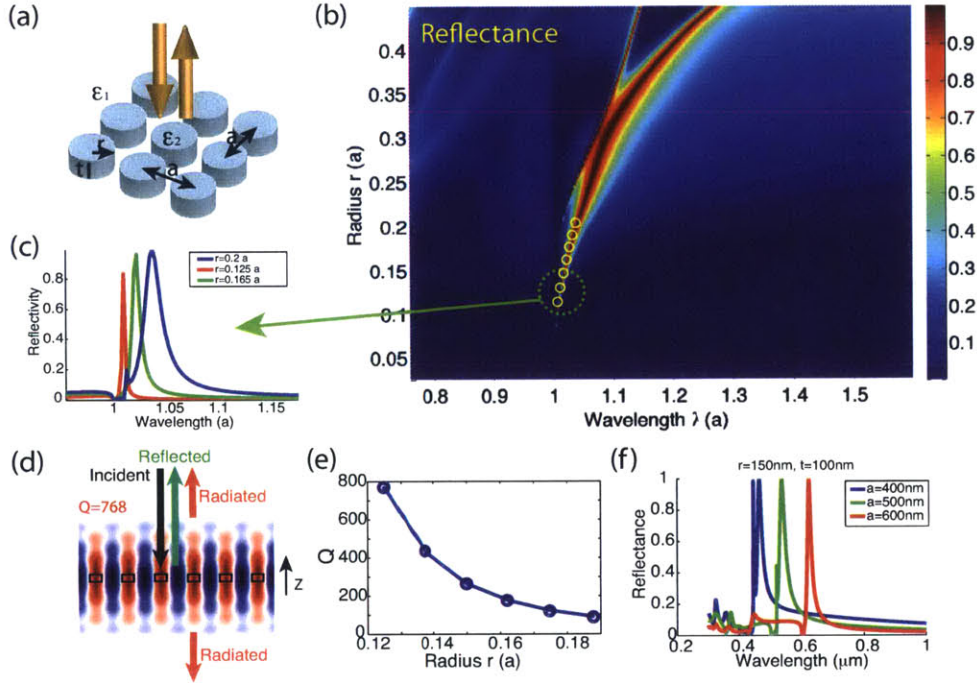


Figure 3-1: **Light reflectance assisted with Fano-resonance** (a) Light with random polarization incident on a periodic array of nano-rods. The dielectric constant of the nano-rods is set to be  $\epsilon_2 = 4$  ( $\text{Ta}_2\text{O}_5$ ) and the surrounding medium  $\epsilon_1 = 1$  (vacuum). (b) Reflectance spectra versus different radii  $r$  of the rods with height  $t = 0.25a$ . The reflectance peaks are the result of interference between the directly reflected light and radiated light from the resonant modes. The yellow rings correspond to the locations of the theoretically simulated resonant modes. (c) Example of reflectance peaks caused by Fano-resonance for structures with  $r = 0.125a$ ,  $r = 0.165a$  and  $r = 0.2a$ . (d) Vertical slice of the spatial distribution of the electric field for the resonant mode responsible for the reflectance peak with  $r = 0.125a$  in (c). (e)  $Q$  values for the resonance modes versus the rod radius. (f) Shift of the reflectance peak when periodicity  $a$  is varied, while the rod radius  $r = 150\text{nm}$  and rod height  $t = 100\text{nm}$  are fixed.

lar dependence. Since the location of the reflection peaks strictly follow the resonance modes inside the photonics crystal (PhC) slab, under certain conditions (see Supplementary), the reflection peak can be designed to have very weak angular dependence. Such near-omnidirectional reflective color is hardly observed in other structural coloration mechanism, and would be useful in many applications.

Furthermore, since the resonant mode of the photonic crystal is directly related to the periodicity of the lattice, one can actively tune the location of the reflectance peak simply by changing the period  $a$  of the structure (Fig. 3-1f).

### 3.3 Experimental Demonstration of Structural Colors with Fano-Resonances

As a proof of concept, we first realize samples that have resonance-induced, *static* color in the red-to-NIR regime. In the next step, we experimentally realize the same structures on elastic substrates (PDMS) and demonstrate their *dynamic* tunability by varying the periodicity  $a$ .

The target structure to achieve Fano resonance consists of rods of a high-index material (Si) on a transparent substrate. In our first experiment, the structures proposed in Fig. 3-1 were fabricated on amorphous SiO<sub>2</sub> (glass) substrates, with two different periods of 450 nm and 500 nm, radius from  $r = 115$  to  $r = 125$  nm, and height  $t = 65$  nm. The radius and the thickness of the rods were optimized to support a resonant mode with a  $Q$  low enough to produce a significant color effect. In order to get a good optical effect, it is critical that the rods have a high index of refraction while having low absorptivity. That is why amorphous Si was used for the rods.

For the static color samples, fused silica substrates were cleaned and a layer of 65 nm of Si was deposited by plasma enhanced chemical vapor deposition (PECVD) at a substrate temperature of 200°C. The refractive index and thickness of the Si layer were confirmed by spectroscopic ellipsometry to be  $n = 4.3$  at 600 nm and 4.0 at 700 nm, while the imaginary part is below  $\kappa = 0.4$  at 600 nm and vanishes at

700 nm.

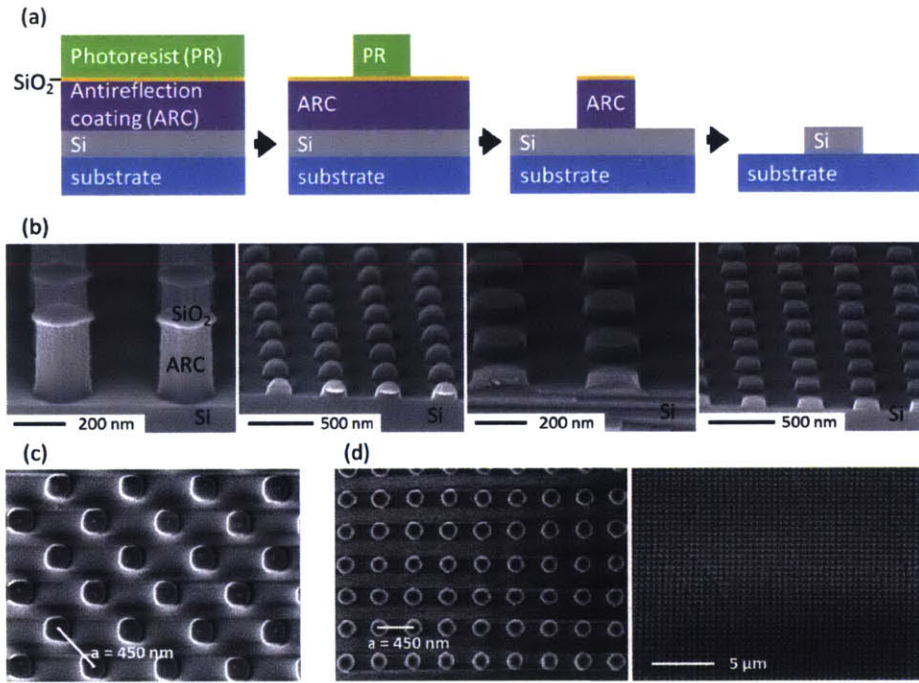


Figure 3-2: **Fabrication process:**(a) Schematic outline of the process flow: Deposition of the Si layer and lithography layers, pattern definition by interference lithography and pattern transfer by RIE. (b) Scanning electron micrographs of the process steps: Sample after RIE of the ARC, after RIE of the Si layer and after ashing of the remaining ARC (from left to right), cross sections taken from test samples on Si substrates. (c) Final Si rods on glass substrates and on (d) PDMS.

The fabrication process of the periodic structures was based on interference lithography (IL) using a trilayer process [122, 123] as shown in Fig. 3-2. IL is a relatively inexpensive, fast and scalable maskless lithography method, which relies on the interference pattern generated by two coherent light sources to define 1D and 2D periodic patterns in a single plane, and is easily scalable to large exposure areas. The lithography layer stack consisted of an antireflective coating (AZ BARLi, 200 nm), a thin layer of SiO<sub>2</sub> (20 nm, deposited by electron beam evaporation) to protect the anti-reflective coating (ARC) during reactive ion etching (RIE), and PFi-88 (Sumika, 200 nm) as a negative photoresist. The IL was done using a Lloyd's mirror setup with a 325 nm HeCd Laser. The periodicity of the pattern is defined by the interference angle,

and the exposure was performed twice, with the substrates rotated by  $90^\circ$  between exposures to create a square array of cylindrical rods in the negative resist. After development of the photoresist and RIE of  $\text{SiO}_2$  and ARC, the pattern was transferred to the Si layer by RIE using a  $\text{CF}_4/\text{O}_2$  chemistry. In the end, the remaining ARC was removed by plasma ( $\text{O}_2$ ) ashing.

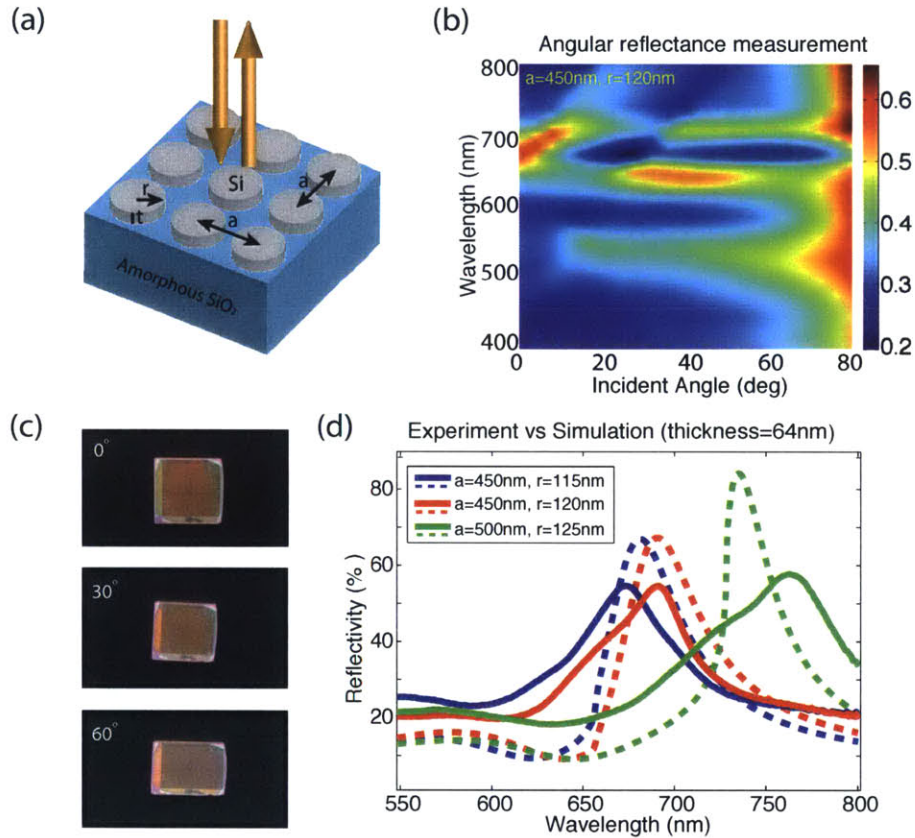


Figure 3-3: **Si rods on amorphous silica wafer** (a) Illustration of the simulated and fabricated structure. (b) Measured of reflectance spectra of a sample with  $a = 450\text{nm}$  and  $r = 120\text{nm}$  over all viewing angles. (c) Photographs of the fabricated sample with  $a = 450\text{nm}$  and  $r = 120\text{nm}$  at different viewing angles. The sample's color appeared red irrespective of the viewing angles (Rod structure in the center, edge area only partially exposed due to lithography setup) (d) Experimental demonstration of color control: Measured (solid lines) and simulated (dashed lines) reflectance spectra of structures with different geometries of the periodic Si rods fabricated on amorphous silica substrates.

The fabricated sample appeared red in color over a wide range of viewing angles (Fig. 3-3c). The reflectance of the samples at different incident angles was measured

using an ultraviolet-visible spectrophotometer (Cary 500i). In Fig. 3-3b we show that the reflection peaks indeed depend weakly on the incident angles, as discussed above. Clearly that there is a resonance band around 650-700nm for small angles, which decreases for angles  $< 10^\circ$ , while there is another resonance band contributing for angles  $> 20^\circ$  in the wavelength around 650nm. The resulting reflection spectrum consists of two different resonance bands, which allow us to observe similar resonant reflectance color for a wide range of angles (similar to the effect in Supplementary). The reflectance spectra at normal incidence of samples fabricated with different periodicity  $a$  and rod radius  $r$  are shown in Fig. 3-3d. The resonance wavelength clearly increases as  $r$  and  $a$  increases as predicted. Compared with the RCWA simulation result (dashed line), the experimental Fano reflectance peaks are broadened due to the non-radiative loss in the structure, possibly due to material absorption and fabrication inaccuracies, in particular local variations in the geometry. Nevertheless, we observed a 3-fold increase in sample's reflectance around the resonance wavelength. Due to the dramatic increase of the absorption in amorphous Si at smaller wavelengths, this particular structure's Fano resonance effect can only be observed at wavelengths longer than 600 nm. However, with suitable lossless materials one should be able to demonstrate this effect also in the lower wavelength regime.

### 3.4 Dynamical Tuning of Structural Colors

In our second experiment, we demonstrated dynamic color tuning using the same Fano resonance mechanism. In order to achieve the desired effect, the structures were fabricated on polydimethylsiloxane (PDMS) substrates (Fig. 3-4) instead of glass substrates. To this end, PDMS (Sigma-Aldrich, approx. 200  $\mu\text{m}$  thick) was spin-coated on 5 cm silanized Si wafers, and annealed at 150°C for 30 minutes. The Si substrates serve as a support in nanofabrication, and can be removed afterwards by peeling off the thick PDMS layer. The PDMS was surface treated by  $\text{O}_2$  ashing (200 W) to enhance adhesion and resistance to wet chemical processing, which resulted in some surface damage and macroscopic cracking in the PDMS surface. On the

prepared PDMS substrates, a layer of 65 nm of Si was deposited by PEVCD at a substrate temperature of 150°C.

The fabrication process of the Si rods on the prepared PDMS substrates was similar to that on the glass substrates (Section 3). To achieve higher fabrication accuracy, a Mach Zehnder setup was used for the IL on the PDMS substrates, instead of the Lloyd's mirror. [124–126].

In the fabrication process it must be taken into account that PDMS is temperature sensitive and elastic, and also highly sensitive to wet chemical processing. While the deposition of Si on glass was straightforward, the PECVD on PDMS resulted in a dull Si surface, on which the cracks from ashing were plainly visible, with considerable surface roughness visible under a microscope. Nevertheless, the Si layer on PDMS appears to be a sufficiently flat layer on a nanoscopic scale, and the optical properties are close to those of amorphous Si. As a result of the difficult fabrication process on the elastic substrates, the achieved structures have an acceptable nanoscopic accuracy (Fig. 3-2), but rather low macroscopic uniformity.

In order to achieve isotropic variation of the periodicity  $a$ , the PDMS sample must be stretched isotropically. To this end, the sample was fixed on a black balloon with radius  $R_1$  (Fig. 3-4b) much larger than the sample size. The balloon was then gradually expanded to  $R_2$ . Through this method, the periodicity of the sample was isotropically increased from  $a_1$  to  $a_2 = a_1 \cdot \frac{R_2}{R_1}$ . The reflectance spectrum at normal incidence was measured with the same ultraviolet-visible photospectrometer as the one used to measure the static colors, and is shown in Fig. 3-4d. Compared with the RCWA simulation result (dashed line in Fig. 3-4c), which was obtained using the measured refractive index dispersion of the deposited Si and assuming a constant rod radius, the spectral position of the experimental reflectance peaks and the simulated spectra match well. The spectral shift of the measured reflectance peak was 32 nm when the sample is stretched by approx. 10 %. The magnitude of the measured reflectance is lower than simulated due to the fabrication inaccuracies mentioned above. Since the Si layer on PDMS was not quite flat after Si deposition, interference lithography was problematic: there was some variation in rod size over a length scale

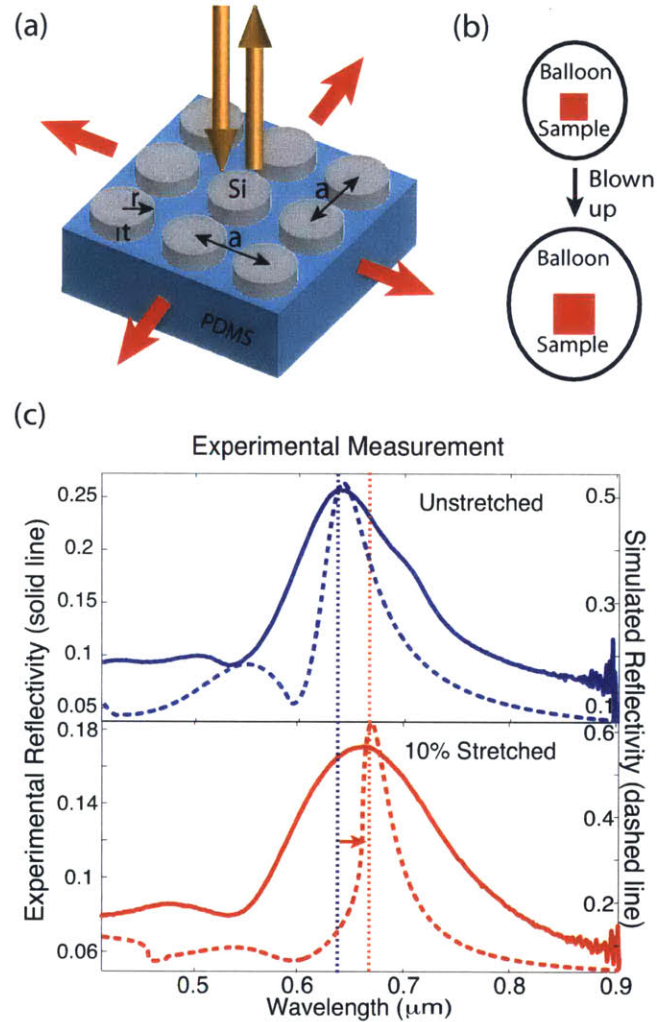


Figure 3-4: **Si rods on PDMS** (a) Illustration of the simulated and fabricated structure. (b) The periodicity  $a$  of the rod lattice can be adjusted by stretching the PDMS. In order to simulate isotropic stretching, the sample is fixed on a balloon, which is gradually blown up. (c) Dynamic color control: Measured (solid lines) and simulated (with ideal structure, dashed lines) reflectance spectra of silicon rods with  $a = 450\text{nm}$  and  $r = 100\text{nm}$  on polydimethylsiloxane (PDMS) before and after stretching by 10%.

of a couple of periods, together with a variation of the level of the rods, which could have had an adverse effect on the observation of Fano resonance. Also, the RIE of the Si layer and the mask layer removal by ashing might have damaged the PDMS surface to some extent and led to the formation of  $\text{SiO}_2$  on the PDMS surface.

Due to those fabrication reasons, in the stretchable samples the Fano resonance can be best observed (with the experimental peak follows the simulated peak) when the stretching is less than 10%. However, we did not observe any degradation of the samples or their optical response after repeated stretching experiments. Another layer of PDMS spin-coated on top of the structure could also add additional stability to the structures during stretching. As mentioned before, it is possible to use different materials and other designs to achieve the same Fano resonance effect also in other wavelength regions. Very repeatable and controlled stretching mechanisms [100,127] are available. Therefore, we believe that a tunable spectral response over a wide wavelength regime could be achieved in a controlled and repeatable way using the proposed Fano resonance effect.

### 3.5 Conclusion

In this Chapter, we propose a structural color mechanism that uses the optical Fano resonance effect of light on a periodic surface structure. To this end, we have designed and fabricated a structure of periodic high-index rods on low-index substrates that show Fano resonance of the reflected and guided modes in the visible wavelength range. The predicted Fano resonance maxima were observed in the reflectance spectra on glass and PDMS substrates, with weak angular dependence. Moreover, dynamical color control was achieved by isotropically stretching the elastic PDMS substrates with the fabricated Fano structure, resulting in a shift of reflection peaks in agreement with with simulation.

This mechanism for structural color and the geometry demonstrated is very versatile and can be specifically tailored for different applications e.g. in displays or light emitting devices. In particular, the Q-factor and therefore the bandwidth of

the resonance can be tuned to achieve a broad reflection bandwidth for displays or narrow reflectance bandwidth for light emitting or lasing applications. In addition, the designed structure shows good performance over a broad range of viewing angles.

The proposed method has the potential to lead the way to static and dynamic color control for a broad range of applications. The resonance effect achieved with these structures can be further optimized by improving the fabrication mechanism to achieve better accuracy and uniformity. Furthermore, the spectral range over which the effect and the reflectance color can be tuned could be extended by using materials that are lossless in the full visible spectrum, such as  $\text{TiO}_2$  or  $\text{Ta}_2\text{O}_5$ .

## Chapter 4

# Substrate-Independent Light Confinement in Bioinspired All-Dielectric Surface Resonators

### 4.1 Light Confinement on Dielectric Photonic Slab Resonator

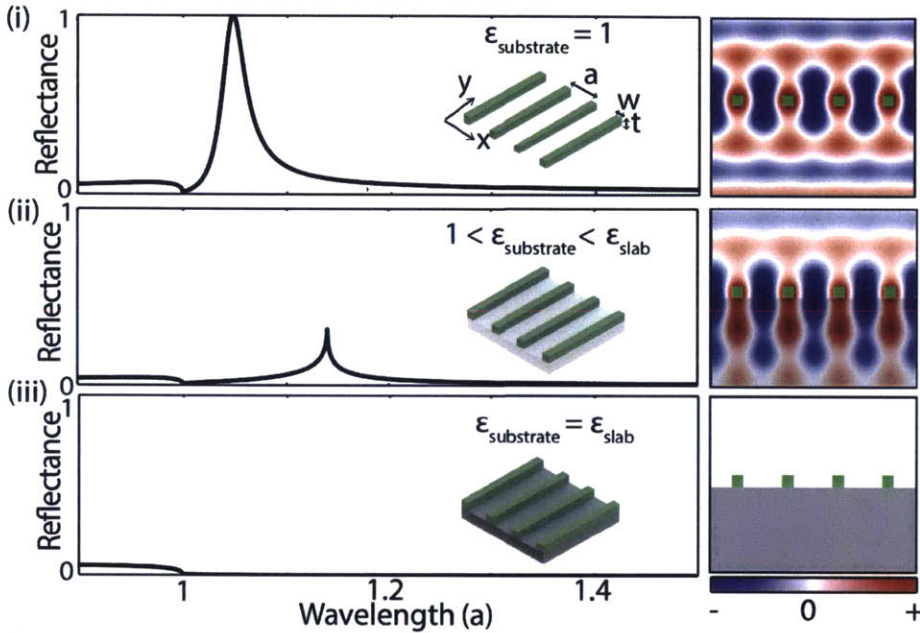
Interaction of light with periodic photonic structures has contributed to rapid advances in our ability to control light [9,128], which has led to many applications, including photonic bandgap fibers [129,130], light management for photovoltaics [131], and angular selective broadband reflectors [2,25]. Among the many photonic crystal structures, photonic crystal slabs (PhC slab) are one of the most widely used geometries due to their ease of fabrication and integration. Traditionally, a PhC slab consists of a high-index guiding layer with periodic in-plane patterns. These structures can support guided resonances that are strongly confined to the slab but also couple to external radiation [132,133]. The ability to channel light from the slab to the external environment has been used in optical devices such as photonic crystal surface emitting lasers [134] and light-emitting diodes [135]. However, when a PhC slab is in direct contact with a substrate, the resonance modes inevitably become less confined

as the index contrast between the slab and the substrate decreases. In this section, we present an all-dielectric surface structure that supports well-confined resonance modes without index contrast between structure and substrate; these resonances are effectively substrate-independent.

When a PhC slab is on a substrate that has a higher refractive index than the environment, the resonance modes inside the slab typically couple to the substrate, reducing their lifetimes. To illustrate this phenomenon, consider a 1D dielectric grating under vacuum [Fig. 4-1(a)]. With no substrate, the grating supports a first-order resonance mode whose energy is concentrated within the slab. Reflection spectra provide experimental evidence of these resonance modes. When the PhC slab is illuminated from above, the radiated light from the resonance mode interferes with the directly reflected light, forming a sharp optical Fano resonance reflection peak [6, 117, 132]. As the dielectric constant of the substrate increases, two factors increase the radiation rate of the resonance [136]. First, the number of radiation channels increases. Second, the impedance mismatch between the slab and the substrate decreases, making the radiation stronger for each channel. As a result, the lifetime of the resonance mode is typically reduced. The mode leakage increases with the dielectric constant of the substrate until no resonance modes are supported once the dielectric constant of the substrate equals that of the slab. At this point, the resonant properties of the slab are no longer observable, as shown in Fig. 4-1(a(iii)) [137]. Furthermore, the resonances shift spectrally when a substrate is introduced due to the modified effective dielectric constant.

To reduce the substrate leakage, metals or high-index dielectric materials are typically used. While plasmonics promise control of light on the subwavelength scale, losses in the optical and infrared regions often significantly limit mode lifetimes and device performance [140]. A small number of high-index dielectrics, such as silicon, are used to efficiently guide light in the telecommunication wavelength regime, but these materials are lossy at visible wavelengths. Materials that have low absorption in the visible spectrum, such as SiN and TiO<sub>2</sub>, have comparatively low dielectric constants. While low-index waveguides have been demonstrated using photonic band gaps or

**(a) Traditional photonic crystal slab**



**(b) Butterfly inspired surface structure**

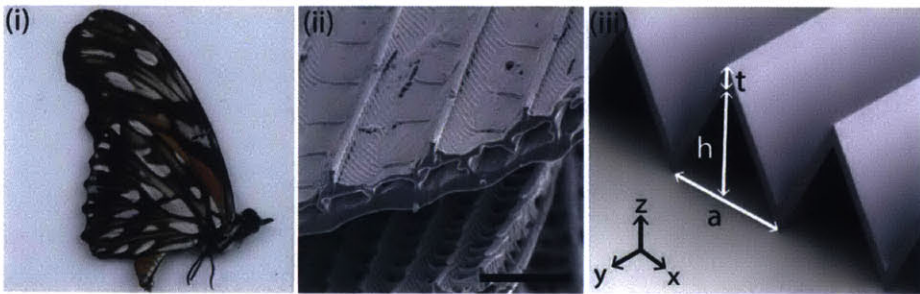


Figure 4-1: **Illustration of resonance mode in grating and bioinspired zigzag structure.** (a) Left panel shows rigorous coupled wave analysis (RCWA) simulation of normal incidence reflectance of a grating with dielectric constant  $\epsilon_{\text{slab}} = 2.235$  on substrates with dielectric constant (i)  $\epsilon_{\text{substrate}} = 1$ , (ii)  $\epsilon_{\text{substrate}} = 1.3$ , and (iii)  $\epsilon_{\text{substrate}} = 2.235$  [1, 138]. In each case, the grating is identical, with periodicity  $a$ , thickness  $t = 0.25a$ , and width  $w = 0.25a$ , and the incident light polarized in the  $y$ -direction. In the right panel (i) and (ii) show finite difference time domain (FDTD) mode profile ( $E_y$ ) [120, 139]. (iii) shows no resonance mode is supported due to strong leakage to the substrate. (b) (i) Photograph of the Dione juno butterfly's wings. (ii) SEM image of the cross section (focus ion beam milled) of a cut silver scale and wing substrate, showing that the scale body forms a periodic pattern on a substrate with air gaps. Scale bar is  $2 \mu\text{m}$  (iii) Schematic illustration of the abstracted zigzag structure characterized by periodicity  $a$ , height  $h$ , and thickness  $t$ .

index contrast [117, 141–143], the trade-off between substrate leakage and optical loss seems inevitable for surface resonators in the visible spectrum. Overcoming

this constraint is important for many applications, such as on-chip biosensing, which relies on low optical absorption in water [144]. In light of the limitations of traditional PhC slabs and their alternatives, we introduce a new class of bioinspired, low-index surface resonators that uses periodic air gaps to support resonance modes without index contrast between the structure and the substrate.

## 4.2 Bio-inspired Surface Resonator

Photonic crystal structures in butterfly wings use low-index biological materials to produce dramatic colors [145] and have been fabricated for optical devices [146, 147]. We study the silver scales on the *Dione juno* butterfly as an inspiration for a surface resonator with low index contrast. A scanning electron micrograph of the cross section of the silver scales and wing substrate shows two ridged cellular lamina with periodic connections [Fig. 4-1(b(ii))]. If the periodic structure interacts with light, the air gaps between the two laminae may reduce the radiation of a top-layer resonance into the underlying lamina structure, despite the low index contrast between the two.

Inspired by the scales, we abstract the microscopic structure to a zigzag surface structure characterized by its height ( $h$ ), thickness ( $t$ ), and periodicity ( $a$ ), whose structure mimics the periodic air gaps in the scales [Fig. 4-1(b(iii))]. This structure can be fabricated using direct laser writing or with controlled buckling for large scale fabrication [148, 149]. Moreover, the zigzag structure may be suitable for dynamic tuning if fabricated on a stretchable substrate, which merits further investigation.

We study the resonant properties of the zigzag structure with the finite difference time domain (FDTD) method [120], using a freely-available software package [139]. We use periodic boundary conditions in the plane of the periodicity and perfectly matched layer (PML) boundary conditions above and below the structure. A low-index acrylic ( $\epsilon = 2.235$ ) zigzag structure was chosen that produces a strong reflection peak on high-index substrates. The structure has periodicity  $a$ , height  $h = 0.88a$ , and thickness  $t = 0.22a$ . Reflection spectra were calculated for the zigzag structure on three substrates: vacuum ( $\epsilon = 1$ ), acrylic ( $\epsilon = 2.235$ ), and high-index ( $\epsilon = 6$ )

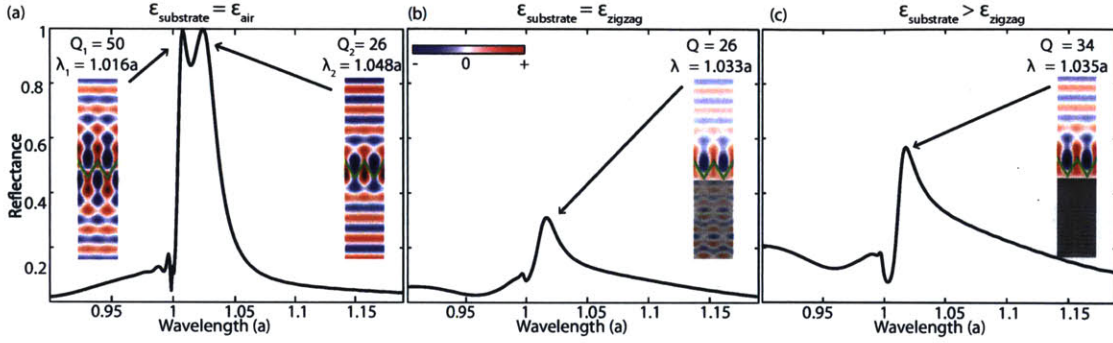


Figure 4-2: **Numerical simulation of the zigzag structure.** FDTD simulation of the reflectance of acrylic  $\epsilon_{\text{zigzag}} = 2.235$  zigzag structure with periodicity  $a$ , height  $h = 0.88a$ , thickness  $t = 0.22a$ , and dielectric constants (a)  $\epsilon_{\text{substrate}} = \epsilon_{\text{air}} = 1$ , (b)  $\epsilon_{\text{substrate}} = \epsilon_{\text{zigzag}} = 2.235$ , (c)  $\epsilon_{\text{substrate}} = 6 > \epsilon_{\text{zigzag}}$ . The incident light is polarized in the y-direction. Inset in each figure: FDTD mode profiles ( $E_y$ ) and Q-factors of the resonance modes at wavelength equal to the first-order Fano resonance peaks indicated.

[Fig. 4-2]. Using a low-storage filter diagonalization method, the spectral location and quality factors (Q-factor  $\approx \omega_0/\gamma$ , where  $\omega_0$  and  $\gamma$  are the frequency and width of the resonance) of the supported resonance modes were determined for each zigzag-substrate combination [121]. The wavelengths of the resonances agree well with the resonant reflection peaks, indicating that the peaks are caused by optical Fano resonance. The mode profiles of the resonances are shown in the inset of Fig. 4-2.

The numerical results show that for  $\epsilon_{\text{substrate}} = 1$ , the acrylic zigzag structure supports two resonance modes at wavelengths  $\lambda_1 = 1.016a$  and  $\lambda_2 = 1.048a$ . For  $\epsilon_{\text{substrate}} > 1$ , one resonance remains near this wavelength range, whose spectral location is approximately constant for different substrate dielectric constants: on the acrylic substrate,  $\lambda = 1.033a$ , and on the high-index substrate,  $\lambda = 1.035a$ . This resonance remains for substrates with  $\epsilon_{\text{substrate}} \geq \epsilon_{\text{slab}}$ , which is not possible in traditional PhC slabs. The other resonance leaks into the substrate. Additionally, in traditional PhC slabs, the resonant wavelength undergoes a large shift as the substrate index increases [Fig. 4-1(a)]. The constant mode location in the zigzag structure suggests that the resonance mode is weakly interacting with the substrate. This is confirmed by the mode profiles inside the zigzag structure, which show that the resonance mode is localized away from the substrate and is concentrated around the horizontal plane

containing the top points of the zigzag due to the large volume of high-index material contained away from the substrate. Therefore, the coupling is reduced and the effective index that the mode experiences is roughly constant [Fig. 4-2(b-c)]. Unlike in traditional photonic crystal slabs, the Q-factor increases slightly for higher-index substrates because the reflection at the air/substrate interface increases. The robustness of the Q-factor and the resonance peak location suggest that these resonances may be useful for devices that work on a variety of substrates.

The substrate-independent resonance property is not unique to the zigzag geometry. A different abstraction of the wing structure, a lamina with periodic connections to the substrate, also shows a sustained resonance on high-index substrates [Fig. S1]. Again, this structure supports a resonance mode away from the substrate with low coupling because the slab material is concentrated away from the substrate [150]. To better understand this physical system, we note that this structure and the zigzag both contain periodic air gaps between the mode and the substrate. Therefore, the surface resonator with self-contained air gaps is similar to a suspended traditional PhC slab, where the distance between the slab and the substrate determines the coupling [Fig. S2].

### 4.3 Experiment

To verify the existence of such resonances, we experimentally measured the reflection spectrum of zigzag structures on a substrate with little index contrast and observed the optical Fano resonance peaks caused by the predicted resonance modes. The experiment was conducted in the visible spectrum, where alternative methods (plasmonics and high-index dielectrics) typically perform poorly because of losses. A zigzag structure with  $\epsilon = 2.31$  was optimized to support one set of third-order resonances in the visible spectrum when on a fused silica ( $\epsilon = 2.18$ ) substrate [Fig. 4-3(a)]; third-order resonances were necessary to study reflection peaks in the visible spectrum because the spatial resolution of the fabrication process is 300 nm. Zigzag structures with thickness  $t = 0.3 \mu\text{m}$ , height  $h = 1.6 \mu\text{m}$  and periods 1.6,

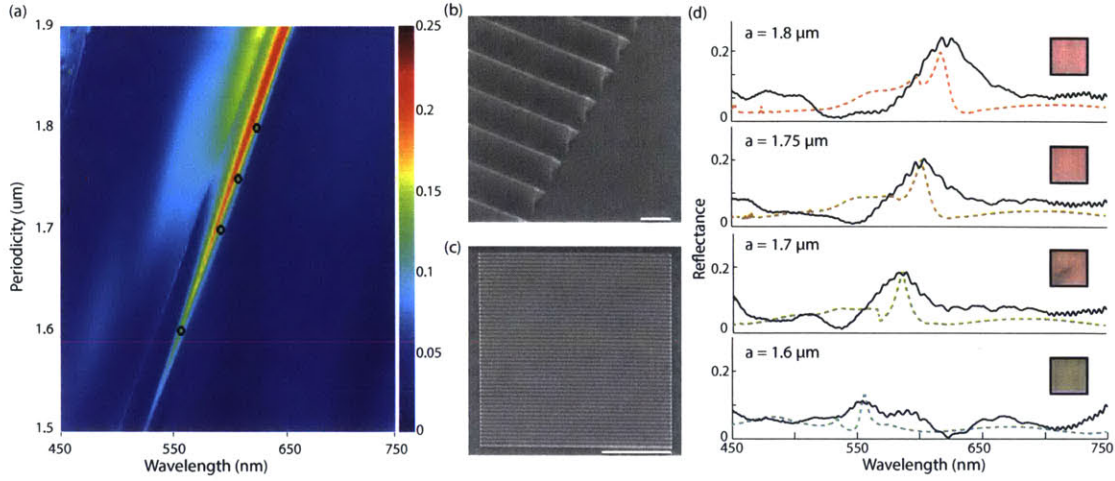


Figure 4-3: **Experimental design and measurement.** (a) RCWA simulation of the reflectivity into the normal direction of a zigzag structure with different periodicities  $a$  and fixed thickness  $t = 0.3 \mu\text{m}$  and height  $h = 1.6 \mu\text{m}$ . Incident light is unpolarized. The black circles indicate the spectral location of third-order resonance modes inside the zigzag structure at each fabricated periodicity, determined by a low-storage filter diagonalization method. (b-c) SEM image of the cross section and the top view of a fabricated zigzag structure on a fused silica substrate. Scale bar is  $2 \mu\text{m}$  in (b) and  $50 \mu\text{m}$  in (c). (d) RCWA simulation (dashed line) and experimental measurement (solid line) of the reflectivity into the normal direction of the fabricated zigzag structures with different periodicities. Incident light is unpolarized. The colors of the dashed lines correspond to the perceived colors. The images inside the black boxes are the microscope photographs of the measured samples ( $50 \mu\text{m} \times 50 \mu\text{m}$ ).

1.7, 1.75, and  $1.8 \mu\text{m}$  were fabricated using direct laser writing. A fused silica substrate ( $\epsilon = 2.18$ ) was coated with a liquid IP-L 780 photoresist, which was exposed to a 780 nm excitation laser with a pulse width of 100 fs and a repetition rate of 80 MHz [148]. The sample was then developed with 1-methoxy-2-propanol-acetate. The photoresist, which forms the zigzag structure, has a dielectric constant  $\epsilon = 2.31$  after laser exposure. Samples of  $50 \mu\text{m} \times 50 \mu\text{m}$  were fabricated, which includes about 30 periods. Scanning electron micrographs show that zigzag patterns were achieved [4-3(b-c)]. Alternatively, large-area fabrication of zigzag surface structures may be possible using controlled buckling, which has produced PDMS zigzag micropatterns with wavelength of  $\approx 50 \mu\text{m}$  [149]. If the micropattern is attached to a substrate, this fabrication technique could be used to create large-scale spectrum filters.

Reflection measurements near the normal incidence of the zigzag structures were

performed using a microspectrometer (CRAIC QDI 2010) with a collection range of  $\pm 2^\circ$  [Fig. S3]. The imaging spot size was approximately  $40 \mu\text{m} \times 40 \mu\text{m}$ . The color of each structure is easily visible through the microscope [4-3(d)]. The measured reflectance spectra of samples fabricated with different periodicities are shown in Fig. 4-3(d), along with rigorous coupled wave analysis (RCWA) simulations of normal incidence reflection [1]. The experimental reflection peaks are broadened due to disorder-induced scattering and side leakage due to the finite size of the structure [151,152]. Additionally, the experimental peaks are higher than predicted due to the small range of collection angles around the normal direction. The dimensions of the zigzag structure are at the limit of the resolution obtainable from the direct laser writing process. Therefore, we expect some fabrication inaccuracies, which are more significant for smaller structures. Despite this limitation, we observe reflection peaks that agree closely with the numerical reflection spectra. The resonance wavelength increases with the period of the zigzag structures, as expected. The appearance of the reflection peaks experimentally validates the existence of well-confined substrate-independent resonances with low index contrast.

## 4.4 Applications

### 4.4.1 Structural Colors

The substrate-independent properties are useful for many applications. One application is a single-material, low-index structural color mechanism. Structural color has previously been produced using light interaction with bulk materials via mechanisms that include scattering [102], photonic crystals [107], and multilayer interference [104]. However, these techniques require thick bulk material to generate sufficient reflection. Plasmonic resonances have also been used to produce color in nanoscopically structured metal surfaces [112]. These techniques promise low thickness and a wide range of color, but the reflection contrast is low because metals are generally lossy in the visible spectrum. A Fano resonance structural color mechanism has been studied in

silicon PhC slabs [6], but was not previously possible with lossless low-index materials. This method creates strong reflection peaks for  $\lambda > 600$  nm, but increased absorption in silicon at smaller wavelengths reduced the spectral range of color. In contrast, the resonance in a dielectric zigzag structure persists on a substrate of the same material and produces broad Fano resonance peaks that are suitable for color in the full visible spectrum. The color can be selected via the periodicity of the zigzag, as has been shown in our experiment. Similar to previous silicon-based Fano resonance structural color results, the zigzag structure presented here could be further optimized for even stronger reflection peaks [6].

#### 4.4.2 Photonic Integrated Circuits

Substrate-independent resonances may also find applications in photonic integrated circuits (PICs), which perform a variety of optical functions on a single chip and have shown promise for many applications [153, 154]. While silicon dominates the semiconductor industry, PICs have been fabricated using a variety of host material systems that provide unique functionality based on their material properties [155]. A low-loss waveguide that operates using self-contained periodic air gaps, rather than relying on high index contrast between the waveguide and the surrounding medium, is an interesting alternative to the material-specific waveguide designs used today. Further, while resonance modes in plasmonic structures have limited quality factors due to absorptive losses, [133, 156, 157] the resonance mode lifetimes for substrate-independent waveguides depend only on substrate leakage and can be optimized geometrically. Optimization of slab with periodic air gaps that supports high-Q guided modes would further contribute to a new class of all-dielectric structures that have substrate-independent properties and work at visible wavelengths. As PICs become increasingly important for high-speed communication and efficient sensing, new methods for designing passive optical components may provide a way to overcome material constraints.

## 4.5 Conclusion

In this Letter, we introduce a new class of low-index bioinspired surface structures that support resonance modes on high-index substrates and without index contrast, which was not previously possible. We experimentally verify the existence of such resonances in the visible wavelength regime, and we identify potential applications for structural colors and light guiding.

## Supplementary

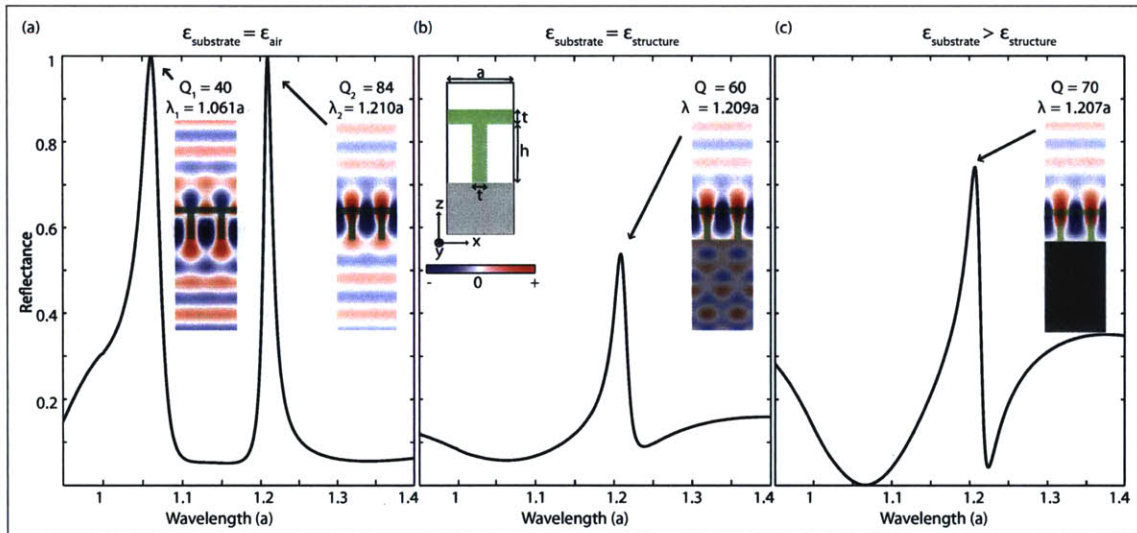


Figure S1: **Numerical Simulation of T-bar Structure.** FDTD simulation of the reflectance of an acrylic  $\epsilon = 2.235$  T-bar structure (see inset of (b)) with periodicity  $a$ , height  $h = 0.88a$ , thickness  $t = 0.22a$  on substrate with dielectric constants (a)  $\epsilon_{\text{substrate}} = \epsilon_{\text{air}} = 1$ , (b)  $\epsilon_{\text{substrate}} = \epsilon_{\text{t-bar}} = 2.235$ , (c)  $\epsilon_{\text{substrate}} = 6 > \epsilon_{\text{t-bar}}$ . The incident light is polarized in the  $y$ -direction. Inset in each figure: FDTD mode profiles ( $E_y$ ) and  $Q$ -factors of the resonance modes at wavelengths equal to the first-order Fano resonance peaks indicated.

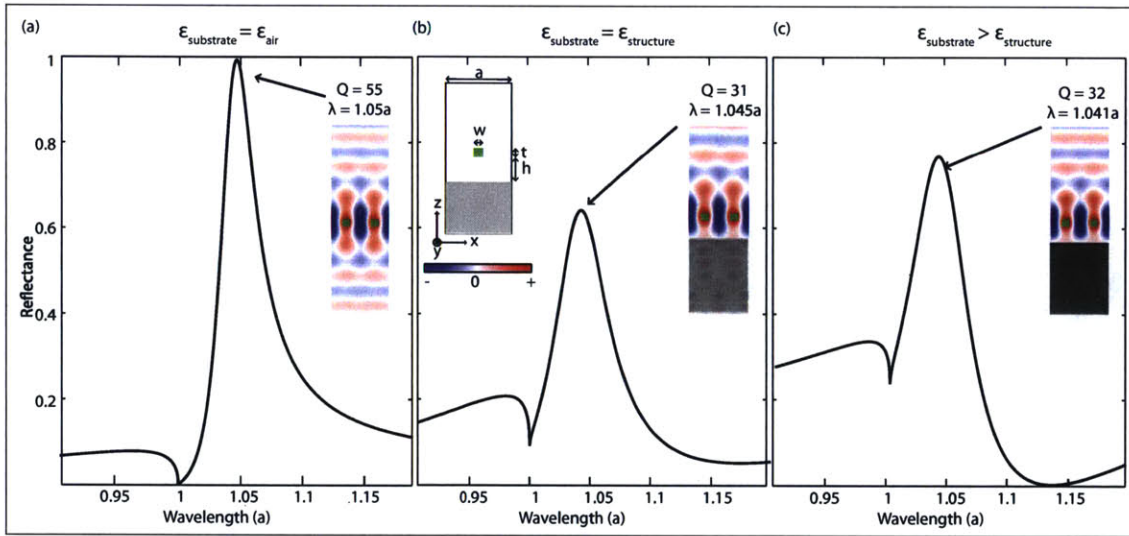


Figure S2: **Numerical Simulation of Suspended Grating.** RCWA simulation of the reflectance of an acrylic  $\epsilon = 2.235$  grating (see inset of (b)) with periodicity  $a$ , width  $w = 0.22a$ , thickness  $t = 0.22a$  suspended at  $h = 0.56a$  above a substrate with dielectric constants (a)  $\epsilon_{\text{substrate}} = \epsilon_{\text{air}} = 1$ , (b)  $\epsilon_{\text{substrate}} = \epsilon_{\text{slab}} = 2.235$ , (c)  $\epsilon_{\text{substrate}} = 6 > \epsilon_{\text{slab}}$ . The incident light is polarized in the  $y$ -direction. Inset in each figure: FDTD mode profiles ( $E_y$ ) and Q-factors of the resonance modes at wavelengths equal to the first order Fano-resonance peaks indicated.

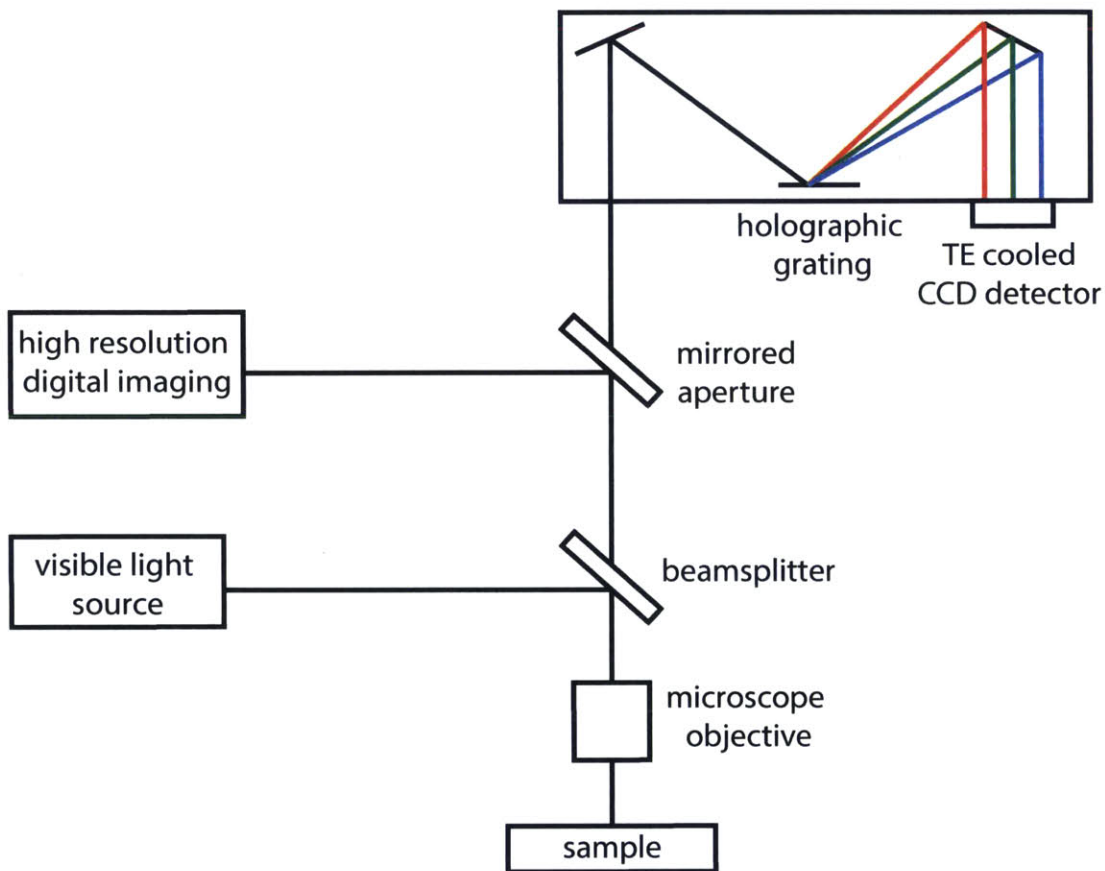


Figure S3: **Microspectrometer Setup for Reflectance Measurement.** Schematic of CRAIC QDI 2010 microspectrometer used to excite zigzag sample at normal incidence and collect reflected light at normal  $\pm 2^\circ$ .

# Chapter 5

## On-Chip Optical Neuromorphic Computing

### 5.1 Introduction

The brain, unlike the von Neumann processors found in conventional computers, is very power efficient, extremely effective at certain computing tasks, and highly adaptable to novel situations and environments. Artificial Neural Network (ANN), and area of research that has recently received an explosion of interests [158], are algorithms that mimic the signal processing architecture in the brain. Artificial Neural Network is composed of multiple processing layers to learn representations of data with multiple levels of abstraction. These methods have dramatically improved the state-of-the-art in speech recognition, visual object recognition, object detection and many other domains such as drug discovery and genomics.

Now, both the quantity and also the size of data files are growing rapidly, therefore computing speed and the power efficiency is the key on evaluating the performance of any machine learning algorithm. In real life applications, artificial neural networks can contain up to millions of units in each hidden layers. The sheer number of units make forward propagation the rate limiting step in many applications. Many efforts have been made to increase the computing speed of artificial neural networks. Among these methods, neuromorphic computing, where electronic devices are tweaked to have

optimized architecture for the kinds of computing for neural networks [159], is one of the most heavily invested techniques.

Photonic platforms offer an alternative approach to microelectronics. The high speeds, high bandwidth, and low cross-talk achievable in photonics are very well suited for an ultrafast ANNW processor. In addition, the high wall-plug efficiencies of photonics devices may allow such implementations to match or eclipse equivalent electronic systems in low energy usage. With the recent advances in quantum optical devices and on-chip nanophotonic circuit fabrication, we reasoned it is possible to design a viable on-chip optical neural network (ONNW) architecture. In this work [160], we will explain that conventional neural networks architecture can be entirely and equivalently represented by on-chip optical components. We will also experimentally demonstrate the on-chip neuromorphic optical computing, with the help of which we show that our optical neural networks are able to give similar accuracy performance on a standard evaluation dataset compared with result from conventional neural networks. Finally, we will show that in certain condition optical neural nets can be made at least 3 orders of magnitude faster in forward propagation than conventional neural nets in digital computers.

## 5.2 Optical Neural Network Device Architecture

Artificial neural network architecture contains an input layer, at least one hidden layers, and an output layer. In each layer, information propagate through neural network via linear combination (e.g. matrix multiplication) followed by nonlinear activation applied to the result from linear combination. In training an artificial neural network model, data are fed into the input layer, and output is calculated through the forward propagation step. Then the weighting parameter of each synapse (matrix entry) are optimized through the back propagation procedure.

In our ONNW design, we will use our integrable photonic device to do each of these two steps. Firstly, matrix multiplication in our ONNW is implemented using optical interference unit, and we will show that our optical system can implement any

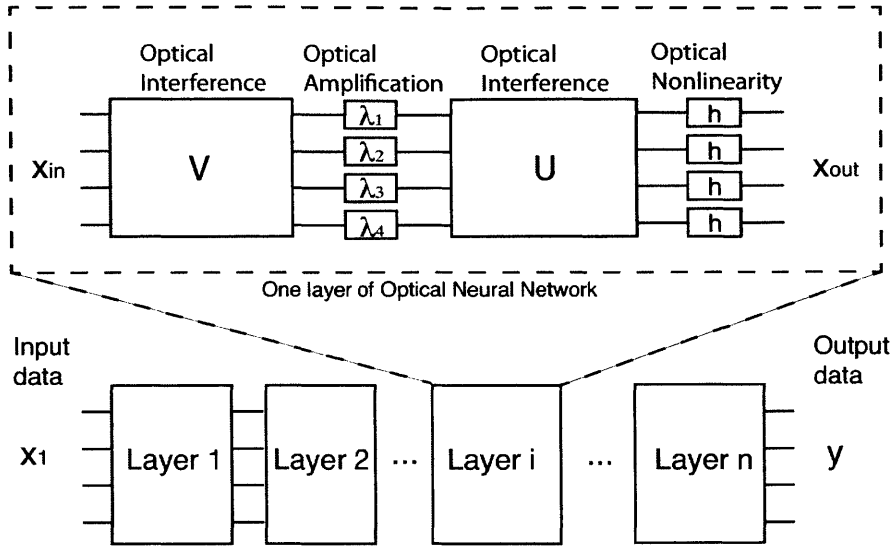


Figure S1: General Architecture of Optical Neural Network

weighting matrix  $\omega_i$ ; multiplication with real number entries. Secondly, the nonlinear activation is realized by optical nonlinearity unit in our ONNW, and we will show that our nonlinear function achieved with optical saturable absorption is very similar to the commonly used Rectified Linear Units (ReLU) nonlinearity. The general architecture of our optical neural network (ONNW) computing scheme is depicted in Fig. S1. In principle, our ONNW architecture can do computation in a way that is mathematically equivalent to the traditional artificial neural networks that we learned in class.

### 5.2.1 Optical Interference Unit

The weighted sum step in neural network computing can be realized optically using optical interference and amplification. In general, any arbitrary matrix can be generated using optical interference and linear amplification. To show how this is achieved, we will prove this statement through the following general steps.

1. **Singular Value Decomposition**, suppose  $\mathbf{M}$  is an  $m \times n$  matrix whose entries are real numbers  $K$ . Then there exists a factorization, called a singular value

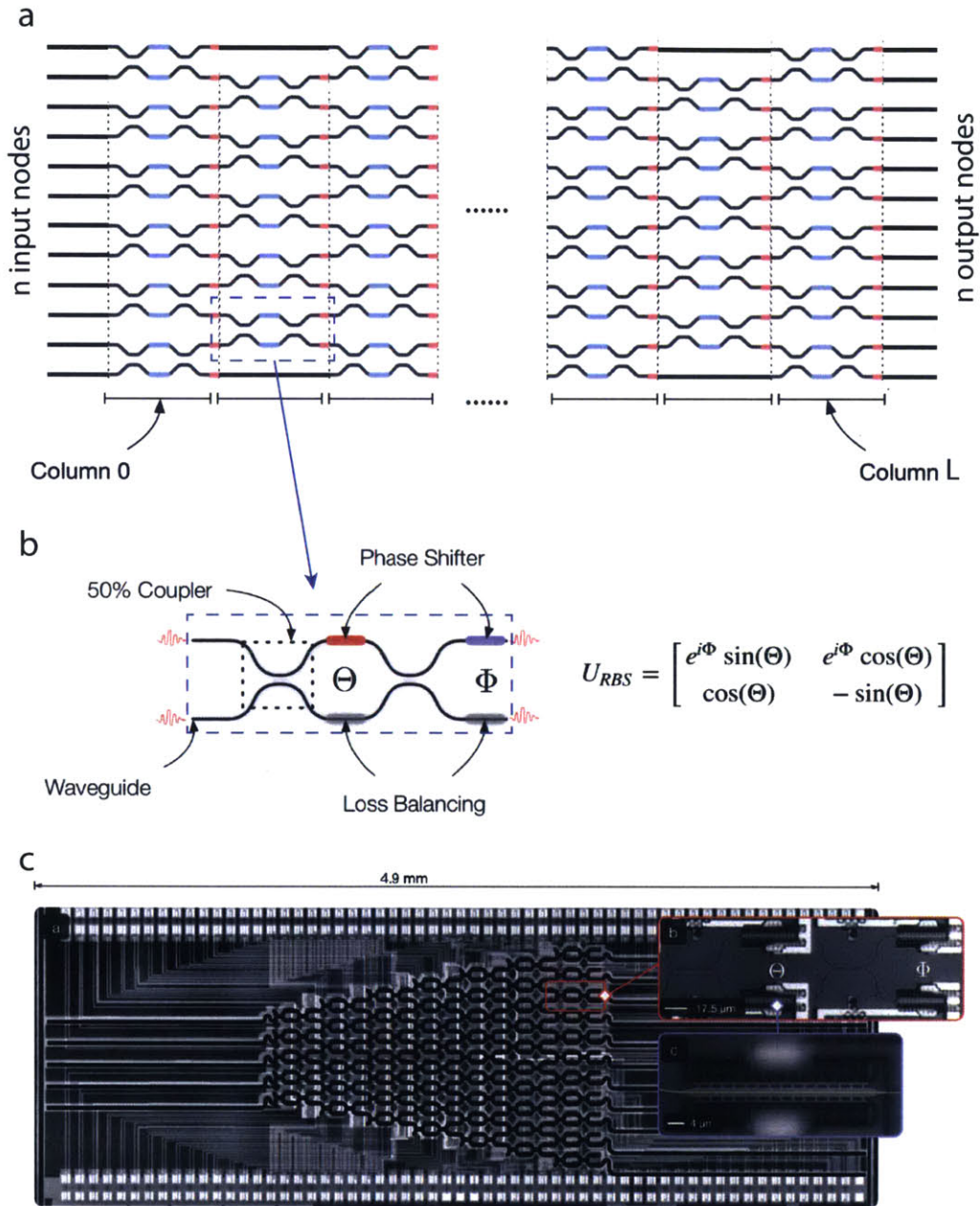


Figure S2: **Illustration of Optical Interference Unit** a. Schematic illustration of the entire optical interference unit, where the number of input  $n$  and the number of columns can be arbitrarily defined depending on the matrix this unit need to represent. b. Schematic illustration of a single Mach-Zehnder Interferometer and the matrix one single interferometer represent. c. Microscope image of an experimentally fabricated  $12 \times 12$  on chip optical interference unit [161–163] .

decomposition of  $\mathbf{M}$  [164], of the form

$$\mathbf{M} = \mathbf{U}\mathbf{\Sigma}\mathbf{V}^* \quad (5.1)$$

where

- $U$  is an  $m \times m$ , unitary matrix,
- $\Sigma$  is a  $m \times n$  diagonal matrix with non-negative real numbers on the diagonal, and
- $V^*$  is an  $n \times n$ , unitary matrix over  $K$ . (If  $K = R$ , unitary matrices are orthogonal matrices.)  $V^*$  is the conjugate transpose of the  $n \times n$  unitary matrix,  $V$ .

The diagonal entries,  $\lambda_i$ , of  $\Sigma$  are known as the singular values of  $\mathbf{M}$ . A common convention is to list the singular values in descending order. In this case, the diagonal matrix,  $\Sigma$ , is uniquely determined by  $M$  (though not the matrices  $U$  and  $V$ ).

2. **Optical Discrete Unitary Operator**, the unitary matrix  $U$  and  $V$  in Eqn. 5.1 can be obtained using a set of Mach-Zehnder interferometers, as shown in Fig. S2. Mathematically, it has been rigorously proved by Reck *et al* that any arbitrary (complex) unitary matrix can be represented by a set of Mach-Zehnder interferometers [165,166].
3. **Optical Amplification**, the diagonal matrix  $\Sigma$  in Eqn. 5.1 can be obtained using a set of optical amplifier [167]. An optical amplifier is a device that amplifies an optical signal directly, without the need to first convert it to an electrical signal. An optical amplifier may be thought of as a laser without an optical cavity, or one in which feedback from the cavity is suppressed. Optical amplifiers are important in optical communication and laser physics, and has been widely used with stable performance. In our particular ONNW setup, each optical amplifier is applied to an output node from  $V$  and amplify / de-amplify

the single by a constant factor  $\lambda_i$ .

### 5.2.2 Optical Nonlinearity

In a typical neural network, each "neuron" is a computational cell that takes an input and produce an output through a nonlinearity map (also known as activation function). This kind of nonlinear map is a necessary component in order to define a neural network. Some commonly used nonlinear functions are sigmoid, ReLU or tanh functions.

In modern optics, luckily, nonlinearity is a very common phenomena. Many materials respond to external light signals in a nonlinear way with respect to light intensity. Therefore, the nonlinear part of calculation in our Optical Neural Network can be achieved in many different ways as long as we utilize the inherent nonlinear property of the optical materials. Specifically, we want to design an optical system that takes an input power  $I_{in}$  and map that into the output power  $I_{out}$  through a nonlinear function  $f$  such that

$$I_{out} = f(I_{in})$$

Here we propose one of the most promising on-chip integratable optical system that can achieve the above propoerty, called *Optical Saturable Absorption* [168].

The saturable absorber nonlinear function can be modeled as:

$$\sigma\tau_s I_0 = \frac{1 \ln(T_m/T_0)}{2 \ 1 - T_m}, \quad (5.2)$$

where  $\sigma$  is the absorption cross section,  $\tau_s$  the radiative lifetime of the material that form the absorber,  $T_m$  is the maximum transmittance of the saturable absorber,  $T_0$  the initial transmittance and  $I_0$  the peak incident intensity.

In addition, note that optical saturable absorption is not the only optical nonlinearity, another common mechanism that can be implemented into all-optical transistors, switches, logical gates, and memory is *Optical Bistability* [169–171], and the nonlinear response it has is quite similar to the commonly used tanh function, as

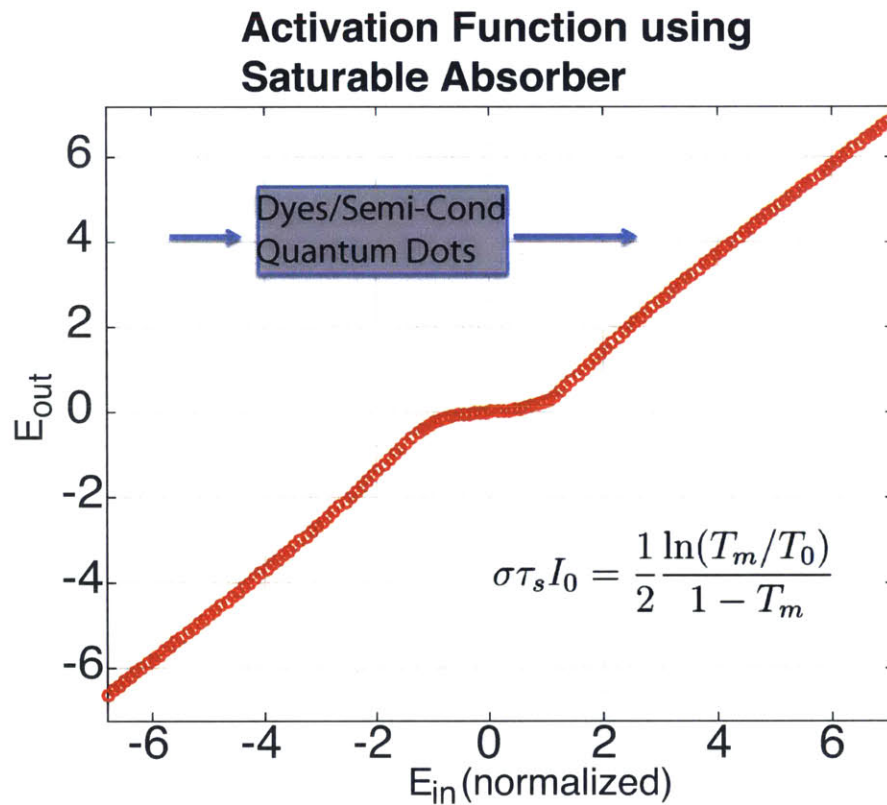


Figure S3: The optical response of a nonlinear optical system (saturable absorption) that perform nonlinear calculation. Inset: Schematic illustration of the saturable absorption system.

shown in Fig. S4.

### 5.3 Simulation

To demonstrate in simulation how our system works, we picked a relatively simple and standard vowel recognition problem for the system to solve. The training data was obtained from a standard dataset of log area ratio coefficients [172] from 90 different speakers speaking 10 different vowel phonemes [173]. These coefficients are derived from a windowed Fourier transform of the voice signal which essentially represents the power contained in different logarithmically spaced frequency bands. In a standard machine learning problem each spoken phoneme represents a different class, while the coefficients are the feature vectors. A subset of five coefficients and 5 vowels phonemes were selected for testing and training our optical neural network.

The exact optical nonlinearity using saturable absorber is used (Eqn. 5.2) in our algorithm, with such optical nonlinearity, and using the MZI networks described above, we are able to train our ONNW and achieve over 91% correction rate of the vowel recognition in the simulation. Note that this correction rate is already comparable to the network trained on conventional computers.

### 5.4 Time efficiency

One big hurdle in the field of ANNW is the speed. Since neural networks can be huge and sophisticated, even doing forward propagation can be time-consuming. The low speed limits the applications of neural network in many field, such as self-driving car, in which super fast and multiple image recognition is needed.

Optical neural networks have the intrinsic advantage of speed. Once all parameters have been trained and programmed on the nanophotonic system, forward propagation computing is performed optically on a passive system, which is only limited by the physical size and the spectral bandwidth of dispersive components (THz). In principle such a system can be 3 orders of magnitude faster than electronic neural networks,

and with much lower power consumption.

For the optical neural network system, we assume the propagation loss at the circuit level is negligible ( $< 2\%$ ), and we ignore power requirements for conversion between the electrical and optical domain. Our power consumption is mainly the amount of power required to support an optical nonlinearity (we need to amplify the incoming signal to this power level).

- **Computation Speed:** Assuming our system has  $N$  nodes and a 1 THz feed-in rate, then the floating point operation per second (FLOPS) of our system would be

$$R = 4N^2 \cdot 10^{12} \text{ FLOPS}$$

- **Power Consumption:** Assume the saturation power for our saturable absorber is  $p$  MW/cm<sup>2</sup>, the cross section for the waveguide is  $A = 0.5\mu\text{m} \times 0.5\mu\text{m}$ , then the total power needed to run the system is:

$$P = N \cdot p \text{ mW}$$

Therefore, the computation performance of ONNW will scale as:

$$R/P = 4 \cdot (N/p) \cdot 10^{15} \text{ FLOPS/W}$$

Typically,  $p$  is in the order of 1 [168, 174], in which case the computational power efficiency can be at least 3 orders of magnitude better than the current power efficiency of GPU and CPU ( $R/P \approx 10^{12}$  FLOPS/W). In addition, our current architecture assumes light only passes once in the system, so that all light will be absorbed in the end. If we can include light recycling and use some other nonlinearity with low absorption, then the efficiency metric above could potentially be even better.

## 5.5 Conclusion

In conclusion, we have theoretically proposed an on-chip optical system that use optical interference in dielectric waveguides to mimic neuron network computation. We then simulate our ONNW system and demonstrated that it can achieve as accurate result as conventional computers, while at the same time have potential to be 3 orders of magnitude more power efficient than conventional computers. Further experimental demonstration will need to be done to complete this work. This work might pave the way to a new generation of deep learning hardware.

## 5.6 Supplementary

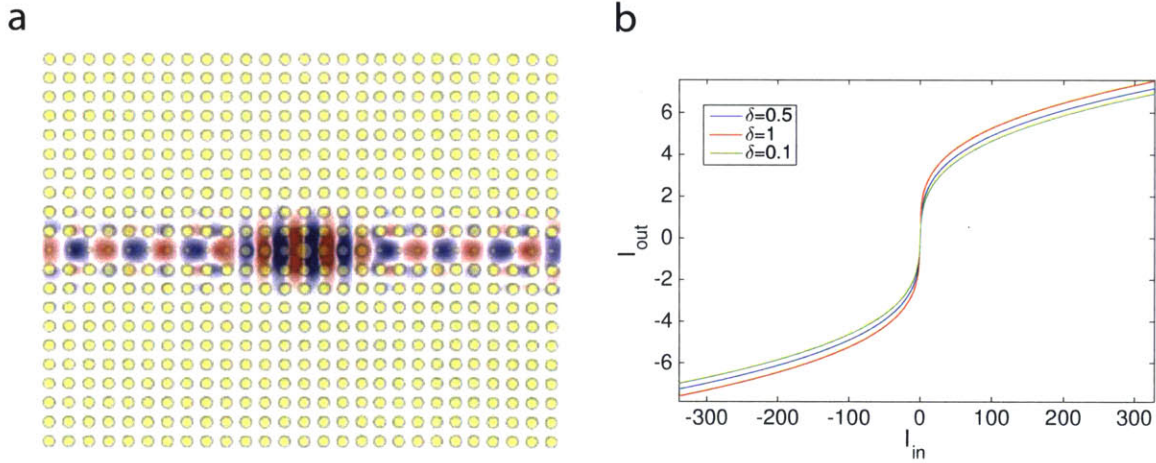


Figure S4: **Optical bistable system that perform nonlinear calculation** a. Schematic illustration of an optical system that show optical bistability. b. Optical response of such optical bistable system. In the work done by Soljagic *et al* [169], they showed that the nonlinear relationship of their optical bistable system (Fig. S4a) satisfy the following equation:  $\frac{I_{out}}{I_{in}} = \frac{1}{1+(I_{out}/I_0-\delta)^2}$ , where  $I_0$  is the "characteristic intensity" of the system, and is equivalent to a rescaling of both axes by the same factor. And  $\delta$  is a parameter that depends on the geometry of the nanophotonic system.

# Chapter 6

## Concluding remarks and future directions

In this thesis, we have explored several interesting behaviors of light in dielectric nanophotonic systems. Here, we discuss their implications and directions for future works.

### 6.1 Optical Broadband Angular Selectivity

Angularly selective devices based on geometrical optics have reached their limit due to the fact that their sizes need to be much larger than the operating wavelength. Nano photonics has opened many new opportunities in the development of broadband angularly selective materials, and is likely to have significant technological impact on this field. We have reviewed some of the most representative theoretical and experimental efforts in this field so far, namely using the micro-geometrical-optics, material birefringence, plasmonics, photonic crystals and metamaterials.

Although this field has already seen rapid progress in the past few years, we believe that we have only seen the beginning of this important topic. Over the coming years, we expect the following major topics to be explored in order for nanoscale broadband angularly selective materials to be widely applicable to the applications discussed in the previous sections.

- **Polarization dependence:**

The current realizations of the Brewster-angle-related methods described previously work only for one polarization. Generalization to both polarizations is a challenge, as the impedance-matching condition at the boundary depends on the polarization. This property applies generally to most PhCs and plasmonic structures irrespective of the dimensions. As a consequence, nano-phonic systems are typically polarization dependent.

However, this issue should not limit us from searching for broadband angularly selective systems that are independent of polarizations. For example, in our *et al*'s work [2], it is proposed that one can lift the restriction on polarization by using materials with nontrivial permeability  $\mu \neq 1$ . During the past decades, it has been demonstrated that metamaterials have a good potential for achieving this.

- **Angularly selective reflection/scattering:**

An opposite but related effect is the angularly selective reflection and scattering of broadband light. These can be useful for applications such as radiative cooling devices [175] and transparent displays [176]. The impedance-matching-based approaches we reviewed are suitable for selective transmission but not for angularly selective reflection or scattering. To the best of our knowledge, none of the existing technologies are capable of achieving such angularly selective reflection or scattering. Therefore, this topic remains to be explored.

- **Tunable selective angle:**

As we discussed in the solar cell applications section, angularly selective materials can increase the efficiency of solar cells and solar thermal systems by a significant amount. But, in order to implement such materials, the transparent window would have to face the sun at all times. Therefore, when using the angularly selective materials with fixed selective angle, a solar tracker would be necessary. However, solar trackers require extra components and energy input, hence are only used in some very large scale solar fields. On the other hand,

if one can develop a mechanism to dynamically tune the angle of the angularly selective material system, it will solve the major problem of solar tracking.

Following the rapid development of nanotechnology, the ability to control light at nanoscale has become an important topic and has attracted a tremendous amount of attention from both academia and industry. In particular, the field of broadband angular selectivity of light at the nanoscale has seen exciting progress in recent years. This new class of materials holds promising prospects for a host of applications, and thus deserves to be thoroughly explored both theoretically and experimentally.

In the coming years, we expect to see further development and more applications enabled by such technologies.

## 6.2 All-dielectric metasurfaces

All-dielectric surface nanophotonics structure has been increasingly explored recently due to the dramatically enhanced fabrication technology. We envision several future directions in which the field of all-dielectric metasurface can have a profound impact.

- **Enhanced Color Filters:**

A color filter embodies various colors by selecting a specific wavelength in the visible light region. Color filters are used widely as core elements for such diverse applications as CMOS image sensors, liquid-crystal display devices, and light-emitting diodes [177, 178]. Color filters are mainly fabricated by spreading a resin, including dye or pigment in three basic colors (RGB), and then patterning each color using photolithography. Pigment density must be increased to enhance the chromatic properties of the color filter; this can result in low transmittance and dramatically increase display power consumption (now 70% of light in LCD is absorbed by the color filters). In addition, manufacturing a color filter by photolithography may consist of approximately 20 steps, including the black matrix process, and must be repeated three times to construct the RGB patterns. Thus, this process represents a large cost and a significant

environmental burden. With the methods discussed in Chapter 3 and 4, it might be possible to fabricate all-dielectric nanophotonics based color filters in a few photolithography steps. Furthermore, the structural color based filters will almost absorb no light, and reflect the unwanted colors to be recycled to somewhere else.

- **Thermal photonics:**

An emerging theme in nanophotonics research is the control of heat radiation for coherent thermal sources, thermophotovoltaics and high-temperature plasmonic coatings. Especially in the mid-infrared range, spectrally tailored thermal sources can lead to biosensing applications. All-dielectric Fano resonant metasurfaces could be an approach to imprint polarization sensitivity and spectral selectivity to thermal emission, which is otherwise incoherent and unpolarized.

- **Silicon-on-insulator platforms:**

One significant advantage of all-dielectric metasurface is the possibility to fabricate them on-chip in a traditional, complementary metal-oxide semiconductor (CMOS)-compatible silicon photonics platform to interface with existing photonic devices. This makes large-area and low-cost realization of the nanophotonics designs possible.

## 6.3 On-Chip Optical Neuromorphic Computing

Computer chips that use light to move data and operating data would be much more energy efficient and possibly even faster than today's chips, which use electricity. Researches in optical computing has been carried out by various groups and has drawn increasing attentions recently due to the enhancement of fabrication technology and the slowing down of Moore's law.

Up to now, most of the groups working on optical computing are aiming at realizing general purpose computing with optics. In this thesis we proposed a specialized optical computing system that is designed for performing deep learning algorithm.

As the applications of artificial intelligence keep increasing, as well as the size and quantity of data, larger portion of computational resources in cluster or personal devices will be spent on doing deep learning calculation. In this case, there will be an increasing demand on specially purposed computing chips.

Future developing opportunities includes:

- Generalizing the on-chip optical neuromorphic computing architecture to other deep learning algorithm, such as Convolution Neuron Network (for image recognition) and Recurrent Neuron Network (for language processing), and other neuron network systems.
- Since the neuromorphic computing mechanism proposed in Chapter 5 is extremely fast and efficient at forward propagation, it potentially can be trained without doing backward propagation, hence suitable for some neuron network architectures that is notoriously hard to train, such as Recurrent Neuron Network.
- Current neuromorphic computing architecture is designed such that it exactly mimic the current neuron network system. However, it might be possible to design new neuron network systems that is specifically designed for optics, such as using complex field and unitary matrix.



# Bibliography

- [1] V. Liu and S. Fan, “S<sup>4</sup> : A free electromagnetic solver for layered periodic structures,” *Computer Physics Communications*, vol. 183, no. 10, pp. 2233 – 2244, 2012. [Online]. Available: <http://www.sciencedirect.com/science/article/pii/S0010465512001658>
- [2] Y. Shen, D. Ye, I. Celanovic, S. G. Johnson, J. D. Joannopoulos, and M. Soljačić, “Optical broadband angular selectivity,” *Science*, vol. 343, no. 6178, pp. 1499–1501, 2014. [Online]. Available: <http://www.sciencemag.org/content/343/6178/1499.abstract>
- [3] T. Xu, Y.-K. Wu, X. Luo, and L. J. Guo, “Plasmonic nanoresonators for high-resolution colour filtering and spectral imaging,” *Nature communications*, vol. 1, p. 59, 2010.
- [4] Q. Chen and D. R. Cumming, “High transmission and low color cross-talk plasmonic color filters using triangular-lattice hole arrays in aluminum films,” *Optics express*, vol. 18, no. 13, pp. 14 056–14 062, 2010.
- [5] G. Si, Y. Zhao, J. Lv, M. Lu, F. Wang, H. Liu, N. Xiang, T. J. Huang, A. J. Danner, and J. Teng, “Reflective plasmonic color filters based on lithographically patterned silver nanorod arrays,” *Nanoscale*, vol. 5, no. 14, pp. 6243–6248, 2013.
- [6] Y. Shen, V. Rinnerbauer, I. Wang, V. Stelmakh, J. D. Joannopoulos, and M. Soljačić, “Structural colors from fano resonances,” *ACS Photonics*, vol. 2, no. 1, pp. 27–32, 2015.

- [7] E. Yablonovitch, “Inhibited spontaneous emission in solid-state physics and electronics,” *Phys. Rev. Lett.*, vol. 58, pp. 2059–2062, May 1987. [Online]. Available: <http://link.aps.org/doi/10.1103/PhysRevLett.58.2059>
- [8] —, “Photonic band-gap structures,” *J. Opt. Soc. Am. B*, vol. 10, no. 2, pp. 283–295, Feb 1993. [Online]. Available: <http://josab.osa.org/abstract.cfm?URI=josab-10-2-283>
- [9] J. Joannopoulos, S. Johnson, J. Winn, and R. Meade, *Photonic Crystals: Molding the Flow of Light (Second Edition)*. Princeton University Press, 2011. [Online]. Available: <http://books.google.com/books?id=owhE36qiTP8C>
- [10] S. G. Johnson and J. D. Joannopoulos, “Three-dimensionally periodic dielectric layered structure with omnidirectional photonic band gap,” *Applied Physics Letters*, vol. 77, no. 22, pp. 3490–3492, 2000. [Online]. Available: <http://scitation.aip.org/content/aip/journal/apl/77/22/10.1063/1.1328369>
- [11] Y. Fink, J. N. Winn, S. Fan, C. Chen, J. Michel, J. D. Joannopoulos, and E. L. Thomas, “A dielectric omnidirectional reflector,” *Science*, vol. 282, no. 5394, pp. 1679–1682, 1998.
- [12] S. Sriram, K. Steinbruegge, and E. Supertzi, uS patent 4512638 filed 31 Aug 1982, and issued 23 Apr 1985.
- [13] J. F. Archard and A. M. Taylor, “Improved glan-foucault prism,” *J. Sci. Instrum.*, vol. 25, no. 12, p. 407, 1948. [Online]. Available: <http://stacks.iop.org/0950-7671/25/i=12/a=304>
- [14] E. Hecht, *Optics*. Pearson Education, 2008. [Online]. Available: <http://books.google.com/books?id=wcMWpBMMzIkC>
- [15] Figure from <http://www.yxingoptics.com/products-detail.asp?cpid=106>.
- [16] Figure from <http://www.ealingcatalog.com/optics/mirrors-beamsplitters/broadband-dielectric-mirrors.html>.

- [17] M. F. Weber, C. A. Stover, L. R. Gilbert, T. J. Nevitt, and A. J. Ouderkirk, "Giant birefringent optics in multilayer polymer mirrors," *Science*, vol. 287, no. 5462, pp. 2451–2456, 2000. [Online]. Available: <http://www.sciencemag.org/content/287/5462/2451.abstract>
- [18] Figure from <http://astronomy-guide.blogspot.com>.
- [19] Photo from La instalaci3n m3s grande para comunicaci3n satelital en Raisting, Baviera, Alemania.
- [20] J. Upping, P. Miclea, R. Wehrspohn, T. Baumgarten, and S. Greulich-Weber, "Direction-selective optical transmission of 3d fcc photonic crystals in the microwave regime," *Photonics and Nanostructures - Fundamentals and Applications*, vol. 8, no. 2, pp. 102 – 106, 2010, special Issue {PECS} 8. [Online]. Available: <http://www.sciencedirect.com/science/article/pii/S1569441009000698>
- [21] B. T. Schwartz and R. Piestun, "Total external reflection from metamaterials with ultralow refractive index," *J. Opt. Soc. Am. B*, vol. 20, no. 12, pp. 2448–2453, Dec 2003. [Online]. Available: <http://josab.osa.org/abstract.cfm?URI=josab-20-12-2448>
- [22] F. G. De Abajo, "Colloquium: Light scattering by particle and hole arrays," *Reviews of Modern Physics*, vol. 79, no. 4, p. 1267, 2007.
- [23] K. Q. Le, C. Argyropoulos, N. Mattiucci, G. D'Aguanno, M. J. Bloemer, and A. Alù, "Broadband brewster transmission through 2d metallic gratings," *Journal of Applied Physics*, vol. 112, no. 9, p. 094317, 2012.
- [24] A. Alù, G. D'Aguanno, N. Mattiucci, and M. J. Bloemer, "Plasmonic brewster angle: Broadband extraordinary transmission through optical gratings," *Phys. Rev. Lett.*, vol. 106, p. 123902, Mar 2011. [Online]. Available: <http://link.aps.org/doi/10.1103/PhysRevLett.106.123902>
- [25] Y. Shen, D. Ye, L. Wang, I. Celanovic, L. Ran, J. D. Joannopoulos, and M. Soljačić, "Metamaterial broadband angular selectivity,"

- Phys. Rev. B*, vol. 90, p. 125422, Sep 2014. [Online]. Available: <http://link.aps.org/doi/10.1103/PhysRevB.90.125422>
- [26] N. Aközbeek, N. Mattiucci, D. de Ceglia, R. Trimm, A. Alù, G. D'Alagnano, M. Vincenti, M. Scalora, and M. Bloemer, “Experimental demonstration of plasmonic brewster angle extraordinary transmission through extreme subwavelength slit arrays in the microwave,” *Physical Review B*, vol. 85, no. 20, p. 205430, 2012.
- [27] C. Argyropoulos, K. Q. Le, N. Mattiucci, G. D'Alagnano, and A. Alu, “Broadband absorbers and selective emitters based on plasmonic brewster metasurfaces,” *Physical Review B*, vol. 87, no. 20, p. 205112, 2013.
- [28] C. Argyropoulos, G. D'Alagnano, N. Mattiucci, N. Akozbek, M. J. Bloemer, and A. Alu, “Matching and funneling light at the plasmonic brewster angle,” *Physical Review B*, vol. 85, no. 2, p. 024304, 2012.
- [29] G. M. C. *et al*, uS patent 7467873B2 filed 14 Oct 2005, and issued 23 Dec 2008.
- [30] F. Rouser, uS patent 5204160A filed 28 May 1991, and issued 20 Apr 1993.
- [31] R. Cohen, uS patent 4553818A filed 12 Dec 1983, and issued 19 Nov 1985.
- [32] E. D. Kosten, J. H. Atwater, J. Parsons, A. Polman, and H. A. Atwater, “Highly efficient gaas solar cells by limiting light emission angle,” *Light Sci Appl*, vol. 2, p. e45, Jan 2013. [Online]. Available: <http://www.nature.com/lisa/journal/v2/n1/supinfo/lisa20131s1.html>
- [33] J. H. Atwater, P. Spinelli, E. Kosten, J. Parsons, C. Van Lare, J. Van de Groep, J. G. De Abajo, A. Polman, and H. A. Atwater, “Microphotonic parabolic light directors fabricated by two-photon lithography,” *Applied Physics Letters*, vol. 99, no. 15, p. 151113, 2011.
- [34] B. K. Winker and D. B. Taber, uS patent 6239853 filed 1 Oct 1999, and issued 29 May 2001.

- [35] S. W. MacMaster, uS patent 7052746 filed 26 Nov 2003, and issued 30 May 2006.
- [36] M. Rundquist, “Broadband angular selectivity achieved with a birefringent filter,” Ph.D. dissertation, University of Minnesota, 2002.
- [37] T. W. Ebbesen, H. Lezec, H. Ghaemi, T. Thio, and P. Wolff, “Extraordinary optical transmission through sub-wavelength hole arrays,” *Nature*, vol. 391, no. 6668, pp. 667–669, 1998.
- [38] F. J. Garcia-Vidal, L. Martin-Moreno, T. Ebbesen, and L. Kuipers, “Light passing through subwavelength apertures,” *Reviews of Modern Physics*, vol. 82, no. 1, p. 729, 2010.
- [39] F. Medina, F. Mesa, and R. Marqués, “Extraordinary transmission through arrays of electrically small holes from a circuit theory perspective,” *Microwave Theory and Techniques, IEEE Transactions on*, vol. 56, no. 12, pp. 3108–3120, 2008.
- [40] A. Alù and N. Engheta, “Optical nanotransmission lines: synthesis of planar left-handed metamaterials in the infrared and visible regimes,” *JOSA B*, vol. 23, no. 3, pp. 571–583, 2006.
- [41] B. Perilloux, *Thin-film Design: Modulated Thickness and Other Stopband Design Methods*, ser. Tutorial texts in optical engineering. SPIE Press, 2002. [Online]. Available: <http://books.google.com/books?id=sHpPeD-788MC>
- [42] C. Zhang, F. Qiao, J. Wan, and J. Zi, “Enlargement of nontransmission frequency range in photonic crystals by using multiple heterostructures,” *J. Appl. Phys.*, vol. 87, no. 6, pp. 3174–3176, 2000. [Online]. Available: <http://scitation.aip.org/content/aip/journal/jap/87/6/10.1063/1.372318>
- [43] X. Wang, X. Hu, Y. Li, W. Jia, C. Xu, X. Liu, and J. Zi, “Enlargement of omnidirectional total reflection frequency range in one-dimensional photonic

- crystals by using photonic heterostructures,” *Appl. Phys. Lett.*, vol. 80, no. 23, pp. 4291–4293, 2002.
- [44] V. V. Zhurin, H. Kaufman, J. R. Kahn, and T. L. Hylton, “Biased target deposition,” *J. Vac. Sci. Technol., A*, vol. 18, no. 1, pp. 37–41, 2000.
- [45] D. W. Schaefer and K. D. Keefer, “Structure of random porous materials: Silica aerogel,” *Phys. Rev. Lett.*, vol. 56, pp. 2199–2202, May 1986. [Online]. Available: <http://link.aps.org/doi/10.1103/PhysRevLett.56.2199>
- [46] Supporting Materials available on *Optics Express* online.
- [47] M. A. Aegerter, N. Leventis, and M. M. Koebel, *Aerogels handbook*. Springer Science & Business Media, 2011.
- [48] Y. Shen, C.-W. Hsu, M. Soljačić, and J. D. Joannopoulos, arXiv:1502.00243.
- [49] J. B. Pendry, A. J. Holden, D. J. Robbins, and W. J. Stewart, “Magnetism from conductors and enhanced nonlinear phenomena,” *IEEE Transactions on Microwave Theory Techniques*, vol. 47, pp. 2075–2084, Nov. 1999.
- [50] J. B. Pendry, A. J. Holden, W. J. Stewart, and I. Youngs, “Extremely low frequency plasmons in metallic mesostructures,” *Phys. Rev. Lett.*, vol. 76, pp. 4773–4776, Jun 1996. [Online]. Available: <http://link.aps.org/doi/10.1103/PhysRevLett.76.4773>
- [51] J. Shin, J.-T. Shen, and S. Fan, “Three-dimensional metamaterials with an ultrahigh effective refractive index over a broad bandwidth,” *Phys. Rev. Lett.*, vol. 102, p. 093903, Mar 2009. [Online]. Available: <http://link.aps.org/doi/10.1103/PhysRevLett.102.093903>
- [52] R. E. Hamam, I. Celanovic, and M. Soljačić, “Angular photonic band gap,” *Phys. Rev. A*, vol. 83, p. 035806, Mar 2011. [Online]. Available: <http://link.aps.org/doi/10.1103/PhysRevA.83.035806>

- [53] R. Azzam and N. Bashara, *Ellipsometry and polarized light*, ser. North-Holland personal library. North-Holland Pub. Co., 1977. [Online]. Available: [http://books.google.com/books?id=1\\_4uAQAAIAAJ](http://books.google.com/books?id=1_4uAQAAIAAJ)
- [54] A. Cho and J. Arthur, "Molecular beam epitaxy," *Progress in solid state chemistry*, vol. 10, pp. 157–191, 1975.
- [55] D. J. Bergman, "The dielectric constant of a composite material—A problem in classical physics," *Physics Reports*, vol. 43, no. 9, pp. 377 – 407, 1978. [Online]. Available: <http://www.sciencedirect.com/science/article/pii/0370157378900091>
- [56] A. Einstein and T. into English, "Concerning an heuristic point of view toward the emission and transformation of light," *American Journal of Physics*, vol. 33, no. 5, p. 367, 1965.
- [57] B. Norton, *Harnessing Solar Heat (First Edition)*. Springer, 2013. [Online]. Available: <http://www.ebooks.com/1538833/harnessing-solar-heat/norton-brian/>
- [58] Y. X. Yeng, M. Ghebrebrhan, P. Bermel, W. R. Chan, J. D. Joannopoulos, M. Soljačić, and I. Celanovic, "Enabling high-temperature nanophotonics for energy applications," *Proceedings of the National Academy of Sciences*, 2012. [Online]. Available: <http://www.pnas.org/content/early/2012/01/20/1120149109.abstract>
- [59] A. Lenert, D. M. Blerman, Y. Nam, W. R. Chan, I. Celanovic, M. Soljačić, and W. E. N., "A nanophotonic solar thermophotovoltaic device," *Nature Nanotechnology*, 2014. [Online]. Available: <http://www.nature.com/nnano/journal/v9/n2/full/nnano.2013.286.html>
- [60] V. Rinnerbauer, Y. Shen, J. D. Joannopoulos, M. Soljačić, F. Schaffler, and I. Celanovic, "Superlattice photonic crystal as broadband solar absorber for high temperature operation," *Optics express*, vol. 22, no. S7, p. A1895, 2014.

- [61] F. J. DiSalvo, "Thermoelectric cooling and power generation," *Science*, vol. 285, no. 5428, pp. 703–706, 1999.
- [62] R. Venkatasubramanian, E. Siivola, T. Colpitts, and B. O'quinn, "Thin-film thermoelectric devices with high room-temperature figures of merit," *Nature*, vol. 413, no. 6856, pp. 597–602, 2001.
- [63] W. Shockley and H. J. Queisser, "Detailed balance limit of efficiency of p-n junction solar cells," *Journal of applied physics*, vol. 32, no. 3, pp. 510–519, 1961.
- [64] T. Markvart, "Solar cell as a heat engine: energy–entropy analysis of photovoltaic conversion," *physica status solidi (a)*, vol. 205, no. 12, pp. 2752–2756, 2008. [Online]. Available: <http://dx.doi.org/10.1002/pssa.200880460>
- [65] M. Peters, J. C. Goldschmidt, and B. Bläsi, "Angular confinement and concentration in photovoltaic converters," *Solar energy materials and solar cells*, vol. 94, no. 8, pp. 1393–1398, 2010.
- [66] L. Fraas and L. Partain, *Solar Cells and Their Applications*, ser. Wiley Series in Microwave and Optical Engineering. Wiley, 2010. [Online]. Available: <http://books.google.com/books?id=K6aSCEmQZEMC>
- [67] L. Weinstein, D. Kraemer, K. McEnaney, and G. Chen, "Optical cavity for improved performance of solar receivers in solar-thermal systems," *Solar Energy*, vol. 108, pp. 69–79, 2014.
- [68] A. Bett, C. Baur, F. Dimroth, G. Lange, M. Meusel, S. Van Riesen, G. Siefer, V. Andreev, V. Romyantsev, and N. Sadchikov, "Flatcon/spl trade/-modules: technology and characterisation," in *Photovoltaic Energy Conversion, 2003. Proceedings of 3rd World Conference on*, vol. 1. IEEE, 2003, pp. 634–637.
- [69] E. D. Kosten and H. A. Atwater, "Limiting acceptance angle to maximize efficiency in solar cells," in *Society of Photo-Optical Instrumentation Engineers*

(*SPIE*) Conference Series, ser. Society of Photo-Optical Instrumentation Engineers (SPIE) Conference Series, vol. 8124, Sep. 2011.

- [70] V. Badescu, "Spectrally and angularly selective photothermal and photovoltaic converters under one-sun illumination," *Journal of Physics D: Applied Physics*, vol. 38, no. 13, p. 2166, 2005. [Online]. Available: <http://stacks.iop.org/0022-3727/38/i=13/a=014>
- [71] E. D. Kosten, "Optical designs for improved solar cell performance," Ph.D. dissertation, California Institute of Technology, 2014.
- [72] M. Agrawal, "Photonic design for efficient solid state energy conversion," Ph.D. dissertation, Stanford University, 2009.
- [73] E. Yablonovitch, "Statistical ray optics," *J. Opt. Soc. Am.*, vol. 72, no. 7, pp. 899–907, Jul 1982. [Online]. Available: <http://www.opticsinfobase.org/abstract.cfm?URI=josa-72-7-899>
- [74] O. Hohn, M. Peters, C. Ulbrich, A. Hoffmann, U. T. Schwarz, and B. Bláđsi, "Optimization of angularly selective photonic filters for concentrator photovoltaic," *Proc. SPIE*, vol. 8438, pp. 84 380A–84 380A–10, 2012. [Online]. Available: <http://dx.doi.org/10.1117/12.921773>
- [75] P. Campbell and M. A. Green, "The limiting efficiency of silicon solar cells under concentrated sunlight," *Electron Devices, IEEE Transactions on*, vol. 33, no. 2, pp. 234–239, 1986.
- [76] E. D. Kosten, B. M. Kayes, and H. A. Atwater, "Experimental demonstration of enhanced photon recycling in angle-restricted gaas solar cells," *Energy & Environmental Science*, vol. 7, no. 6, pp. 1907–1912, 2014.
- [77] W. P. Dumke, "Spontaneous radiative recombination in semiconductors," *Phys. Rev.*, vol. 105, pp. 139–144, Jan 1957. [Online]. Available: <http://link.aps.org/doi/10.1103/PhysRev.105.139>

- [78] O. Höhn, M. Peters, C. Ulbrich, A. Hoffmann, U. Schwarz, and B. Bläsi, “Optimization of angularly selective photonic filters for concentrator photovoltaic,” in *SPIE Photonics Europe*. International Society for Optics and Photonics, 2012, pp. 84 380A–84 380A.
- [79] O. Höhn, T. Kraus, G. Bauhuis, U. T. Schwarz, and B. Bläsi, “Maximal power output by solar cells with angular confinement,” *Optics Express*, vol. 22, no. 103, pp. A715–A722, 2014.
- [80] O. D. Miller, E. Yablonovitch, and S. R. Kurtz, “Strong internal and external luminescence as solar cells approach the shockley–queisser limit,” *Photovoltaics, IEEE Journal of*, vol. 2, no. 3, pp. 303–311, 2012.
- [81] A. Martí, J. Balenzategui, and R. Reyna, “Photon recycling and shockley–queisser diode equation,” *Journal of applied physics*, vol. 82, no. 8, pp. 4067–4075, 1997.
- [82] G. L. Araújo and A. Martí, “Absolute limiting efficiencies for photovoltaic energy conversion,” *Solar Energy Materials and Solar Cells*, vol. 33, no. 2, pp. 213–240, 1994.
- [83] J. Müller, B. Rech, J. Springer, and M. Vanecek, “Tco and light trapping in silicon thin film solar cells,” *Solar Energy*, vol. 77, no. 6, pp. 917–930, 2004.
- [84] T. Tiedje, E. Yablonovitch, G. D. Cody, and B. G. Brooks, “Limiting efficiency of silicon solar cells,” *Electron Devices, IEEE Transactions on*, vol. 31, no. 5, pp. 711–716, 1984.
- [85] E. Kosten, B. Newman, J. Lloyd, A. Polman, and H. Atwater, “Limiting light escape angle in silicon photovoltaics: Ideal and realistic cells,” *Photovoltaics, IEEE Journal of*, vol. 5, no. 1, pp. 61–69, Jan 2015.
- [86] A. Arbabi, Y. Horie, M. Bagheri, and A. Faraon, “Dielectric metasurfaces for complete control of phase and polarization with subwavelength spatial resolution and high transmission,” *Nature nanotechnology*, 2015.

- [87] B. Shen, P. Wang, R. Polson, and R. Menon, “Ultra-high-efficiency metamaterial polarizer,” *Optica*, vol. 1, no. 5, pp. 356–360, 2014.
- [88] V. Rinnerbauer, A. Lenert, D. M. Bierman, Y. X. Yeng, W. R. Chan, R. D. Geil, J. J. Senkevich, J. D. Joannopoulos, E. N. Wang, M. Soljačić *et al.*, “Metallic photonic crystal absorber-emitter for efficient spectral control in high-temperature solar thermophotovoltaics,” *Advanced Energy Materials*, 2014.
- [89] Y. X. Yeng, J. B. Chou, V. Rinnerbauer, Y. Shen, S.-G. Kim, J. D. Joannopoulos, M. Soljačić, and I. Čelanović, “Global optimization of omnidirectional wavelength selective emitters/absorbers based on dielectric-filled anti-reflection coated two-dimensional metallic photonic crystals,” *Optics Express*, vol. 22, no. 18, pp. 21 711–21 718, 2014.
- [90] P. Bermel, M. Ghebrebrhan, W. Chan, Y. X. Yeng, M. Araghchini, R. Hamam, C. H. Marton, K. F. Jensen, M. Soljačić, J. D. Joannopoulos, S. G. Johnson, and I. Celanovic, “Design and global optimization of high-efficiency thermophotovoltaic systems,” *Opt. Express*, vol. 18, no. S3, pp. A314–A334, Sep 2010. [Online]. Available: <http://www.opticsexpress.org/abstract.cfm?URI=oe-18-103-A314>
- [91] P. Bermel, M. Ghebrebrhan, M. Harradon, Y. Yeng, I. Celanovic, J. D. Joannopoulos, and M. Soljačić, “Tailoring photonic metamaterial resonances for thermal radiation,” *Nanoscale research letters*, vol. 6, no. 1, pp. 1–5, 2011.
- [92] M. J. Blanco, J. G. Martín, and D. C. Alarcón-Padilla, “Theoretical efficiencies of angular-selective non-concentrating solar thermal systems,” *Solar Energy*, vol. 76, no. 6, pp. 683–691, 2004.
- [93] R. N. Wilson and R. N. Wilson, *Reflecting telescope optics*. Springer Verlag, 1999.
- [94] S. Ananthkrishnan, “The giant meterwave radio telescope,” *Journal of Astrophysics and Astronomy*, vol. 16, no. Sup, pp. 427–435, 1995.

- [95] P. A. R. Ade, R. W. Aikin, M. Amiri, D. Barkats, S. J. Benton, C. A. Bischoff, J. J. Bock, J. A. Brevik, I. Buder, E. Bullock, G. Davis, P. K. Day, C. D. Dowell, L. Duband, J. P. Filippini, S. Fliescher, S. R. Golwala, M. Halpern, M. Hasselfield, S. R. Hildebrandt, G. C. Hilton, K. D. Irwin, K. S. Karkare, J. P. Kaufman, B. G. Keating, S. A. Kernasovskiy, J. M. Kovac, C. L. Kuo, E. M. Leitch, N. Llombart, M. Lueker, C. B. Netterfield, H. T. Nguyen, R. O'Brient, I. R. W. Ogburn, A. Orlando, C. Pryke, C. D. Reintsema, S. Richter, R. Schwarz, C. D. Sheehy, Z. K. Staniszewski, K. T. Story, R. V. Sudiwala, G. P. Teply, J. E. Tolan, A. D. Turner, A. G. Vieregg, P. Wilson, C. L. Wong, K. W. Yoon, and B. Collaboration, "Bicep2. ii. experiment and three-year data set," *The Astrophysical Journal*, vol. 792, no. 1, p. 62, 2014. [Online]. Available: <http://stacks.iop.org/0004-637X/792/i=1/a=62>
- [96] B. Temelkuran, M. Bayindir, E. Ozbay, R. Biswas, M. Sigalas, G. Tuttle, and K.-M. Ho, "Photonic crystal-based resonant antenna with a very high directivity," *Journal of applied physics*, vol. 87, no. 1, pp. 603–605, 2000.
- [97] S. Kinoshita, S. Yoshioka, and J. Miyazaki, "Physics of structural colors," *Rep. Prog. Phys.*, vol. 71, no. 7, p. 076401, 2008.
- [98] D. Graham-Rowe, "Tunable structural colour," *Nat. Photonics*, vol. 3, no. 10, pp. 551–553, 2009.
- [99] H. Kim, J. Ge, J. Kim, S.-e. Choi, H. Lee, H. Lee, W. Park, Y. Yin, and S. Kwon, "Structural colour printing using a magnetically tunable and lithographically fixable photonic crystal," *Nat. Photonics*, vol. 3, no. 9, pp. 534–540, 2009.
- [100] A. C. Arsenault, D. P. Puzzo, I. Manners, and G. A. Ozin, "Photonic-crystal full-colour displays," *Nat. Photonics*, vol. 1, no. 8, pp. 468–472, 2007.
- [101] R. O. Prum, R. H. Torres, S. Williamson, and J. Dyck, "Coherent light scattering by blue feather barbs," *Nature*, vol. 396, no. 6706, pp. 28–29, 1998.

- [102] J. D. Forster, H. Noh, S. F. Liew, V. Saranathan, C. F. Schreck, L. Yang, J.-G. Park, R. O. Prum, S. G. Mochrie, C. S. O'Hern, and Others, "Biomimetic isotropic nanostructures for structural coloration," *Adv. Mater.*, vol. 22, no. 26-27, pp. 2939–2944, 2010.
- [103] H. Noh, S. F. Liew, V. Saranathan, S. G. Mochrie, R. O. Prum, E. R. Dufresne, and H. Cao, "How noniridescent colors are generated by quasi-ordered structures of bird feathers," *Adv. Mater.*, vol. 22, no. 26-27, pp. 2871–2880, 2010.
- [104] M. Kolle, B. Zheng, N. Gibbons, J. J. Baumberg, and U. Steiner, "Stretch-tuneable dielectric mirrors and optical microcavities," *Opt. Express*, vol. 18, no. 5, pp. 4356–4364, 2010.
- [105] M. Kolle, P. M. Salgard-Cunha, M. R. Scherer, F. Haung, P. Vukusic, S. Mahajan, J. J. Baumberg, and U. Steiner, "Mimicking the colourful wing scale structure of the papilio blumei butterfly," *Nat. Nanotechnol.*, vol. 5, no. 7, pp. 511–515, 2010.
- [106] M. Kolle, A. Lethbridge, M. Kreysing, J. J. Baumberg, J. Aizenberg, and P. Vukusic, "Bio-inspired band-gap tunable elastic optical multilayer fibers," *Adv. Mater.*, vol. 25, no. 15, pp. 2239–2245, 2013.
- [107] B. Michaelis, D. R. Snoswell, N. A. Bell, P. Spahn, G. P. Hellmann, C. E. Finlayson, and J. J. Baumberg, "Generating lithographically-defined tunable printed structural color," *Adv. Eng. Mater.*, vol. 15, no. 10, pp. 948–953, 2013.
- [108] M. Aschwanden and A. Stemmer, "Polymeric, electrically tunable diffraction grating based on artificial muscles," *Opt. Lett.*, vol. 31, no. 17, pp. 2610–2612, 2006.
- [109] H. A. Macleod, *Thin-film optical filters*. CRC Press, 2001.
- [110] P. Yeh, *Optical Waves in Layered Media*, ser. Wiley Series in Pure and Applied Optics. Wiley, 2005. [Online]. Available: <http://books.google.com/books?id=yZBAQAAIAAJ>

- [111] M. A. Kats, R. Blanchard, P. Genevet, and F. Capasso, “Nanometre optical coatings based on strong interference effects in highly absorbing media,” *Nat. Mater.*, vol. 12, no. 1, pp. 20–24, 2013.
- [112] S. J. Tan, L. Zhang, D. Zhu, X. M. Goh, Y. M. Wang, K. Kumar, C.-W. Qiu, and J. K. Yang, “Plasmonic color palettes for photorealistic printing with aluminum nanostructures,” *Nano letters*, vol. 14, no. 7, pp. 4023–4029, 2014.
- [113] J. Olson, A. Manjavacas, L. Liu, W.-S. Chang, B. Foerster, N. S. King, M. W. Knight, P. Nordlander, N. J. Halas, and S. Link, “Vivid, full-color aluminum plasmonic pixels,” *Proceedings of the National Academy of Sciences*, vol. 111, no. 40, pp. 14 348–14 353, 2014.
- [114] K. Kumar, H. Duan, R. S. Hegde, S. C. Koh, J. N. Wei, and J. K. Yang, “Printing colour at the optical diffraction limit,” *Nature nanotechnology*, vol. 7, no. 9, pp. 557–561, 2012.
- [115] Y. J. Liu, G. Y. Si, E. S. P. Leong, N. Xiang, A. J. Danner, and J. H. Teng, “Light-driven plasmonic color filters by overlaying photoresponsive liquid crystals on gold annular aperture arrays,” *Advanced Materials*, vol. 24, no. 23, pp. OP131–OP135, 2012. [Online]. Available: <http://dx.doi.org/10.1002/adma.201104440>
- [116] S. Yokogawa, S. P. Burgos, and H. A. Atwater, “Plasmonic color filters for cmos image sensor applications,” *Nano letters*, vol. 12, no. 8, pp. 4349–4354, 2012.
- [117] A. E. Miroshnichenko, S. Flach, and Y. S. Kivshar, “Fano resonances in nanoscale structures,” *Rev. Mod. Phys.*, vol. 82, no. 3, p. 2257, 2010.
- [118] S. Fan and J. Joannopoulos, “Analysis of guided resonances in photonic crystal slabs,” *Phys. Rev. B*, vol. 65, no. 23, p. 235112, 2002.
- [119] S. Fan, W. Suh, and J. Joannopoulos, “Temporal coupled-mode theory for the fano resonance in optical resonators,” *JOSA A*, vol. 20, no. 3, pp. 569–572, 2003.

- [120] K. S. Kunz and R. J. Luebbers, *The finite difference time domain method for electromagnetics*. CRC press, 1993.
- [121] V. A. Mandelshtam and H. S. Taylor, “Harmonic inversion of time signals and its applications,” *J. Chem. Phys.*, vol. 107, no. 17, pp. 6756–6769, 1997.
- [122] M. Schattenburg, R. Aucoin, and R. Fleming, “Optically matched trilevel resist process for nanostructure fabrication,” *J. Vac. Sci. Technol. B*, vol. 13, no. 6, pp. 3007–3011, 1995.
- [123] T. Savas, M. Schattenburg, J. Carter, and H. I. Smith, “Large-area achromatic interferometric lithography for 100 nm period gratings and grids,” *J. Vac. Sci. Technol. B*, vol. 14, no. 6, pp. 4167–4170, 1996.
- [124] M. E. Walsh, “On the design of lithographic interferometers and their application,” Ph.D. dissertation, Massachusetts Institute of Technology, 2004.
- [125] E. H. Anderson, “Fabrication and electromagnetic applications of periodic nanostructures,” Ph.D. dissertation, Massachusetts Institute of Technology, 1988.
- [126] M. Schattenburg, E. Anderson, and H. I. Smith, “X-ray/vuv transmission gratings for astrophysical and laboratory applications,” *Phys. Scr.*, vol. 41, no. 1, p. 13, 1990.
- [127] G. Kamita, M. Kolle, F. Huang, J. J. Baumberg, and U. Steiner, “Multi-layer mirrored bubbles with spatially-chirped and elastically-tuneable optical bandgaps,” *Optics express*, vol. 20, no. 6, pp. 6421–6428, 2012.
- [128] K. Sakoda, *Optical Properties of Photonic Crystals*. Springer-Verlag Berlin Heidelberg, 2005.
- [129] P. Russell, “Photonic crystal fibers,” *Science*, vol. 299, no. 5605, pp. 358–362, 2003. [Online]. Available: <http://www.sciencemag.org/content/299/5605/358.abstract>

- [130] J. C. Knight, J. Broeng, T. A. Birks, and P. S. J. Russell, “Photonic band gap guidance in optical fibers,” *Science*, vol. 282, no. 5393, pp. 1476–1478, 1998. [Online]. Available: <http://www.sciencemag.org/content/282/5393/1476.abstract>
- [131] M. L. Brongersma, Y. Cui, and S. Fan, “Light management for photovoltaics using high-index nanostructures,” *Nat. Mater.*, vol. 13, no. 5, pp. 451–460, 05 2014. [Online]. Available: <http://dx.doi.org/10.1038/nmat3921>
- [132] S. Fan and J. D. Joannopoulos, “Analysis of guided resonances in photonic crystal slabs,” *Phys. Rev. B*, vol. 65, p. 235112, Jun 2002. [Online]. Available: <http://link.aps.org/doi/10.1103/PhysRevB.65.235112>
- [133] C. W. Hsu, B. Zhen, J. Lee, S.-L. Chua, S. G. Johnson, J. D. Joannopoulos, and M. Soljačić, “Observation of trapped light within the radiation continuum,” *Nature*, vol. 499, pp. 188–191, 2013. [Online]. Available: <http://dx.doi.org/10.1038/nature12289>
- [134] K. Hirose, Y. Liang, Y. Kurosaka, A. Watanabe, T. Sugiyama, and S. Noda, “Watt-class high-power, high-beam-quality photonic-crystal lasers,” *Nat. Photon.*, vol. 8, no. 5, pp. 406–411, 05 2014. [Online]. Available: <http://dx.doi.org/10.1038/nphoton.2014.75>
- [135] A. A. Erchak, D. J. Ripin, S. Fan, P. Rakich, J. D. Joannopoulos, E. P. Ippen, G. S. Petrich, and L. A. Kolodziejski, “Enhanced coupling to vertical radiation using a two-dimensional photonic crystal in a semiconductor light-emitting diode,” *Appl. Phys. Lett.*, vol. 78, no. 5, pp. 563–565, 2001. [Online]. Available: <http://scitation.aip.org/content/aip/journal/apl/78/5/10.1063/1.1342048>
- [136] M. López-García, J. F. Galisteo-López, C. López, and A. García-Martín, “Light confinement by two-dimensional arrays of dielectric spheres,” *Phys. Rev. B*, vol. 85, p. 235145, Jun 2012. [Online]. Available: <http://link.aps.org/doi/10.1103/PhysRevB.85.235145>

- [137] “When the dielectric constant of the substrate is larger than the slab, the substrate will reflect some light because of the index contrast between the slab and the substrate. at the same time, there are more allowed diffraction channels into the substrate due to the high index. the combination of these effects determines the mode leakage and thus  $q$ . in general, the system can support a resonance mode, but  $q$  will be low and the wavelength will be shifted significantly. further, the resonance wavelength is shifted from the no-substrate condition and therefore follows the trend shown in fig. 1(a).”
- [138] T. K. Gaylord, W. E. Baird, and M. G. Moharam, “Zero-reflectivity high spatial-frequency rectangular-groove dielectric surface-relief gratings,” *Appl. Opt.*, vol. 25, no. 24, pp. 4562–4567, Dec 1986. [Online]. Available: <http://ao.osa.org/abstract.cfm?URI=ao-25-24-4562>
- [139] A. F. Oskooi, D. Roundy, M. Ibanescu, P. Bermel, J. D. Joannopoulos, and S. G. Johnson, “MEEP: A flexible free-software package for electromagnetic simulations by the FDTD method,” *Comput. Phys. Commun.*, vol. 181, pp. 687–702, January 2010.
- [140] J. B. Khurgin, “How to deal with the loss in plasmonics and metamaterials,” *Nat. Nano.*, vol. 10, no. 1, pp. 2–6, 01 2015. [Online]. Available: <http://dx.doi.org/10.1038/nnano.2014.310>
- [141] Q. Xu, V. R. Almeida, R. R. Panepucci, and M. Lipson, “Experimental demonstration of guiding and confining light in nanometer-size low-refractive-index material,” *Opt. Lett.*, vol. 29, no. 14, pp. 1626–1628, Jul 2004. [Online]. Available: <http://ol.osa.org/abstract.cfm?URI=ol-29-14-1626>
- [142] A. F. Abouraddy, M. Bayindir, G. Benoit, S. D. Hart, K. Kuriki, N. Orf, O. Shapira, F. Sorin, B. Temelkuran, and Y. Fink, “Towards multimaterial multifunctional fibres that see, hear, sense and communicate,” *Nat. Mater.*, vol. 6, no. 5, pp. 336–347, May 2007. [Online]. Available: <http://dx.doi.org/10.1038/nmat1889>

- [143] N. M. Litchinitser, A. K. Abeeluck, C. Headley, and B. J. Eggleton, "Antiresonant reflecting photonic crystal optical waveguides," *Opt. Lett.*, vol. 27, no. 18, pp. 1592–1594, Sep 2002. [Online]. Available: <http://ol.osa.org/abstract.cfm?URI=ol-27-18-1592>
- [144] I. Goykhman, B. Desiatov, and U. Levy, "Ultrathin silicon nitride microring resonator for biophotonic applications at 970 nm wavelength," *Appl. Phys. Lett.*, vol. 97, no. 8, 2010. [Online]. Available: <http://scitation.aip.org/content/aip/journal/apl/97/8/10.1063/1.3483766>
- [145] P. Vukusic and J. R. Sambles, "Photonic structures in biology," *Nature*, vol. 424, no. 6950, pp. 852–855, 08 2003. [Online]. Available: <http://dx.doi.org/10.1038/nature01941>
- [146] Y. Tan, J. Gu, X. Zang, W. Xu, K. Shi, L. Xu, and D. Zhang, "Versatile fabrication of intact three-dimensional metallic butterfly wing scales with hierarchical sub-micrometer structures," *Angewandte Chemie International Edition*, vol. 50, no. 36, pp. 8307–8311, 2011. [Online]. Available: <http://dx.doi.org/10.1002/anie.201103505>
- [147] Y. Tan, J. Gu, L. Xu, X. Zang, D. Liu, W. Zhang, Q. Liu, S. Zhu, H. Su, C. Feng, G. Fan, and D. Zhang, "High-density hotspots engineered by naturally piled-up subwavelength structures in three-dimensional copper butterfly wing scales for surface-enhanced raman scattering detection," *Adv. Funct. Mater.*, vol. 22, no. 8, pp. 1578–1585, 2012. [Online]. Available: <http://dx.doi.org/10.1002/adfm.201102948>
- [148] M. Deubel, G. von Freymann, M. Wegener, S. Pereira, K. Busch, and C. M. Soukoulis, "Direct laser writing of three-dimensional photonic-crystal templates for telecommunications," *Nat. Mater.*, vol. 3, no. 7, pp. 444–447, 07 2004. [Online]. Available: <http://dx.doi.org/10.1038/nmat1155>
- [149] J. Yin, J. L. YagÄije, M. C. Boyce, and K. K. Gleason, "Biaxially mechanical tuning of 2-d reversible and irreversible surface topologies through simultaneous

and sequential wrinkling,” *ACS Applied Materials & Interfaces*, vol. 6, no. 4, pp. 2850–2857, 2014.

- [150] M. J. Burek, Y. Chu, M. S. Z. Liddy, P. Patel, J. Rochman, S. Meesala, W. Hong, Q. Quan, M. D. Lukin, and M. Lončar, “High quality-factor optical nanocavities in bulk single-crystal diamond,” *Nat. Commun.*, vol. 5, 12 2014. [Online]. Available: <http://dx.doi.org/10.1038/ncomms6718>
- [151] S. Hughes, L. Ramunno, J. F. Young, and J. E. Sipe, “Extrinsic optical scattering loss in photonic crystal waveguides: Role of fabrication disorder and photon group velocity,” *Phys. Rev. Lett.*, vol. 94, p. 033903, Jan 2005. [Online]. Available: <http://link.aps.org/doi/10.1103/PhysRevLett.94.033903>
- [152] E. Kuramochi, M. Notomi, S. Hughes, A. Shinya, T. Watanabe, and L. Ramunno, “Disorder-induced scattering loss of line-defect waveguides in photonic crystal slabs,” *Phys. Rev. B*, vol. 72, p. 161318, Oct 2005. [Online]. Available: <http://link.aps.org/doi/10.1103/PhysRevB.72.161318>
- [153] A. L. Washburn and R. C. Bailey, “Photonics-on-a-chip: recent advances in integrated waveguides as enabling detection elements for real-world, lab-on-a-chip biosensing applications,” *Analyst*, vol. 136, pp. 227–236, 2011. [Online]. Available: <http://dx.doi.org/10.1039/C0AN00449A>
- [154] A. Liu, L. Liao, Y. Chetrit, J. Basak, H. Nguyen, D. Rubin, and M. Paniccia, “Wavelength division multiplexing based photonic integrated circuits on silicon-on-insulator platform,” *Selected Topics in Quantum Electronics, IEEE Journal of*, vol. 16, no. 1, pp. 23–32, Jan 2010.
- [155] D. Liang and J. Bowers, “Photonic integration: Si or inp substrates?” *Electron. Lett.*, vol. 45, no. 12, pp. 578–581, June 2009.
- [156] X. Yu, L. Shi, D. Han, J. Zi, and P. V. Braun, “High quality factor metallodielectric hybrid plasmonic-photonic crystals,” *Adv. Funct.*

- Mater.*, vol. 20, no. 12, pp. 1910–1916, 2010. [Online]. Available: <http://dx.doi.org/10.1002/adfm.201000135>
- [157] A. A. Yanik, A. E. Cetin, M. Huang, A. Artar, S. H. Mousavi, A. Khanikaev, J. H. Connor, G. Shvets, and H. Altug, “Seeing protein monolayers with naked eye through plasmonic fano resonances,” *Proc. Natl. Acad. Sci. USA*, vol. 108, no. 29, pp. 11784–11789, 2011. [Online]. Available: <http://www.pnas.org/content/108/29/11784.abstract>
- [158] Y. LeCun, Y. Bengio, and G. Hinton, “Deep learning,” *Nature*, vol. 521, no. 7553, pp. 436–444, 05 2015. [Online]. Available: <http://dx.doi.org/10.1038/nature14539>
- [159] J. Misra and I. Saha, “Artificial neural networks in hardware: A survey of two decades of progress,” *Neurocomputing*, vol. 74, no. 1, pp. 239–255, 2010.
- [160] “On-chip Optical Neuromorphic Computing.”
- [161] N. C. Harris, D. Grassani, A. Simbula, M. Pant, M. Galli, T. Baehr-Jones, M. Hochberg, D. Englund, D. Bajoni, and C. Galland, “Integrated source of spectrally filtered correlated photons for large-scale quantum photonic systems,” *Physical Review X*, vol. 4, no. 4, p. 041047, 2014.
- [162] N. C. Harris, Y. Ma, J. Mower, T. Baehr-Jones, D. Englund, M. Hochberg, and C. Galland, “Efficient, compact and low loss thermo-optic phase shifter in silicon,” *Optics express*, vol. 22, no. 9, pp. 10487–10493, 2014.
- [163] N. C. Harris, G. R. Steinbrecher, J. Mower, Y. Lahini, M. Prabhu, T. Baehr-Jones, M. Hochberg, S. Lloyd, and D. Englund, “Bosonic transport simulations in a large-scale programmable nanophotonic processor,” *arXiv preprint arXiv:1507.03406*, 2015.
- [164] G. Golub and W. Kahan, “Calculating the singular values and pseudo-inverse of a matrix,” *Journal of the Society for Industrial & Applied Mathematics, Series B: Numerical Analysis*, vol. 2, no. 2, pp. 205–224, 1965.

- [165] M. Reck, A. Zeilinger, H. J. Bernstein, and P. Bertani, “Experimental realization of any discrete unitary operator,” *Phys. Rev. Lett.*, vol. 73, pp. 58–61, Jul 1994. [Online]. Available: <http://link.aps.org/doi/10.1103/PhysRevLett.73.58>
- [166] W. R. Clements, P. C. Humphreys, B. J. Metcalf, W. S. Kolthammer, and I. A. Walmsley, “An optimal design for universal multiport interferometers,” *arXiv preprint arXiv:1603.08788*, 2016.
- [167] [https://en.wikipedia.org/wiki/Optical\\_amplifier](https://en.wikipedia.org/wiki/Optical_amplifier).
- [168] A. Selden, “Pulse transmission through a saturable absorber,” *British Journal of Applied Physics*, vol. 18, no. 6, p. 743, 1967.
- [169] M. Soljačić, M. Ibanescu, S. G. Johnson, Y. Fink, and J. Joannopoulos, “Optimal bistable switching in nonlinear photonic crystals,” *Physical Review E*, vol. 66, no. 5, p. 055601, 2002.
- [170] B. Xu and N.-B. Ming, “Experimental observations of bistability and instability in a two-dimensional nonlinear optical superlattice,” *Phys. Rev. Lett.*, vol. 71, pp. 3959–3962, Dec 1993. [Online]. Available: <http://link.aps.org/doi/10.1103/PhysRevLett.71.3959>
- [171] E. Centeno and D. Felbacq, “Optical bistability in finite-size nonlinear bidimensional photonic crystals doped by a microcavity,” *Phys. Rev. B*, vol. 62, pp. R7683–R7686, Sep 2000. [Online]. Available: <http://link.aps.org/doi/10.1103/PhysRevB.62.R7683>
- [172] D. Chow and W. H. Abdulla, “Speaker identification based on log area ratio and gaussian mixture models in narrow-band speech,” in *PRICAI 2004: Trends in Artificial Intelligence*. Springer, 2004, pp. 901–908.
- [173] D. H. Deterding, “Speaker normalisation for automatic speech recognition.” Ph.D. dissertation, University of Cambridge, 1990.

- [174] Q. Bao, H. Zhang, Y. Wang, Z. Ni, Y. Yan, Z. X. Shen, K. P. Loh, and D. Y. Tang, "Atomic-layer graphene as a saturable absorber for ultrafast pulsed lasers," *Advanced Functional Materials*, vol. 19, no. 19, pp. 3077–3083, 2009. [Online]. Available: <http://dx.doi.org/10.1002/adfm.200901007>
- [175] A. P. Raman, M. A. Anoma, L. Zhu, E. Rephaeli, and S. Fan, "Passive radiative cooling below ambient air temperature under direct sunlight," *Nature*, vol. 515, no. 7528, pp. 540–544, 2014.
- [176] C. W. Hsu, B. Zhen, W. Qiu, O. Shapira, B. G. DeLacy, J. D. Joannopoulos, and M. Soljačić, "Transparent displays enabled by resonant nanoparticle scattering," *Nature communications*, vol. 5, 2014.
- [177] Y. Cho, Y. Choi, and S. Sohn, "Optical properties of neodymium-containing polymethylmethacrylate films for the organic light emitting diode color filter," *Applied physics letters*, vol. 89, no. 5, p. 051102, 2006.
- [178] P. B. Catrysse, W. Suh, S. Fan, and M. Peeters, "One-mode model for patterned metal layers inside integrated color pixels," *Optics letters*, vol. 29, no. 9, pp. 974–976, 2004.